BINARY NEUTRON STARS WITH ARBITRARY SPINS
IN NUMERICAL RELATIVITY

by

Nicholas A. Tacik

A thesis submitted in conformity with the requirements
for the degree of Doctor of Philosophy
Graduate Department of Astronomy & Astrophysics
University of Toronto

Abstract

Binary Neutron Stars with Arbitrary Spins

in Numerical Relativity

Nicholas A. Tacik

Doctor of Philosophy

Graduate Department of Astronomy & Astrophysics

University of Toronto

2016

We discuss spinning binary neutron stars in numerical relativity. Write a good abstract when done everything else.

Dedication

Dedicated to lots of good people. Write a proper dedication.

"Something inspirinsg."

Someone inspiring

Acknowledgements

Thanks to my friends and family.

Contents

List of Tables

List of Figures

Chapter 1

Introduction

1.1 Timeline

- Jun 15 - Send Harald completed draft of thesis and begin editing

- Jul 15 - Submit thesis

- Aug 30 - Defend thesis

- Each of the above could reasonably be pushed back 2 weeks depending on when Harald gets back to Toronto

1.2 Thesis TDL

- Fix all short captions of ch 5

- Modify introduction of introduction to discuss detection of gravitational waves

- Add introduction section to discuss detection of gravitational waves

- Need introduction section on current status of NR

- Organize what papers to put into that section

- Fix Ω driver section in the paper to use accurate equations

- Fix caption for 3+1 decomp text and add a sentence referencing it

- Read bunch of bh-ns papers to motivate the introduction of that section better. Log these papers in mendeley.

- Write up numerical methods section for bh-ns

- Add citaiton for dimensional reduction tehcniques

- fix table ref on page 33

- what does "appropriate averaging" mean on page 8?

- find a citation for PN results and methodology

- find a citation for the TT decomposition

- fix refernce to fig binary evolution

- collaction misspelled in ch2

1.3 Introduction

Einstein's theory of general relativity (GR) is now over a century old. One of its most striking predictions is the existence of gravitationl waves (GWs) - ripples in space-time that propagate at the speed of light. One of the ways these gravitational waves are generated is through the inspiral of compact object binaries. In these binaries, a neutron star (NS) or a black hole (BH), orbits with a NS/BH companion about their common centre of mass. Over time, through the emission of GW, the orbit shrinks and eventually the objects merge. Although these GW have never been directly detected, their existence has been indirectly confirmed. Hulse and Taylor won the 1993 Nobel Prize for

their observations of the Hulse-Taylor pulsar (Hulse & Taylor (1975a)) - a binary pulsar system whose orbital decay was carefully measured and found to match perfectly with the predctions of general relativity. Further observations have since strengthened these findings; see Berti et al. (2015) for a detailed review of current and future tests of GR.

Ground-based interferometric gravitational wave detectors are poised to make direction detections of GWs. With Advanced LIGO (Harry (2010); Aasi et al. (2015)) recently beginning its first science run, and Advanced Virgo (The Virgo Collaboration (2010); Acernese et al. (2015)) and KAGRA (Somiya & the KAGRA Collaboration (2012)) to soon follow, the first direct detection may come soon. Advanced LIGO expect a realistic event rate ~ 30 binary neutron star mergers per year at design sensitivity, with a horzion diestance of ~ 200 Mpc. Similarly, an event rate of ~ 10 mergers per year is expected for binary black holes, and ~ 10 for BH-NS binaries. These detectors are sensitive to frequencies of $\sim 10\text{Hz} - 1\text{kHz}$. Other detection methods, like pulsar timing arrays (see Joshi (2013)), are sensitive to very different frequency bands ($300\text{pHz} - 100\text{nHz}$).

These ground-based detectors use the technique of mathced filtering to make detections, in which the observed signal is mathced against teplate waveforms to search for the astrophysical signal. These templates are generated either using an analytically, using, for example, Post-Newtonian theory, an perturbative expansion of GR, or by using numerical relativity (NR), in which the Einstein Field Equations are solved numerically on sumpercomputers. PN wave are cheap to produce but become increasingly innaccurate near merger, while NR waveforms are more accurate, but are costly to produce. Hybridization techniques "stitch" PN waveofrms together with NR waveforms to get the best of both worlds.

The parameter space of numerical relativity simulations of black hole binaries is seven dimensional. Each black hole has a spin vector $\vec{\chi}$ with three components, and their mass ration $q == \equiv m_1/m_2$, where m_1 is the mass of the larger hole, is the 7th dimension. The total mass of the binary is scaled out of the numerical problem. Most compact object

systems are expected to circularize in their orbits before merger, so we do not regard orbital eccentriccity as part of the parameter space. Spanning this parameter space is a difficult endeavour for numerical relativity collaborations and much of it remains uncovered. Various dimensional reduction technqiues are used for Advanced LIGO template banks.

Once matter is added to simulations, through neutron stars, the parameter space increases signficantly. In addition to the 7 parameters already present in the black hole binaries, the total mass of the system is now a parameter, as the maximum NS provides a natural phsyical mass scale. This can affect, for example, whether or not a hyper-massive neutron star is present after the merger or if direct collapse to a black hole occurs. In addition, the NS equation of state (EOS) becomes important to the system. Many research groups use a polytropic equation of state $P = \kappa\rho^{\Gamma}$, as a simple choice. Recently, more focus has been placed on using piece-wise polytropes or tabulated EOS to represent EOS motivated by nuclear theory . There is hope that detections by by advanced LIGO will place constraints on the EOS of dense matter by measuring the orbital effect of tidal deformations of the NSs during the last stages of the orbit. Finally, the addition of matter adds additional physics to the problem. Numerical relativity simulations can investigate, for exmaple, neutrino heating in the post-merger disk, or the growth of magnetic fields that are thought to power short gamma ray bursts (GRBs). The field of multi-messenger seeks to use GW observations together with electromagnetic and neutrino observations to learn more about merging NS systems.

NS-NS binaries, unlike BH-BH and BH-NS bianries, have been observed and studied within our galaxy, and therefore the expections of Advanced LIGO for NS-NS binaries are more tightly constrained. The known binary neutron star population is summarized in table **??**. We report the spin periods, orbital periods, eccentriccites, characteristic life-times ($\tau_c = \dot{P}/2P$), time until merger, and the final spin periods of systems that will merge in a Hubble time. The system J0737-3039 is particuarly interesting, as one fot the

Table 1.1: The properties of known double neutron star systems

System	$P(ms)$	$P_{\rm orb}(d)$	e	$\log_{10}\tau_c(yr)$	$\log_{10}\tau_g(yr)$	$P_f(ms)$
J0737-3039	22.7	0.102	0.088	8.3	7.9	26.8
J0737-3039	2770	0.102	0.088	7.7	7.9	4453
J1518+4904	40.9	8.6	0.25	10.3	12.4	—
B1534+12	37.9	0.32	0.27	8.4	9.4	126
J1756-2251	28.5	0.32	0.18	8.6	10.2	—
J1811-1736	104.2	18.8	0.83	9.0	13.0	—
B1820-11	279.8	357.8	0.79	6.5	15.8	—
J1829+2456	41.0	1.18	0.14	10.1	10.8	—
J1906+0746	144.1	0.17	0.085	5.1	8.5	7224
B1913+16	59.0	0.3	0.62	8.0	8.5	120
B2127+11C	30.5	0.3	0.67	8.0	8.3	52.6

NSs will merge with a spin period of 22.4ms. This is comparable enough to the orbtial timescale near merger, $P \sim 2ms$, to be relevant to GW data analysis. NSs in binaries are spinning, and thus it is important to do NR simulations of spinning NS-NS binaries. For many years, spin was a largely unexamined dimension of the BNS paramter space, although there has been a significant interest lately. Add a note on why we want to study bns binaries. Add a note on corotational vs. irrotational vs. spinning.

This thesis is largely interested in spining neutron stars in numerical relativity. The structure is as follows: In chapter 2, we discuss our work on initial data and evolutions of spinning NS-NS binaries using the SpEC code. In chapter 3, we disucss the exntension of this initial data formalism to NS-BH binaries with a spinning NS. In chapter 4, we discuss the application of our initial data to studying spinning NS-NS binaries with interacting magnetic fields. In chapter 5, we shift focus and discuss work we have done on understanding the nature of "junk radiation" in Binary BH systems. Finally, in chapter

6 we conclude and summarize the thesis and discuss future possibilities.

The remainder of this introduction is structured as follows: In Section 1.4 we review the 2-body problem in GR and discuss some basic Post-Newtonian theory. In section 1.5, we review the initial value problem in NR. Finally, in section 1.6 we discuss some basic astrophysical properties of binary neutron star systems.

1.4   The two-body problem in General Relativity

In this section, we will review the basic scales and ideas that govern the two-body problem in general relativity. Specifically, when the bodies are of comparable masses (i.e., the mass ratio is not a perturbative parameter). Since the inspiral of two compact objects is driven by the emission of gravitational radiation, we being by reviewing gravitational waves.

We consider a perturbation to a Minkowski background, so we write the full metric as

$$g_{\mu\nu} = \eta_{\mu\nu} + h_{\mu\nu} \qquad |h| \ll 1. \tag{1.1}$$

It is easily verified that the inverse metric is

$$g^{\mu\nu} = \eta^{\mu\nu} - h^{\mu\nu}, \tag{1.2}$$

where

$$h^{\mu\nu} = \eta^{\mu\rho}\eta^{\sigma\nu}h_{\rho\sigma}, \tag{1.3}$$

as the assumption that $|h|$ is small allows us to neglect terms that are higher than first order in $h_{\mu\nu}$. It is now helpful to consider the "trace-reversed" perturbation defined as,

$$\bar{h}_{\mu\nu} = h_{\mu\nu} - \frac{1}{2}h\eta_{\mu\nu}. \tag{1.4}$$

It is easily verified that $\bar{h} = -h$, hence the name "trace-reversed". Next, we exploit our coordinate freedom and work in the Lorentz gauge, defined by

$$\nabla_{\mu}\bar{h}^{\mu\nu} = 0. \tag{1.5}$$

In this gauge, the Einstein tensor is simply

$$G_{\mu\nu} = -\frac{1}{2}\nabla_\rho\nabla^\rho\bar{h}_{\mu\nu}, \tag{1.6}$$

and so in vacuum, the Einstein field equations are a wave equation

$$\Box\bar{h}_{\mu\nu} = 0. \tag{1.7}$$

Thus we see that gravitational waves propagate at the speed of light. Using further coordinate freedom, it is convenient to work in the traceless-transverse (TT) gauge, defined by

$$\bar{h}^{\mathrm{TT}}_{\mu 0} = 0 \qquad \bar{h}^{\mathrm{TT}} = 0. \tag{1.8}$$

The first conditions guarantees that the non-zero components of $\bar{h}^{\mathrm{TT}}_{\mu\nu}$ are purely spatial, while the traceless condition guarantees that $\bar{h}^{\mathrm{TT}}_{\mu\nu} = \bar{h}^{\mathrm{TT}}_{\mu\nu}$. For the rest of this section, we will work only in the TT gauge.

The Lorentz gauge condition, transverse condition, and traceless condition account for 8 of the 10 degrees of freedom in the gravitational field $h_{\mu\nu}$. The remaining two degrees of freedom correspond go the two polarization states of gravitational waves. These are known as the "+" and "×" polarizations, due to their particular distorting effects acting upon a ring of particles (see Fig. 1.1). We can thus decompose a gravitational wave as

$$h^{\mathrm{TT}}_{ij} = h_+ e^+_{ij} + h_\times e^\times_{ij}. \tag{1.9}$$

When a matter source is present, the wave equation becomes

$$\nabla_\rho\nabla^\rho h_{\mu\nu} = -16\pi T_{\mu\nu}. \tag{1.10}$$

The solution to this equation can be written with the help of a Green's function,

$$h_{\mu\nu}(t, x^i) = 4\int d^3y \frac{1}{|x-y|} T_{\mu\nu}(t_r, y^i), \tag{1.11}$$

where t_r is the "retarded" time, $t_r = t - |x - y|$. This integral can be evaluated in terms of the quadruople tensor I^{ij} defined by

$$I^{ij}(t) = \int d^3x\, x^i x^j T^{00}(t, x^i), \tag{1.12}$$
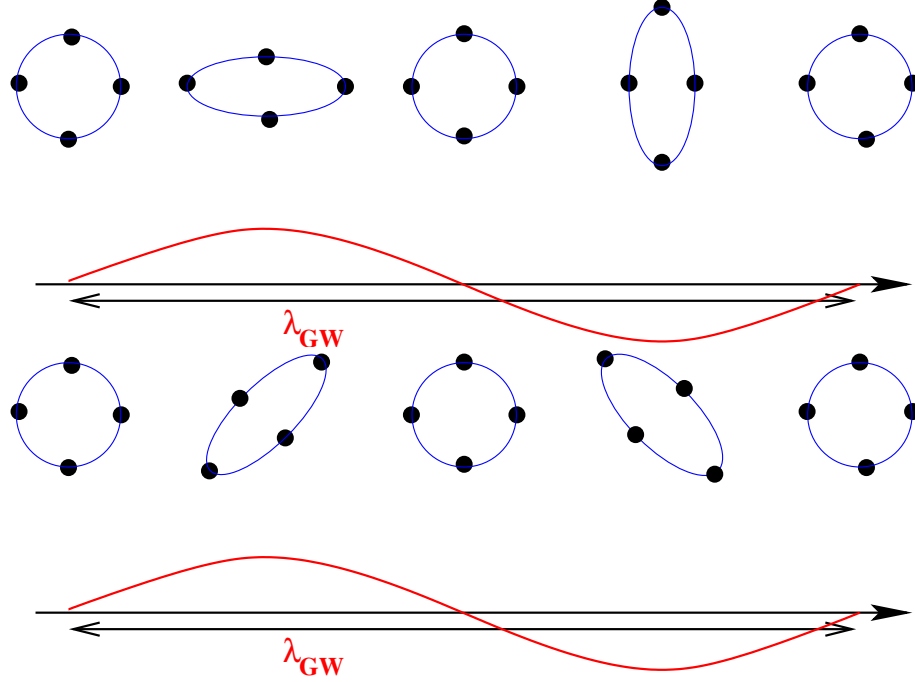
Figure 1.1: From Buonanno (2007). The top panel shows the effect of a + polarized gravitational wave passing through a ring of particles, in the direction perpendicular to the plane of the ring. The bottom panel shows the effect of a × polarized gravitational wave.

and the reduced quadrupole moment

$$J_{ij} = I_{ij} - \frac{1}{3}\eta_{ij}I, \tag{1.13}$$

where $I = I_\mu^\mu$. The result is

$$h_{ij}(t, x^i) = \frac{2}{r}\ddot{J}_{ij}^{\mathrm{TT}}(t_r) \tag{1.14}$$

In other words, linear gravitational waves are sourced by an oscillating quadrupole. To study the energy content of these gravitational waves, note that the effective stress-energy tensor of this spacetime is

$$T_{\mu\nu} = \frac{1}{32\pi}\left\langle \partial_\mu h_{ij}\partial_\nu h^{ij} \right\rangle. \tag{1.15}$$

where $<>$ denotes an appropriate averaging. This can be integrated to find the energy

output per unit time in gravitational waves,

$$L_{GW} = \frac{r^2}{16\pi} \oint \left\langle \dot{h}_\times^2 + \dot{h}_+^2 \right\rangle d\Omega \tag{1.16}$$

$$= \frac{1}{5} \left\langle \dddot{J}_{ij}^{\mathrm{TT}} \dddot{J}^{\mathrm{TTij}} \right\rangle. \tag{1.17}$$

Let us now consider a circular binary with total mass M, reduced mass μ, separation R and orbital frequency ω. Direct computation of the quadrupole tensor gives the simple result

$$L_{GW} = \frac{32}{5}\mu^2 M^3 R^{-5}. \tag{1.18}$$

Using this, along with the Newtonian estimates $\omega = M^{1/2}R^{-3/2}$, $E = -\frac{\mu M}{2R}$, $dE/dt = -L_{\mathrm{GW}}$, allows us the compute the characteristic inspiral scales. The binary shrinks at a rate

$$\frac{dR}{dt} = \frac{dE/dt}{dE/dr} = \frac{-64}{5}M^2\mu R^{-3}. \tag{1.19}$$

Integrating this expression gives the time to coallescence where $R = 0$ as

$$\tau_c = \frac{5}{256}M^{-2}\mu^{-1}R^4. \tag{1.20}$$

As the binary separation decreases, the orbital frequency increases. By integrating

$$\frac{df_{\mathrm{GW}}}{dt} = \frac{1}{\pi}\frac{d\omega}{dt} = \frac{-3M^{1/2}}{2}R^{-5/2}\frac{dR}{dt}, \tag{1.21}$$

the frequency evolution is given by

$$f_{\mathrm{GW}}(t) = \frac{\omega}{\pi} = \frac{1}{8\pi}\left(\frac{5}{\mu M^{2/3}(\tau_c - t)}\right)^{3/8}. \tag{1.22}$$

The number of gravitational waves cycles, $N = \int f_{\mathrm{GW}}dt$, in a given frequency band df_{GW} is given by

$$\frac{dN}{d\log f_{\mathrm{GW}}} = \frac{5}{96\pi}\frac{1}{(\pi\mathcal{M}f_{\mathrm{GW}})^{5/3}}, \tag{1.23}$$

where the quantity $\mathcal{M} = \mu^{3/5}M^{2/5}$ is called the "chirp mass". The explicit radiation pattern is given by

$$h_+ = \frac{4}{r}\mathcal{M}^{5/3}(2\omega)^{2/3}\cos(2\omega t + \phi)\left(\frac{1 + \cos^2\theta}{2}\right), \tag{1.24}$$

$$h_\times = \frac{4}{r}\mathcal{M}^{5/3}(2\omega)^{2/3}\sin(2\omega t + \phi)\cos\theta, \tag{1.25}$$

where r is the distance to the source, θ is the angle between the observer and the axis normal to the orbital plane of the binary, and ϕ is the arbitrary phase of the binary. Detectors are sensitive to the strain h, rather than the energy flux, and therefore a factor of x improvement in sensitivity results in a factor of x^3 higher event rate (assuming a uniformly placed distribution of sources).

These estimates were all made for a circular binary. If the binary has some eccentricity, e, then equation 1.16 is modified to

$$L_{GW} = \frac{32}{5}\mu^2 M^3 R^{-5} \left(1 + \frac{73}{24}e^2 + \frac{37}{96}e^4\right)\left(1 - e^2\right)^{-7/2} \tag{1.26}$$

However, eccentriccity is radiated away as the inspiral proceeds. The classic reference of Peters(1964) found that

$$\left\langle\frac{de}{dt}\right\rangle = -\frac{304}{15}e\frac{\mu M^2}{R^4\left(1-e^2\right)^{5/2}}\left(1 + \frac{121}{304}e^2\right). \tag{1.27}$$

Thus even a highly eccentric binary will radiate away its eccentricity and circularize before merger, provided the compact objects started far enough away from each other. Most numerical relativity simulations consider only circularized binaries and use techniques to attempt to get rid of any residual eccentricity.

The equations above in this section are valid only for a slowly-moving, weak-field system. As the system gets closer and closer to merger, these equations become increasingly inacurate. Post-Newtonian theory, by expanding to higher order, allows us to consider binaries with higher orbital frequencies. It is typically written as an expansion in the dimensionless parameter

$$x = \left(\frac{GM\omega}{c^3}\right)^{(2/3)}. \tag{1.28}$$

The evolution of the orbital phase, for example, can be written as

$$\phi = \frac{-x^{-5/2}}{32\nu}\left(1 + a_1 x + a_2 x^{3/2} + a_3 x^2 + a_4 x^{5/2} + a_5 x^3 + a_6 x^{7/2} + \mathcal{O}(1/c^8)\right) \tag{1.29}$$

where ν is the symmetric mass ratio, $\nu = \frac{m_1 m_2}{(m_1+m_2)^2}$, and each of the a_i are functions only of ν and $\log x$. This expression is said to be known to 3.5 Post-Newontian order.

Additional contrbutions come in at other PN orders, such as spin-orbit coupling at 1.5 PN order, spin-spin coupling at 2 PN order and tidal effects at 5 PN order. See cite for an overview of PN results and methodology.

1.5 The initial value problem in Numerical Relativity

From the point of view of numerical relativity, it is natural to use a 3+1 decomposition of space-time. In this section, we will review this process. Given a globally hyperbolic spacetime $(M, g_{\mu\nu})$. We foliate M by a set of $t = $ const hypersurfaces Σ_t.
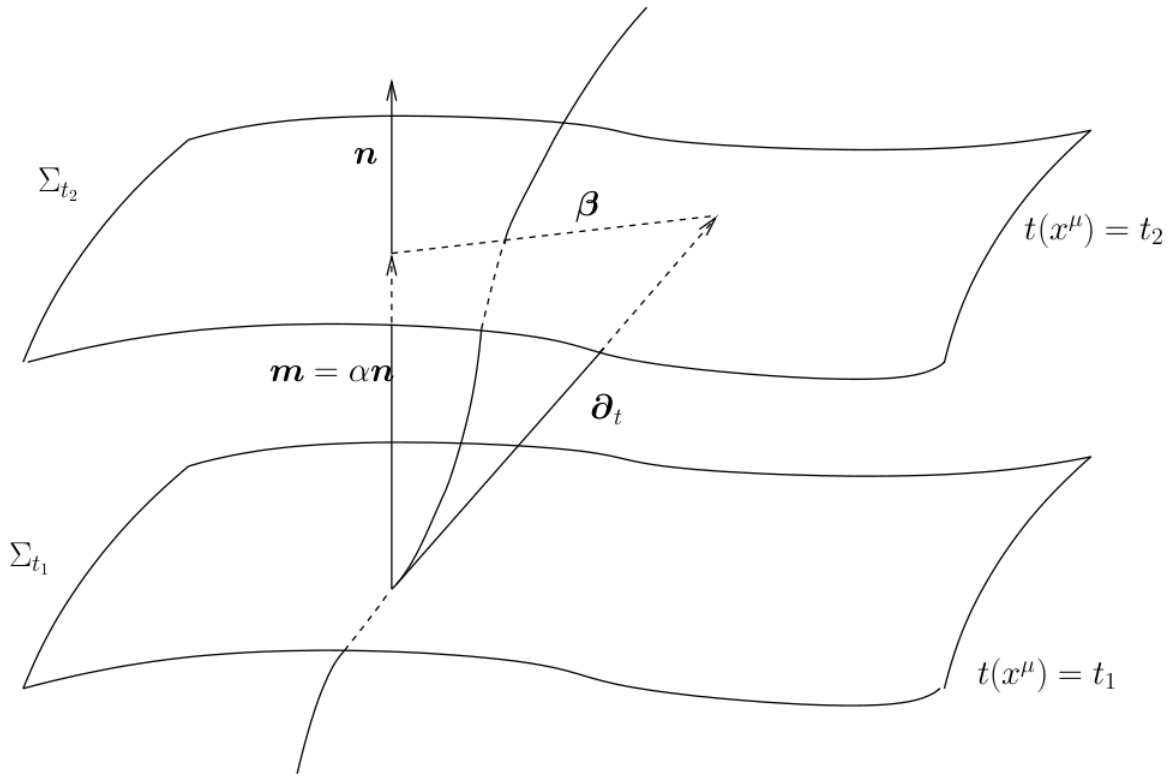
Figure 1.2: add caption - from here http://relativity.livingreviews.org/Articles/lrr-2015-1/articlese6.html

Each surface has a forward pointing unit normal

$$n^\mu = -g^{\mu\nu}\nabla_\nu t \left(g^{\mu\nu}\nabla_\mu t\nabla_\nu t\right)^{-1/2}, \tag{1.30}$$

induced metric

$$\gamma_{\mu\nu} = g_{\mu\nu} + n_\mu n_\nu, \tag{1.31}$$

and compatible derivative operator D. The induced metric measure curvature inside each hypersurface, while the extrinsic curvature $K_{\mu\nu}$ measures how the hypersurface is curved insde the space-time manifold M. It is defined by

$$K_{\mu\nu} = -\frac{1}{2}\mathcal{L}_n g_{\mu\nu}, \tag{1.32}$$

where $\mathcal{L}_n$ is the usual Lie derivative, along the direction of the vector field n^μ. The space-time metric is written as

$$ds^2 = -\alpha^2 dt^2 + \gamma_{ij}\left(dx^i + \beta^i dt\right)\left(dx^j + \beta^j dt\right). \tag{1.33}$$

Here α is known as the lapse function - it measures the proper time between neighbouring hypersurfaces. β^i is known as the shift - it measures the proper distance within a spatial hypersurface. The lapse and shift are both arbitrary - their choice amounts to a choice of coordinates.

Similar to how Maxwell's equations can be written as a set of constraint equations that do not contain any time derivatives,

$$D_i E^i - 4\pi\rho = 0, \tag{1.34}$$

$$D_i B^i = 0, \tag{1.35}$$

and evolution equations,

$$\partial_t E_i = \epsilon_{ijk} D^j B^k - 4\pi j_i \tag{1.36}$$

$$\partial_t B_i = -\epsilon_{ijk} D^j E^k, \tag{1.37}$$

(where E^i is the electric field, B^i is the magnetic field, ρ is the charge density, j^i is the current density, and ϵ_{ijk} is the Levi-Civitia symbol, and the equations are written in

Gaussian units), the same is true of Einstein's equations. The famous Hamiltonian and momentum constraints are

$$R + K^2 - K_{ij}K^{ij} = 16\pi\rho, \tag{1.38}$$

and,

$$D_j K_i^j - D_i K = 8\pi S_i \tag{1.39}$$

where ρ is the energy density measured by a normal observer, $\rho = n_i n_j T^{ij}$, and S_i is the momentum density measured by a normal observer $S_i = -\gamma_i^j n^k T_{jk}$. These are elliptic equations for the geometric quantities defined on the Σ_t. The general task of constructing initial data is to find $(\Sigma, g_{\mu\nu}, K_{\mu\nu})$ that satisfy the constraint equations and represent well the physical situation at hand (e.g., the inspiral of a compact object binary). The evolution equations are

$$\partial_t \gamma_{ij} = -2\alpha K_{ij} + D_i\beta_j + D_j\beta_i \tag{1.40}$$

and

$$\partial_t K_{ij} = -D_i D_j\alpha + \alpha\left(R_{ij} - 2K_{ik}K_j^k + KK_{ij}\right) - 8\pi\alpha(S_{ij} - \frac{1}{2}\gamma_{ij}(S-\rho)) + \beta^k D_k K_{ij} + K_{ik}D_j\beta^k + K_{kj}D_i\beta^k \tag{1.41}$$

, where S_{ab} is the spatial stress, $S_{ab} = \gamma_a^c \gamma_b^d T_{cd}$, and S is its trace. Once constraint satisfying initial data has been constructed, the evolution equations determine the geometric quantities at all future times. Analytically, the evolution equations preserve the constraints, although numerically this may not always be the case.

There are many sets of data $(g_{\mu\nu}, K_{\mu\nu})$ that will satisfy the constraint equations. The task remains, then, to choose this free data appropriately. To do so, one typically begins with a conformal decomposition of the metric,

$$\gamma_{ij} = \Psi^4 \tilde{\gamma}_{ij}. \tag{1.42}$$

Here, Ψ is called the conformal factor, and $\tilde{\gamma}_{ij}$ is called the conformal metric. Next we break up the extrinsic curvature into its trace and trace-free parts,

$$K_{ij} = A_{ij} + \frac{1}{3}\gamma_{ij}K. \tag{1.43}$$

The Hamiltonian and Momentum constraints become

$$\tilde{D}^2\Psi - \frac{1}{8}\Psi\tilde{R} - \frac{1}{12}\Psi^5 K^2 + \frac{1}{8}\Psi^{-5}\tilde{A}_{ij}\tilde{A}^{ij} = -2\pi\Psi^{-5}\rho. \tag{1.44}$$

$$D_j A^{ij} - \frac{2}{3}D^i K = 8\pi j^i, \tag{1.45}$$

$\tilde{A}^{ij} = \Psi^{-10}A^{ij}$. We now proceed according to the extended conformal thin sandwich formalism. See cite for a review of the alternative traceless-transverse decomposition. We define

$$\tilde{u}_{ij} = \partial_t\tilde{\gamma}_{ij}, \tag{1.46}$$

and we introduce the scalings

$$\tilde{j}^i = \Psi^{10}j^i, \tag{1.47}$$

$$\tilde{\rho} = \Psi^8\rho \tag{1.48}$$

$$\tilde{A}^{ij} = \Psi^{10}A^{ij}. \tag{1.49}$$

The Hamiltonian and Momentum constraints constraints can now be viewed as equations for the shift and conformal factor

$$\tilde{D}^2\Psi - \frac{1}{8}\Psi\tilde{R} - \frac{1}{12}\Psi^5 K^2 + \frac{1}{8}\Psi^{-7}\tilde{A}_{ij}\tilde{A}^{ij} = -2\pi\Psi^{-3}\tilde{\rho}, \tag{1.50}$$

$$\tilde{D}_j\left(\frac{1}{2\tilde{\alpha}}\left(\mathbb{L}\beta\right)^{ij} - \tilde{D}_j\left(\frac{1}{2\tilde{\alpha}}\tilde{u}^{ij}\right)\right) - \frac{2}{3}\Psi^6\tilde{D}^i K = 8\pi\tilde{j}^i, \tag{1.51}$$

where

$$\tilde{\alpha} = \Psi^6\alpha \tag{1.52}$$

is the conformal lapse and

$$\left(\tilde{\mathbb{L}}\beta\right)^{ij} = \Psi^4\left(D^i\beta^j + D^j\beta^i - \frac{2}{3}\gamma^{ij}D_k\beta^k\right) \tag{1.53}$$

is the conformal longitudinal operator. The lapse is given by the evolution equation of K,

$$\tilde{D}^2\left(\tilde{\alpha}\Psi^7\right) - \left(\tilde{\alpha}\Psi^7\right)\left[\frac{1}{8}\tilde{R} + \frac{5}{12}\Psi^4 K^2 + \frac{7}{8}\Psi^{-8}\tilde{A}_{ij}\tilde{A}^{ij}\right.$$

$$\left. + 2\pi\Psi^{-2}\left(\tilde{E} + 2\tilde{S}\right)\right] = -\Psi^5\left(\partial_t K - \beta^k D_k K\right). \tag{1.54}$$

The free data are $\tilde{\gamma}_{ij}, \tilde{u}_{ij}, K, \partial_t K$. In a coordinate system corotating with the binary, it is natural to choose $\tilde{u}_{ij} = 0, \partial_t K = 0$. Common choices are conformal flatness, $\tilde{\gamma}_{ij} = \delta_{ij}$ and maximal slicing $K = 0$. With appropriate boundary conditions, the system of equations can now be solved.

1.6 Binary Neutron Star Systems

To begin our discussion of the properties of binary neutron star binaries, we should first briefly review how these system forms. We follow the discussion outlined in Postnov & Yungelson (2014). The standard formation scenario is illustrated in figure **??**, and goes as follows:

- We begin with two high mass OB main-sequence stars undergoing standard binary evolution. Eventually the more massive (primary) star burns its central hydrogen, and a helium core is left over.

- The primary star then rapidly expands, overflows its Roche lobe, and begins a period of mass transfer onto the secondary star. This period lasts until most of the primary's Hydrogen envelope has been transferred, leaving behind a naked helium core.

- The primary star eventually collapses as a core-collapse supernova, leaving behind a neutron star. It is likely that the explosion disrupts the binary, but let us assume that it survives. We then have a massive main sequence star in orbit with a neutron star.

- Eventually the secondary star evolves off the main sequence, expands, and overflows its Roche lobe. It will then begin accreting mass onto the primary. This accretion spins up the neutron star, thus "recycling" it. It also leads to strong x-ray emission.

- The secondary further expands and a common envelope stage ensues. Eventually the secondary explodes as a supernova, and becomes a neutron star.

- If the system is not disrupted, it can then become a binary that will eventually merge due to the continuous emission of gravitational waves.

As discussed earlier, such systems are expected to be quasi-circular once they enter the LIGO band. There are, however, other ways of forming systems that are highly eccentric while in the LIGO band. For example, the dynamical capture in a close two-body encounter in a dense cluster environment, or a binary in a hierarchichal triple system whose eccentricity is enhanced by the Kozai mechanism. Nonetheless, quasi-circular binaries are expected to constitute the large majority of gravitational wave sources.

The end state of a binary neutron star merger depends strongly on the properties of the stars. For systems with a combined mass less than the maximum mass allowed by the EOS, the final result would be a more massive neutron star. Otherwise, the final result will be a single Kerr black hole. Simulations have shown that these black holes will have a spin on the order of $\chi \simeq 0.6 - 0.8$. The intermediate state is known as a hypermassive neutron star (HMNS). This is a NS whose mass is above the maximum mass allowed by the EOS, temporarily supported by differential rotation and thermal pressure. Over time, angular momentum is efficiently transported out of the system, and it collapses into a black hole. We can further subdivide these systems based on the timescale for callapse - prompt collapse or delayed collapse. In the prompt case, the pressure support is too low, and the system collapses on a $\sim$ freefall timescale. This is expected in systems with a large total mass ($\gtrsim 2.8 M_\odot$), although the details depend, of course, on the EOS. In the delayed collapse case, the collapse timescale depends on
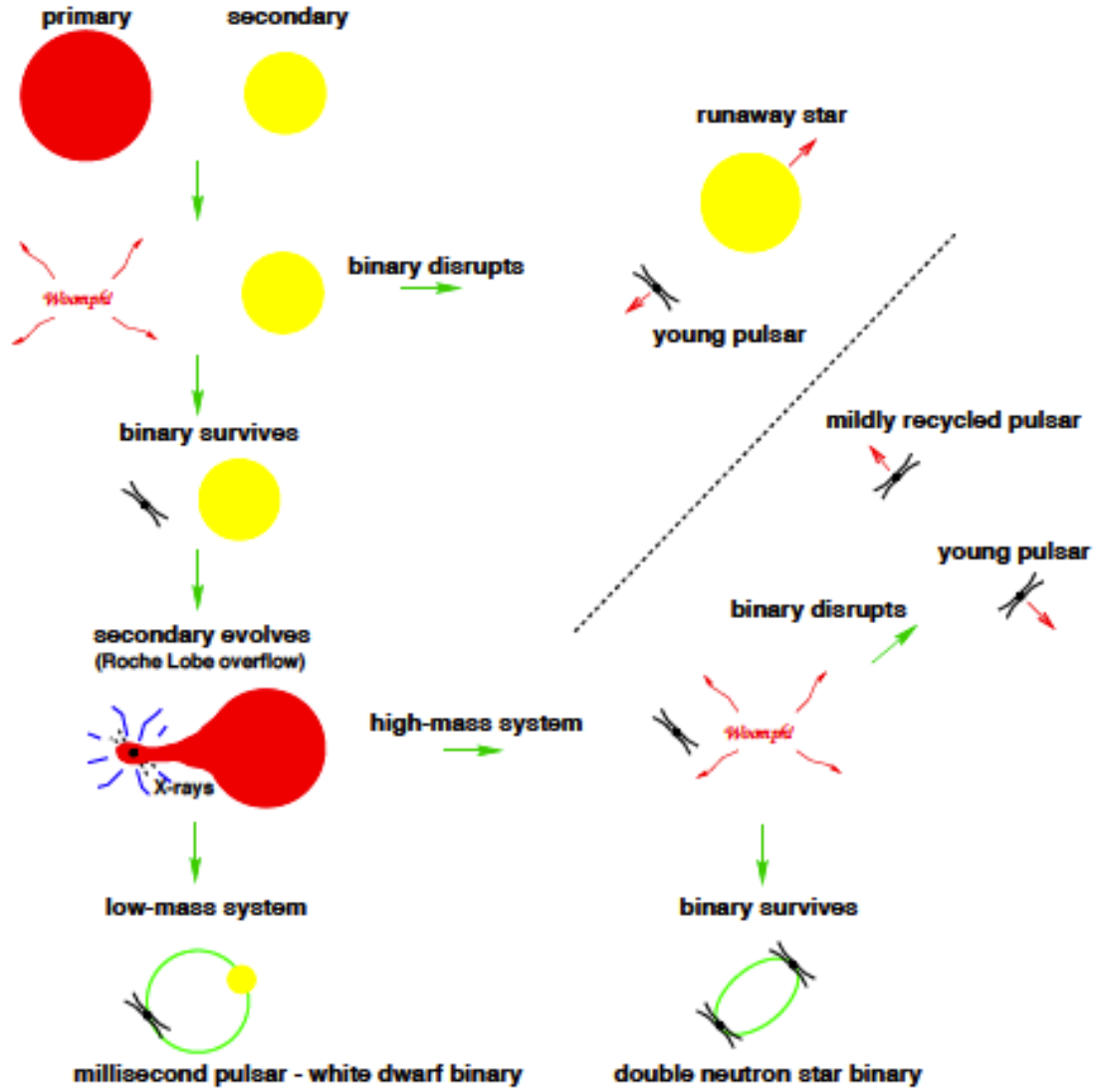
Figure 1.3: From Lorimer (2008). The possible evolutionary scenarios of a typical high mass binary are shown.

many factors. Angular momentum distribution by magnetic winding is an important factor - it operates on the Alfven timescale $\tau \sim R\sqrt{\rho}/B \simeq 10 - 100$ms. Transport driven by magneto-rotational instability is also important. It is of the order $\tau \sim 100$ms for $B \simeq 10^{15}G$. Cooling by neutrino or electromagnetic emission is also important, as

it decreases thermal pressure, although it operates on a longer timescale, $\sim$ seconds. An accretion disk around the eventual BH, lying beyond the ISCO, will form, with a mass of $\simeq 0.01 - 0.3M_\odot$. The amount of material in the disk depends on the time to BH formation, as there is more time to distribute angular momentum ot the disk. HMNS systems emit gravitational waves at peak frequencies of approximately $2 - 4$kHz, unfortunately outside of the optimal frequency range of ground-based detectors. The mass ratio of the system is another important factor. Figure 1.4 shows the post-merger remnant of an equal-mass system, and of a system with mass ratio $q \sim 1.38$. The equal mass system shows a "dumbell"-like structure, composed of two cores which, over time, turn into an ellipsoidal HMNS. The non-equal-mass case shows two asymmetric cores, which act like the smaller one orbiting the larger one. The stronger tidal forces in this case cause the outher layers of the smaller star to be stripped off and form an envelope around the HMNS. Higher disk mass correlates with higher deviations from $q = 1$, as well as with higher NS compactness.

The merger of two neutron stars is the site of the emission of a tremendous amount of electromagnetic energy. Their mergers are thought to be one of the most promising candidates to be the progenitors of short gamma ray bursts (SGRBs), although there is not yet definitive evidence of it. The engine of a rotating black hole, surrounded by a hot accretion torus and a collimiated magnetic field contains the necessary ingreidients thought to be needed for a SGRB. Apart from this, another promising candidate for electromagnetic signature is the "kilonova" - emission powered by the radioactive decay of r-process elements formed in the merger, lasting on the time-scale of $\sim$ weeks. Multi-messenger astronomy (see Fan & Hendry (2015) for a review) seeks to combine information from gravitational waves, these electromagnetic events, and possible neutrino observations, to further elucidate the astrophysics of these mergers.

One of the most exciting prospects of the Advanced LIGO era is using gravitational wave observations to constrain the NS EOS. The EOS of dense nuclear matter is an open

question of tremendous interest to nuclear physicists and astrophysicists alike. Tidal effects are parameterized by the tidal deformability paramter λ, which relates the induced quadrupole field of one star, Q_{ij}, to the tidal field in which it is immersed, $\mathcal{E}_{ij}$:

$$Q_{ij} = -\lambda(m; \text{EOS})\mathcal{E}_{ij}. \tag{1.55}$$

Or, likewise, by the second tidal Love number,

$$k_2 = \frac{3}{2}\frac{\lambda}{R^5}. \tag{1.56}$$

These enter the PN equations for binary phase at the very high 5PN order, but because of the large pre-factors, they are still very important in the late-stage inspiral dynamics. Much work has been done to estimate how well Advanced LIGO can measure these paramters (see Read et al. (2009); Hinderer et al. (2010); Damour et al. (2012); Lackey et al. (2012)). Del Pozzo et al. (2013) (further extended in Agathos et al. (2015)) used a Bayesian framework to show that λ could be constrained at the 10% level after a few tens of detections. There is also the question of more exotic NS matter. Chatziioannou et al. (2015) studied various possibilities and found, for example, that a detection with an SNR of ~ 20 could provide good evidence of the existence or non-existence of strange quark stars. However, kaon condensates or hyperons in NS cores are much more difficulty to confirm.

Numerical simulations of the mergers of binary neutron stars have been possible for at least fifteen years cite. Since then, simulations have rapidly progressed, adding more resolution, more orbits, more detailed physics, and a better coverage of the available paramter space. Cite a bunch of papers here, on those different things. With the great increase in simulation technology, and the coincident start of the Advanced LIGO era, it is truly an exciting time for this field.
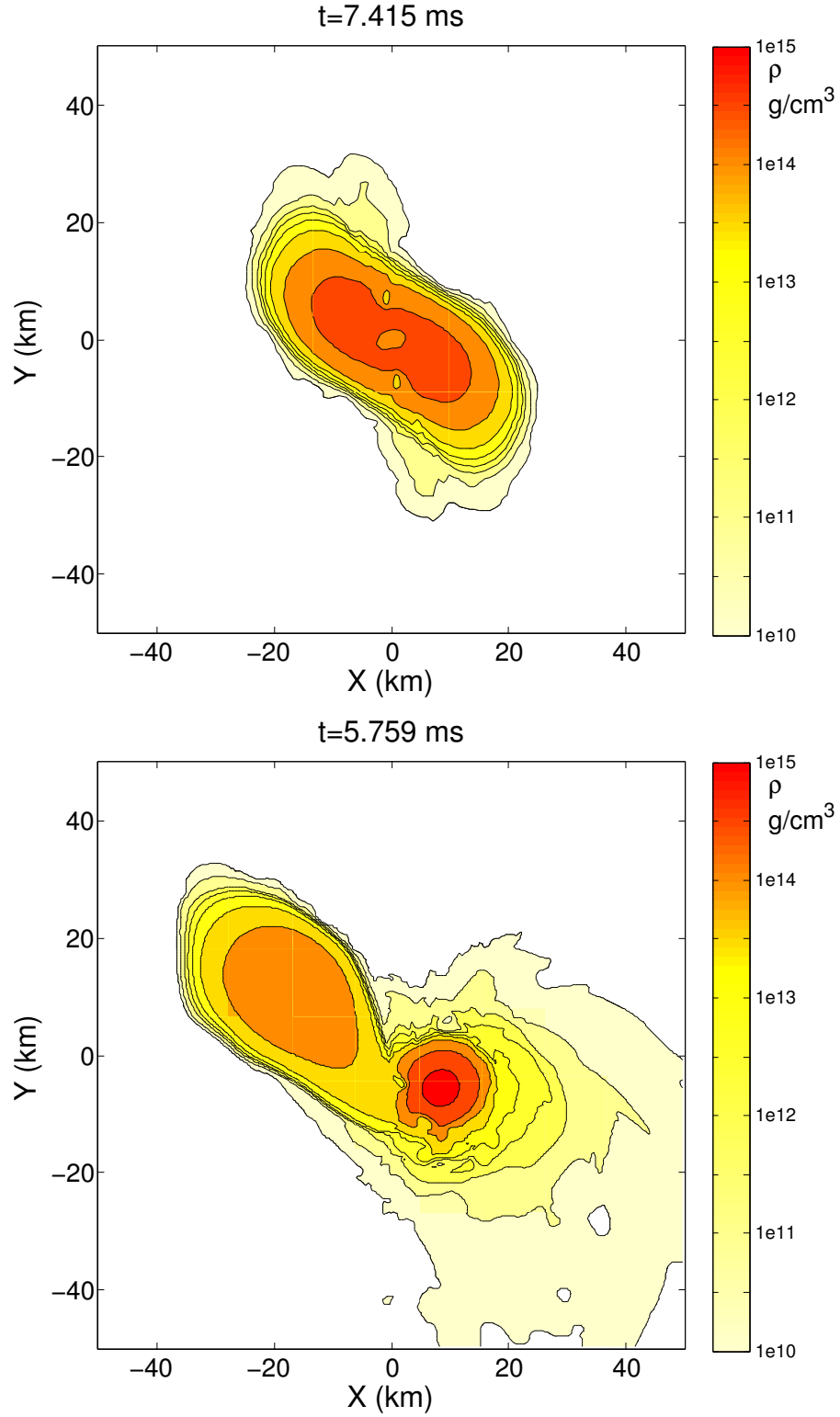
Figure 1.4: From Rezzolla et al. (2010). The top panel shows the iso-density contours of the HMNS from an equal mass system with baryon masses $M_1 = M_2 = 1.643 M_\odot$. The bottom panel shows the iso-density contours of the HMNS from a system with baryon masses $M_1 = 1.304 M_\odot$ and $M_2 = 1.805 M_\odot$.

Chapter 2

Binary Neutron Stars with Arbitrary Spins in Numerical Relativity

- Modify text based on changes from submitted paper

- Modify figures so that they fit on one page

- Modify figure captions so that they are small

2.1   Chapter Overview

We present a code to construct initial data for binary neutron star systems in which the stars are rotating. Our code, based on a formalism developed by Tichy, allows for arbitrary rotation axes of the neutron stars and is able to achieve rotation rates near rotational breakup. We compute the neutron star angular momentum through quasi-local angular momentum integrals. When constructing irrotational binary neutron stars, we find a very small residual dimensionless spin of $\sim 2 \times 10^{-4}$. Evolutions of rotating neutron star binaries show that the magnitude of the stars' angular momentum

is conserved, and that the spin- and orbit-precession of the stars is well described by post-Newtonian approximation. We demonstrate that orbital eccentricity of the binary neutron stars can be controlled to $\sim 0.1\%$. The neutron stars show quasi-normal mode oscillations at an amplitude which increases with the rotation rate of the stars.

2.2 Introduction

Several known binary neutron star (BNS) systems will merge within a Hubble time due to inspiral driven by gravitational radiation Lorimer (2008), most notably the Hulse-Taylor pulsar Hulse & Taylor (1975b). Therefore, binary neutron stars constitute one of the prime targets for upcoming gravitational wave detectors like Advanced LIGO Harry (2010); Aasi et al. (2015) and Advanced Virgo The Virgo Collaboration (2010); Acernese et al. (2015). The neutron stars in known binary pulsars have fairly long rotation periods Lorimer (2008). The system J0737-3039 Lyne et al. (2004) contains the fastest known spinning neutron star in a binary with a rotation period of 22.7ms. This system will merge within $\sim 10^8$ years through gravitational wave driven inspiral. Globular clusters contain a significant fraction of all known milli-second pulsars Lorimer (2008), which through dynamic interactions, may form binaries Lee et al. (2010); Benacquista & Downing (2013). Gravitational wave driven inspiral reduces Peters & Mathews (1963); Peters (1964) the initially high eccentricity of dynamical capture binaries. Given the presence of milli-second pulsars in globular clusters, dynamically formed BNS may contain very rapidly spinning neutron stars with essentially arbitrary spin orientations. Presence of spin in BNS systems does influence the evolution of the binary. For instance, in order to avoid a loss in sensitivity in GW searches, one needs to account for the NS spin Brown et al. (2012). Furthermore, early BNS simulations Shibata & Uryu (2000) of irrotational and corotational BNS systems found that the spin of corotating BNS noticeably increased the size of accretion discs occurring during the merger of the two NS. The properties of accretion discs and unbound ejecta are intimately linked to electromagnetic

and neutrino emission from merging compact object binaries Metzger & Berger (2012). Understanding the behavior of rotating BNS systems is therefore important to quantify the expected observational signatures from such systems. These considerations motivated a recent interest in the numerical modeling of rotating binary neutron star systems during their last orbits and coalescence. Baumgarte and Shapiro Baumgarte & Shapiro (2009), Tichy Tichy (2011), and East et al East et al. (2012) presented formalisms for constructing BNS initial data for spinning neutron stars. Tichy proceeded to construct rotating BNS initial data Tichy (2012); and Ref. Bernuzzi et al. (2014) studies short inspirals and mergers of BNS with rotation rates consistent with known binary neutron stars (i.e. a dimensionless angular momentum of each star $\chi = S/M^2 \lesssim 0.05$), and rotation axes aligned with the orbital angular momentum. Very recently, Dietrich et al. Dietrich et al. (2015) presented a comprehensive study of BNS, including a simulation of a precessing, merging BNS. East et. al. East et al. (2015) investigate interactions of rotating neutron stars on highly eccentric orbit. Kastaun et al. Kastaun et al. (2013) determine the maximum spin of the black hole remnant formed by the merger of two aligned spin rotating neutron stars. Tsatsin and Marronetti Tsatsin & Marronetti (2013) present initial data and evolutions for non-spinning, spin-aligned and anti-aligned data sets. Tsokaros et. al. Tsokaros et al. (2015) presented initial data and quasi-equilibrium sequences of spin-aligned and anti-aligned binaries with a nuclear equation of state.

Previous studies differ in the type of initial data used: Refs. Baumgarte & Shapiro (2009); Tichy (2011; 2012); Bernuzzi et al. (2014) construct and utilize constraint-satisfying initial data, which also incorporates quasi-equilibrium of the binary system. Refs. East et al. (2012; 2015) construct constraint-satisfying data based on individual TOV stars, without regard of preserving quasi-equilibrium in the resulting binary, but providing greatly enhanced flexibility in the type of configurations that can be studied, e.g. hyperbolic encounters. Refs. Kastaun et al. (2013); Tsatsin & Marronetti (2013), finally, only approximately satisfy the constraint equations. Previous studies also differ in the

rigor with which the neutron star angular momentum is measured. Ref. Tichy (2012) merely discusses the neutron stars based on a rotational velocity ω^i entering the initial data formalism (cf. our Eq. (2.48) below), whereas Refs. Bernuzzi et al. (2014); Kastaun et al. (2013); East et al. (2015) estimate the initial neutron star spin either based on single star models or based on the differences in binary neutron star initial data sets with and without rotation, and thus neglecting the impact of interactions in the binary. All these studies measure the neutron star angular momentum in the initial data. Changes in the neutron star angular momentum that could happen during initial relaxation of the binary or during the subsequent evolution of the binary are not monitored.

In this paper we study the construction of rotating binary neutron star initial data and the evolution through the inspiral phase. We implement the constant rotational velocity (CRV) formalism developed by Tichy Tichy (2012), and construct constraint satisfying BNS initial data sets with a wide variety of spin rates, as well as different spin directions. We apply quasi-local angular momentum techniques developed for black holes to our BNS initial data sets; the quasi-local spin indicates that we are able to construct BNS with dimensionless angular momentum exceeding 0.4. Evolving some of the constructed initial data sets through the inspiral phase, we demonstrate that we can control and reduce orbital eccentricity by an iterative adjustment of initial data parameters controlling orbital frequency and radial velocity of the stars, both for non-precessing (i.e. aligned-spin binaries) and precessing binaries. When monitoring the quasi-angular momentum of the neutron stars during the inspiral, we find that its magnitude is conserved, and the spin-direction precesses in a manner consistent with post-Newtonian predictions.

This paper is organized as follows. Section 5.5 describes the initial data formalism and our numerical code to solve for rotating BNS initial data. In Sec. 2.4 we use this code to study a range of initial configurations, with a special emphasis on the behavior of the quasi-local spin diagnostic. We evolve rotating BNS in Sec. 2.5, including a discussion of eccentricity removal, the behavior of the quasi-local spin diagnostics, and a comparison

of the precession dynamics to post-Newtonian theory. A discussion concludes the paper in Sec. 2.6. In this paper, we work in units where $G = c = M_\odot = 1$.

2.3 Methodology

2.3.1 Formalism for irrotational binaries

To start, we will review a formalism commonly used for the construction of initial data for system of irrotational binary neutron stars. We will then discuss how to build upon this formalism to construct initial data for neutron stars with arbitrary spins.

We begin with the 3+1 decomposition of the space-time metric (see Gourgoulhon (2007) for a review),

$$ds^2 = -\alpha^2 dt^2 + \gamma_{ij} \left(dx^i + \beta^i dt\right) \left(dx^j + \beta^j dt\right). \tag{2.1}$$

Here, α is the lapse function, β^i is the shift vector and γ_{ij} is the 3-metric induced on a hypersurface $\Sigma(t)$ of constant coordinate time t. In this decomposition, the unit normal vector n^μ to $\Sigma(t)$ and the tangent vector t^μ to the coordinate line t are related by

$$t^\mu = \alpha n^\mu + \beta^\mu, \tag{2.2}$$

with $n_\mu = (-\alpha, 0, 0, 0)$ and $\beta^\mu = (0, \beta^i)$. The extrinsic curvature of $\Sigma(t)$ is the symmetric tensor defined as

$$K_{\mu\nu} = -\nabla_\nu n_\mu - n_\nu \gamma^\lambda_{\ \mu} \nabla_\lambda(\ln \alpha) = -\frac{1}{2} \mathcal{L}_n \gamma_{\mu\nu}, \tag{2.3}$$

where $\gamma_{\mu\nu} = g_{\mu\nu} + n_\mu n_\nu$ is the extension of the 3-metric γ_{ij} to the 4-dimensional spacetime, and $g_{\mu\nu}$ is the 4-metric of that spacetime. By construction, $K^{\mu\nu} n_\mu = 0$ and we can restrict $K^{\mu\nu}$ to the 3-dimensional tensor K^{ij} defined on $\Sigma \times \Sigma$. The extrinsic curvature K^{ij} is then divided into its trace K and trace-free part A^{ij}:

$$K^{ij} = A^{ij} + \frac{1}{3} \gamma^{ij} K. \tag{2.4}$$

We treat the matter as a perfect fluid with stress-energy tensor

$$T_{\mu\nu} = (\rho + P)\, u_\mu u_\nu + P g_{\mu\nu}, \tag{2.5}$$

where $\rho = \rho_0(1 + \epsilon)$ is the energy density, ρ_0 the baryon density, ϵ the specific internal energy, P the pressure, and u_μ the fluid's 4-velocity. For the initial value problem, it is often convenient to consider the following projections of the stress tensor:

$$
\begin{aligned}
E &= T^{\mu\nu} n_\mu n_\nu, & (2.6) \\
S &= \gamma^{ij} \gamma_{i\mu} \gamma_{j\nu} T^{\mu\nu}, & (2.7) \\
J^i &= -\gamma^i{}_\mu T^{\mu\nu} n_\nu. & (2.8)
\end{aligned}
$$

We then further decompose the metric according to the conformal transformation

$$\gamma_{ij} = \Psi^4 \tilde{\gamma}_{ij}. \tag{2.9}$$

Other quantities have the following conformal transformations:

$$
\begin{aligned}
E &= \Psi^{-6} \tilde{E}, & (2.10) \\
S &= \Psi^{-6} \tilde{S}, & (2.11) \\
J^i &= \Psi^{-6} \tilde{J}^i, & (2.12) \\
A^{ij} &= \Psi^{-10} \tilde{A}^{ij}, & (2.13) \\
\alpha &= \Psi^6 \tilde{\alpha}. & (2.14)
\end{aligned}
$$

$\tilde{A}^{ij}$ is related to the shift and the time derivative of the conformal metric, $\tilde{u}_{ij} = \partial_t \tilde{\gamma}_{ij}$ by

$$\tilde{A}^{ij} = \frac{1}{2\tilde{\alpha}} \left[\left(\tilde{\mathbb{L}}\beta\right)^{ij} - \tilde{u}^{ij} \right], \tag{2.15}$$

where $\tilde{\mathbb{L}}$ is the conformal longitudinal operator whose action on a vector V^i is

$$\left(\tilde{\mathbb{L}}V\right)^{ij} = \tilde{\nabla}^i V^j + \tilde{\nabla}^j V^i - \frac{2}{3} \tilde{\gamma}^{ij} \tilde{\nabla}_k V^k, \tag{2.16}$$

and $\tilde{\nabla}$ is the covariant derivative defined with respect to the conformal 3-metric $\tilde{\gamma}_{ij}$.

In the 3+1 formalism, the Einstein equations are decomposed into a set of evolution equations for the metric variables as a function of t, and a set of constraint equations on each hypersurface $\Sigma(t)$. The initial data problem consists in providing quantities $g_{\mu\nu}(t_0)$ and $K_{\mu\nu}(t_0)$ which satisfy the constraints on $\Sigma(t_0)$ and represent initial conditions with the desired physical properties (e.g. masses and spins of the objects, initial orbital frequency, eccentricity, etc.).We solve the constraint equations using the Extended Conformal Thin Sandwich (XCTS) formalism York (1999), in which the constraints take the form of five nonlinear coupled elliptic equations. The XCTS equations can be written as

$$
2\tilde{\alpha}\left[\tilde{\nabla}_j\left(\frac{1}{2\tilde{\alpha}}(\tilde{L}\beta)^{ij}\right) - \tilde{\nabla}_j\left(\frac{1}{2\tilde{\alpha}}\tilde{u}^{ij}\right)\right.
$$
$$
\left. -\frac{2}{3}\Psi^6\tilde{\nabla}^i K - 8\pi\Psi^4\tilde{J}^i\right] = 0, \tag{2.17}
$$

$$
\tilde{\nabla}^2\Psi - \frac{1}{8}\Psi\tilde{R} - \frac{1}{12}\Psi^5 K^2
$$
$$
+\frac{1}{8}\Psi^{-7}\tilde{A}_{ij}\tilde{A}^{ij} + 2\pi\Psi^{-1}\tilde{E} = 0, \tag{2.18}
$$

$$
\tilde{\nabla}^2\left(\tilde{\alpha}\Psi^7\right) - \left(\tilde{\alpha}\Psi^7\right)\left[\frac{1}{8}\tilde{R} + \frac{5}{12}\Psi^4 K^2 + \frac{7}{8}\Psi^{-8}\tilde{A}_{ij}\tilde{A}^{ij}\right.
$$
$$
\left. +2\pi\Psi^{-2}\left(\tilde{E} + 2\tilde{S}\right)\right] = -\Psi^5\left(\partial_t K - \beta^k\partial_k K\right). \tag{2.19}
$$

We solve these equations for the conformal factor Ψ, the densitized lapse $\tilde{\alpha}\Psi^7$ and the shift β^i. $\tilde{E}$, $\tilde{S}$ and $\tilde{J}^i$ determine the matter content of the slice. The variables $\tilde{\gamma}_{ij}$, $\tilde{u}_{ij} = \partial_t\tilde{\gamma}_{ij}$, K and $\partial_t K$ are freely chosen.

If we work in a coordinate system corotating with the binary, $\tilde{u}_{ij} = 0$ and $\partial_t K = 0$ are natural choices for a quasi-equilibrium configuration. Following earlier work Taniguchi et al. (2007; 2006); Foucart et al. (2008), we also choose to use maximal slicing, $K = 0$,

and a conformally flat metric, $\tilde{\gamma}_{ij} = \delta_{ij}$. Maximal slicing is a gauge choice that determines the location of the initial data hypersurface in the embedding space time. Conformal flatness is used for computational convenience; rotating black holes are known to be not conformally flat Garat & Price (2000), and so this simplifying assumption should be revisited in the future.

In addition to solving these equations for the metric variables, we must impose some restrictions on the matter. In particular, the stars should be in a state of approximate hydrostatic equilibrium in the comoving frame. This involves solving the Euler equation and the continuity equation. For an irrotational binary, the first integral of the Euler equation leads to the condition

$$h\alpha\frac{\gamma}{\gamma_0} = C, \tag{2.20}$$

where C is a constant, hereafter referred to as the Euler constant, the enthalpy h is defined as

$$h = 1 + \epsilon + \frac{P}{\rho_0}, \tag{2.21}$$

and we have introduced

$$\gamma = \gamma_n\gamma_0\left(1 - \gamma_{ij}U^iU_0^j\right), \tag{2.22}$$

$$\gamma_0 = \left(1 - \gamma_{ij}U_0^iU_0^j\right)^{-1/2}, \tag{2.23}$$

$$\gamma_n = \left(1 - \gamma_{ij}U^iU^j\right)^{-1/2}, \tag{2.24}$$

$$U_0^i = \frac{\beta^i}{\alpha}. \tag{2.25}$$

The 3-velocity U^i is defined by

$$u^\mu = \gamma_n(n^\mu + U^\mu), \tag{2.26}$$

$$U^\mu n_\mu = 0. \tag{2.27}$$

The choice of U^i, which is unconstrained in this formalism, is an important component is determining the initial conditions in the neutron star. For irrotational binaries (non-

spinning neutron stars), there exists a potential ϕ such that

$$U^i = \frac{\Psi^{-4}\tilde{\gamma}^{ij}}{h\gamma_n}\partial_j\phi. \tag{2.28}$$

The continuity equation can then be written as a second-order elliptic equation for ϕ:

$$\frac{\rho_0}{h}\nabla^\mu\nabla_\mu\phi + (\nabla^\mu\phi)\,\nabla_\mu\frac{\rho_0}{h} = 0. \tag{2.29}$$

Under the assumption of the existence of an approximate helicoidal Killing vector ξ Teukolsky (1998); Shibata (1998), this equation becomes

$$\rho_0\left\{-\tilde{\gamma}^{ij}\partial_i\partial_j\phi + \frac{h\beta^i\Psi^4}{\alpha}\partial_i\gamma_n + hK\gamma_n\Psi^4\right.$$
$$\left. + \left[\tilde{\gamma}^{ij}\tilde{\Gamma}^k_{ij} + \gamma^{ik}\partial_i\left(\ln\frac{h}{\alpha\Psi^2}\right)\right]\partial_k\phi\right\}$$
$$= \tilde{\gamma}^{ij}\partial_i\phi\partial_j\rho_0 - \frac{h\gamma_n\beta^i\Psi^4}{\alpha}\partial_i\rho_0. \tag{2.30}$$

Another simple choice for U^i is to enforce corotation of the star, i.e. $U^i = U^i_0$. This would be the case if neutron star binaries were tidally locked. However, viscous forces in neutron stars are expected to be insufficient to impose tidal locking Bildsten & Cutler (1992), and the neutron star spins probably remain close to their value at large orbital separations.

Once we have obtained h from the metric and U^i, the other hydrodynamical variables can be recovered if we close the system by the choice of an equation of state for cold neutron star matter in β-equilibrium, $P = P(\rho_0)$ and $\epsilon = \epsilon(\rho_0)$. Throughout this work, we use a polytropic equation of state, $P = \kappa\rho_0^\Gamma$, with $\Gamma = 2$. The internal energy, $\epsilon\rho_0$, satisfies

$$\epsilon\rho_0 = \frac{P}{\Gamma - 1}. \tag{2.31}$$

The boundary conditions of our system of equations are quite simple. At the outer boundary of the computational domain (which we approximate as "infinity" and is in practice $10^{10}M_\odot$), we require the metric to be Minkowski in the inertial frame, and so in

the corotating frame we have

$$\boldsymbol{\beta} = \boldsymbol{\Omega}_0 \times \boldsymbol{r} + \dot{a}_0 \boldsymbol{r}, \tag{2.32}$$

$$\alpha = 1, \tag{2.33}$$

$$\Psi = 1, \tag{2.34}$$

with $\boldsymbol{\Omega}_0$ the initial orbital frequency of the binary and $\dot{a}_0$ the initial inspiral rate of the binary. We choose $\boldsymbol{\Omega}_0 = (0, 0, \Omega_0)$, with Ω_0 and $\dot{a}_0$ as freely specifiable variables that determine the initial eccentricity of the binary.

At the surface of each star, the boundary condition can be easily inferred from the $\rho_0 = 0$ limit of equation (2.30):

$$\tilde{\gamma}^{ij} \partial_i \phi \partial_j \rho_0 = \frac{h \gamma_n \beta^i \Psi^4}{\alpha} \partial_i \rho_0. \tag{2.35}$$

Finally, we discuss how a first guess for the orbital angular velocity Ω_0 can be obtained for a non-spinning system. The force balance equation at the centre of the NS is

$$\nabla \ln h = 0. \tag{2.36}$$

Neglecting any infall velocity, this condition guarantees that the binary is in a circular orbit. This is only an approximation as there is really some infall velocity, but this still leads to low eccentricity binaries with $e \sim 0.01$. From the integrated Euler equation, we can write this condition as

$$\nabla \ln h = \nabla \left(\ln \frac{\gamma_0}{\alpha \gamma} \right) = 0, \tag{2.37}$$

or, by using the definitions of γ_0, and γ,

$$\nabla \ln \left(\alpha^2 - \gamma_{ij} \beta^i \beta^j \right) = -2 \nabla \ln \gamma. \tag{2.38}$$

If we decompose β^i in its inertial component β_0^i and its comoving component according to

$$\boldsymbol{\beta} = \boldsymbol{\beta}_0 + \boldsymbol{\Omega}_0 \times \boldsymbol{r} + \dot{a}_0 \boldsymbol{r}, \tag{2.39}$$

this can be written as a quadratic equation for the orbital angular velocity Ω_0 (neglecting the dependence of γ on the orbital angular velocity Ω_0). In practice, we solve for Ω_0 by projecting Eq. (2.38) along the line connecting the center of the two stars.[1]

The exact iterative procedure followed to solve in a consistent manner the constraint equations, the elliptic equations for ϕ, and the algebraic equations for h (including on-the-fly computation of Ω_0 and of the constant in the first integral of Euler equation) is detailed in Section 2.3.4.

Once a quasi-equilibrium solution has been obtained by this method, lower eccentricity systems can be generated by modifying Ω_0 and $\dot{a}_0$, following the methods developed by Pfeiffer et al. Pfeiffer et al. (2007).

2.3.2 Formalism for Spinning Binaries

We will now discuss how to alter the formalism discussed above to incorporate spinning BNS. Although several formalisms have been introduced in the past Marronetti & Shapiro (2003)Baumgarte & Shapiro (2009), we will follow the work of Tichy (2011)Tichy (2011). A first obvious difference is that we can no longer write the velocity solely in terms of the gradient of a potential. Following Tichy, we break the velocity up into an irrotational part, and a new rotational part W:

$$U^i = \frac{\Psi^{-4}\tilde{\gamma}^{ij}}{h\gamma_n}\left(\partial_j\phi + W_j\right),\tag{2.40}$$

where it is natural, although not required, for W to be divergenceless.

Following the assumptions stated in TichyTichy (2011), the continuity equation be-

---

[1]Along the other directions, the enthalpy h is corrected so that force balance is enforced at the center of the star, according to the method described in Foucart et al. (2011)

comes

$$\rho_0 \left\{ -\tilde{\gamma}^{ij}\partial_i\left(\partial_j\phi + W_j\right) + \frac{h\beta^i\Psi^4}{\alpha}\partial_i\gamma_n + hK\gamma_n\Psi^4 \right.$$
$$\left. + \left[\tilde{\gamma}^{ij}\tilde{\Gamma}^k_{ij} + \gamma^{ik}\partial_i\left(\ln\frac{h}{\alpha\Psi^2}\right)\right]\left(\partial_k\phi + W_k\right)\right\}$$
$$= \tilde{\gamma}^{ij}\left(\partial_i\phi + W_i\right)\partial_j\rho_0 - \frac{h\gamma_n\beta^i\Psi^4}{\alpha}\partial_i\rho_0. \tag{2.41}$$

Eq. 4.29 then is the same as in the irrotational case, cf. Eq. 2.30, under the replacement $\partial_i\phi \to \partial_i\phi + W_i$.

Taking the limit $\rho_0 \to 0$ in Eq. (4.29) yields the boundary condition at the surface of each star:

$$\tilde{\gamma}^{ij}\left(\partial_i\phi + W_i\right)\partial_j\rho_0 = \frac{h\gamma_n\beta^i\Psi^4}{\alpha}\partial_i\rho_0. \tag{2.42}$$

The solution of the Euler equation is no longer as simple as it was previously, in Eq. 2.20. As shown in Tichy(2011)Tichy (2011), the solution is now

$$h = \sqrt{L^2 - \left(\nabla_i\phi + W_i\right)\left(\nabla^i\phi + W^i\right)}, \tag{2.43}$$

where

$$L^2 = \frac{b + \sqrt{b^2 - 4\alpha^4\left(\left(\nabla_i\phi + W_i\right)W^i\right)^2}}{2\alpha^2}, \tag{2.44}$$

and

$$b = \left(\beta^i\nabla_i\phi + C\right)^2 + 2\alpha^2\left(\nabla_i\phi + w_i\right)w^i. \tag{2.45}$$

Finally, the method discussed previously of modifying the star's angular velocity is now no longer as simple. The equation is modified to

$$\nabla\ln\left(\alpha^2 - \gamma_{ij}\beta^i\beta^j\right) = -2\nabla\ln\Gamma, \tag{2.46}$$

where

$$\Gamma = \frac{\gamma_n\left(1 - \left(\beta^i + \frac{W^i\alpha}{h\gamma_n}\right)\frac{\nabla_i\phi}{\alpha h\gamma_n} - \frac{W_iW^i}{\alpha^2\gamma_n^2}\right)}{\sqrt{1 - \left(\frac{\beta^i}{\alpha} + \frac{W^i}{h\gamma_n}\right)\left(\frac{\beta_i}{\alpha} + \frac{W_i}{h\gamma_n}\right)}}. \tag{2.47}$$

Let us now discuss the choice of the spin term, W. This term is, in principle, freely chosen, and so we must choose it so as to best represent the physical situation at hand - namely a uniform rotation with constant angular velocity. As suggested by Tichy(2011)Tichy (2011) and Tichy(2012)Tichy (2012), a reasonable choice for W is

$$W^i = \epsilon^{ijk}\omega^j r^k, \tag{2.48}$$

where r^k is the position vector centered at the star's centre, ω^j represents an angular velocity vector and $\epsilon^{ijk} = \{\pm 1, 0\}$. This leads to a vector field W^i with vanishing divergence in the conformal metric $\tilde{g}_{ij} = \delta_{ij}$. Alternatively, one might prefer a vector field V^i with vanishing divergence with respect to the physical metric $g_{ij} = \Psi^4\delta_{ij}$. Owing to the conformal transformation properties of the divergence operator, V^i is given by

$$V^i = \Psi^{-6}W^i. \tag{2.49}$$

Here, we generally use W^i as we have found that it leads to initial data which is closer to being in equilibrium, as we will further discuss in section 2.5.5.

2.3.3 Solving the elliptic equations

In the previous sections, we have reduced the Einstein constraints, Eqs. (4.17)–(4.19), as well as the continuity equation (4.29) to elliptic equations. We solve these equations with the multi-domain pseudo-spectral elliptic solver developed in Pfeiffer et al. (2003), as modified in Foucart et al. (2008) for matter. The computational domain is subdivided into individual subdomains as indicated in Fig. 2.1: The region near the center of each star is covered by a cube, overlapping the cube is a spherical shell which covers the outer layers of the star. The outer boundary of this shell is deformed to conform to the surface of the star. This places all surfaces at which the solution is not smooth at a subdomain-boundary, which preserves the exponential convergence of spectral methods. Another spherical shell surrounds each star. The inner shells representing the stars and their
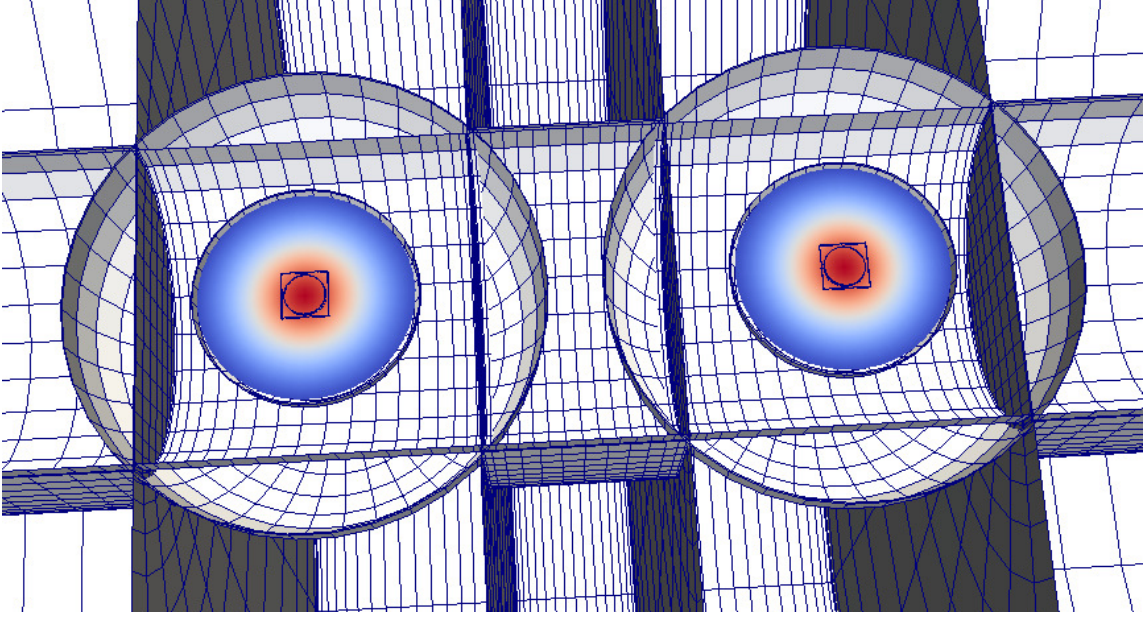
Figure 2.1: Visualization in the x-y plane of the domain decomposition used in our initial data solve. The colour map represents the density of the stars.

vicinity are embedded into a structure of five concentric cylinders with three rectangular blocks along the axis connecting the centers of the neutron stars, which overlap the inner spherical shells. The cylinders/blocks in turn are overlapped at large radius by one further spherical shell centered half-way between the two neutron stars. Using an inverse radial mapping, the outer radius of the outer sphere is placed at 10^{10}.

All variables are decomposed on sets of basis functions depending on the subdomain. The resolution of each domain (i.e., the number of colocation points used) is chosen at the start of the initial data solve, and then subsequently modified several times using an adaptive procedure described below. In this paper, when discussing the total resolution of the domain, we use the notation

$$N^{1/3} = \left(\sum N_i \right)^{1/3}, \tag{2.50}$$

with N_i the number of collocation points in the ith subdomain. $N^{1/3}$ is thus the cube root of the total number of collaction points in all subdomains.

2.3.4 Construction of quasi-equilibrium initial data

Construction of initial data for rotating binary neutron stars begins with selecting the physical properties of the system: the equation of state of nuclear matter, the coordinate separation d between the neutron stars, the baryon masses M_1^b and M_2^b of the two stars, and their spin vectors $\boldsymbol{\omega}_{\mathrm{rot},1}$ and $\boldsymbol{\omega}_{\mathrm{rot},2}$. We also choose the orbital angular frequency Ω_0 and the initial inspiral rate $\dot{a}_0$.

We generally begin by setting Ω_0 to the value for the orbital frequency of a similar irrotational BNS (where Ω_0 is determined by the condition of quasi-circularity, Eq. (2.36)), and $\dot{a}_0 = 0$. These values are then adjusted following the eccentricity reduction method developed by Pfeiffer et al. Pfeiffer et al. (2007). Finally, we use a flat conformal metric, $\tilde{\gamma}_{ij} = \delta_{ij}$, and maximal slicing, $K = 0$.

Once all these quantities are fixed, we need to solve self-consistently Eqs. (4.17)–(4.19) for the Einstein-constraints, the continuity equation Eq. (4.29), while simultaneously satisfying conditions to enforce the desired masses of the stars. To do so, we follow an iterative procedure developed originally for black hole-neutron star binaries Foucart et al. (2012).

First, we choose initial guesses for the conformal metric and hydrodynamical variables, using an analytical superposition of two isolated boosted neutron stars.

We then obtain constraint-satisfying initial conditions by applying the following iterative procedure, where n represents the iteration number:

1. Solve the nonlinear XCTS system for the set of metric variables $X = (\beta^i, \Psi, \alpha\Psi)$, assuming fixed values of the conformal source terms $(\tilde{E}, \tilde{S}, \tilde{J}^i)$. The new value X^{n+1} of the metric variables is obtained from their old value X^n and, following the relaxation scheme used in Foucart et al. (2008), the solution of the XCTS equations X^*, using

$$X^{n+1} = 0.3X^* + 0.7X^n. \tag{2.51}$$

2. Locate the surface of each star. Representing the surface in polar coordinates centered on each star as $R_s^n(\theta, \phi)$, we determine R_s^n to satisfy Foucart et al. (2008) $h(R_s^n(\theta, \phi), \theta, \phi) = 1$. To ensures that the grid-boundary R_b converges to the surface of the star, we occassionally modify the numerical grid such that $R_b(\theta, \phi) = R_s^n(\theta, \phi)$. Because this requires a re-initialization of the elliptic solver, the grid is only modified if the stellar surface has settled down, specifically, if

$$||R_s^n - R_s^{n-1}|| < 0.1||R_s^n - R_b||. \tag{2.52}$$

Here $|| \, . \, ||_2$ denotes the L2-norm over the surface.

3. For each neutron star, fix the constant in Euler's first integral so that the baryon mass of the neutron star matches the desired value. We compute the baryon mass as a function of the Euler constant C through

$$M_{NS}^b = \int_{NS} \rho_0 \Psi^6 \sqrt{\frac{1}{1 - \gamma_{ij}U^iU^j}} dV, \tag{2.53}$$

and utilize the secant method to drive the mass to the desired value.

4. If desired, adjust the orbital frequency to ensure force-balance at the center of each star by solving Eq. (2.38). This step is skipped if the orbital frequency is fixed through iterative eccentricity removal, cf. Sec. 2.5.2.

5. Solve the elliptic equation for the velocity potential ϕ, and obtain the next guess for ϕ using the same relaxation method shown in Eq. 2.51.

6. Check whether all equations are satisfied to the desired accuracy. If yes, proceed. If no, return to Step 1.

7. Compute the truncation error of the current solution by examining the spectral expansion of the XCTS variables. If this truncation error is undesirably large (typically, if it is $> 10^{-9}$), then adjust the number of grid-points in the domain-decomposition and return to Step 1. The adjustment is based on the desired target

truncation eror and the measured convergence rate of the solution, cf. Szilágyi
(2014).

2.3.5 Quasi-Local Angular Momentum

The goal of the present paper is to construct spinning BNS initial data and to evolve
it. Therefore, we need diagnostics to measure the NS spin, for which we use techniques
originally developed for black holes. It is common to discuss the spins of black holes in
terms of their dimensionless spin χ,

$$\chi = \frac{S}{M^2}. \tag{2.54}$$

Here, S is the angular momentum of the black hole, and M is its Christodoulou mass Christodoulou
(1970),

$$M^2 = M_{\mathrm{irr}}^2 + \frac{S^2}{4M_{\mathrm{irr}}^2}. \tag{2.55}$$

The irreducible mass M_{irr} is defined based on the area of the hole's apparent horizon,
$M_{\mathrm{irr}} = \sqrt{A/16\pi}$. The angular momentum is computed with a surface integral over the
apparent horizon Brown & York (1993); Ashtekar et al. (2001); Ashtekar & Krishnan
(2003),

$$S = \frac{1}{8\pi} \oint_{\mathcal{H}} \phi^i s^j K_{ij} dA \tag{2.56}$$

where $\mathcal{H}$ is the black hole's apparent horizon, s^j is the outward-pointing unit-normal to
$\mathcal{H}$ within the $t = \mathrm{const}$ hypersurface, and ϕ^i is an azimuthal vector field tangent to $\mathcal{H}$.
For spacetimes with axisymmetry, ϕ^i should be chosen as the rotational Killing vector. In
spacetimes without an exact rotational symmetry (e.g. the spacetime of a binary black
hole system), one substitutes an approximate Killing vectorCook & Whiting (2007);
Lovelace et al. (2008) (AKV). Ref. Lovelace et al. (2008) introduces a minimization
principle to define ϕ^i, resulting in an Eigenvalue problem. The three eigenvectors with
the lowest eigenvalues (i.e. smallest shear) are taken and used to compute the three
components of the spin.

In this paper, we explore the application of quasi-local spin measures to neutron stars. In the absence of apparent horizons $\mathcal{H}$, we need to choose different surface(s) to evaluate Eq. (2.56).

When constructing initial data, the stellar surface $\mathcal{S}$ is already determined, so one obvious choice is to integrate over the stellar surface $\mathcal{S}$. To estimate the ambiguity in quasi-local spin, we furthermore compute S by integrating over coordinate spheres with radii ranging from just outside $\mathcal{S}$ to larger by about 70%. During the evolution, the stars change shape and may even loose mass in tidal tails. Because of these complications, the SpEC evolution code does not track the location of the stellar surface during the evolution, and we shall only monitor S on coordinate spheres.

It is useful to compute a dimensionless spin χ, for instance, for post-Newtonian comparisons. In the absence of a horizon, Eq. (2.55) is meaningless and we need a different choice for the mass-normalization. Instead, we normalize by each star's ADM mass, M_{ADM}, i.e.

$$\chi \equiv \frac{S}{M_{\mathrm{ADM}}^2}. \tag{2.57}$$

The ADM mass is determined by computing the ADM mass of an equilibrium configuration of a single uniformly rotating polytrope in isolation with the same baryon mass and angular momentum as those measured in our binary systems.

The results of the quasi-local spin measures are described in section 2.4.4, which shows that this procedure is numerically robust.

Finally, let us discuss, from an order of magnitude perspective, how the star's dimensionless spin is related to its more commonly used physical properties. We start with the Newtonian relation $S = 2\pi I/P$ between angular momentum S, moment of inertia I, and rotational period P. Writing further $I = f R^2 M$, with the dimensionless constant

f depending on the stellar density profile, we have

$$
\chi \sim \frac{2\pi c}{G} \frac{f R^2}{P M}
$$
$$
= 0.48 \left(\frac{f}{0.33}\right) \left(\frac{R}{12\text{km}}\right)^2 \left(\frac{M}{1.4 M_\odot}\right)^{-1} \left(\frac{P}{1\text{ms}}\right)^{-1}. \tag{2.58}
$$

The factor c/G arises from the transition to geometric units.

This –quite simplistic– estimate shows that millisecond pulsars will have appreciable dimensionless spin χ. Centrifugal breakup of rapidly rotating neutron stars happens at a dimensionless spin in the range $0.65 - 0.70$ Lo & Lin (2011), with only small dependence on the equation of state and neutron star mass. Ansorg et al Ansorg et al. (2003) studied in detail $\Gamma = 2$ polytropes, the equation of state we use here. Ref. Ansorg et al. (2003) finds a dimensionless spin at mass-shedding of $\chi = 0.57$.

2.4 Initial Data Results

In this section, we will demonstrate that our code can robustly construct contraint-satisfying initial data for BNS systems with arbitrary spins. As discussed in section 2.3.4, our code consists of a solver that runs for a number of iterations at constant resolution, and then the resolution is increased and this process restarts. We will therefore demonstrate that appropriate quantities converge with both the iterations of iterative scheme described above in Section 2.3.4 and with resolution as the resolution increases.

2.4.1 Convergence of the Iterative Procedure

At each step of the iterative procedure, the Euler constant of each star is modified to achieve a desired stellar baryon mass, based on the current matter distribution inside the star. We expect that the Euler constant converges during the iterations at a fixed resolution. Figure 2.2 shows the behavior of the Euler Constant during iterations at the lowest initial data resolution, R0. We show three runs of interest, one with large aligned

Name	M_{NS}^b	$\boldsymbol{\omega}$	D_0	$\Omega_0 \times 10^3$	$\dot{a}_0 \times 10^5$	M_{ADM}	$\vec{\chi}$
S.4z	1.7745	$0.01525\hat{z}$	47.2	5.09594	-1.75	1.648	$0.3765\hat{z}$
S-.05z	1.7745	$-0.00273\hat{z}$	47.2	5.11769	-1.71	1.640	$-0.05018\hat{z}$
S.4x	1.7745	$0.01525\hat{x}$	47.2	5.10064	-2.36	1.648	$0.3714\hat{x}$

Table 2.1: Parameters for the initial data sets used in testing the initial data solver: M_{NS}^b and ω^i are baryon mass and rotational parameter for either neutron star (the same values are used); D_0, Ω_0 and $\dot{a}_0$ represent coordinate separation between the centers of the stars, the orbital frequency, and the radial expansion; $\vec{\chi}$ is the dimensionless spin vector computed from the initial data set. In each case we use a polytropic equation of state, $P = \kappa \rho_0^{\Gamma}$, with $\Gamma = 2$ and $\kappa = 123.6$.

spins (S.4z), one with large precessing spin (S.4x), and one with small anti-aligned spins (S-.05z). The properties of these configurations are shown in table 2.1. In all three cases we see agreement between neighboring iterations at the $10^{-5} - 10^{-6}$ level by the end of iterating at this resolution. At the highest resolutions, these differences are down to, typically, the $10^{-9} - 10^{-10}$ level. This can be compared to Fig. 3 of Gourgoulhon et al. (2001). Although not shown here, other free quantities converge similarly to the Euler constant.

2.4.2 Convergence of the Solution

Having established that our iterative procedure converges as intended, we now turn out attention to the convergence of the solution with resolution. To demonstrate it, we will look at the Hamiltonian and momentum constraints, and the differences between measured physical quantities - the ADM energy and ADM angular momentum, and the surface fitting coefficients of the stars. As our initial data representation is fully spectral, we expect that these quantities should converge exponentially with resolution. Note that when we discuss the value of a quantity at a certain resolution, we are referring to the
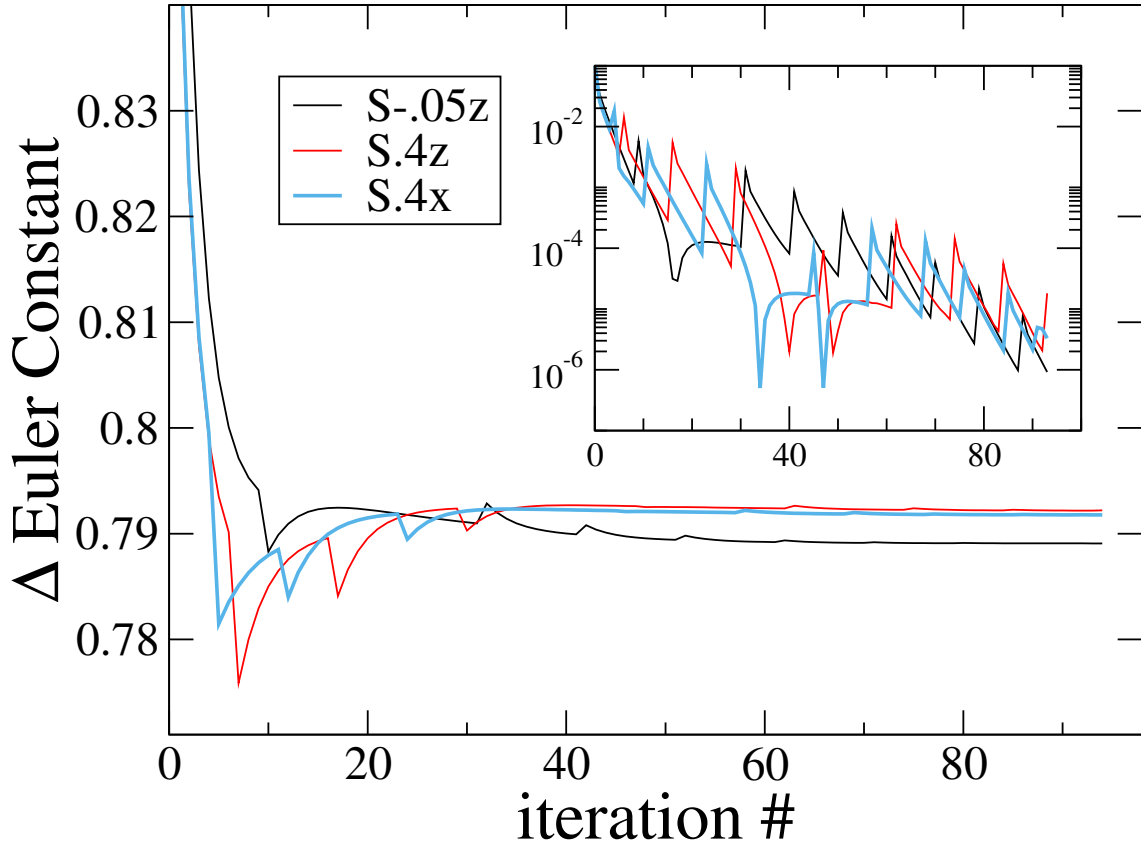
Figure 2.2: Convergence of the Euler constant during iteration at the lowest resolution R0. The inset shows the difference between values at subsequent iterations.

value of that quantity after the final iterative step at that resolution.

Figure 2.3 shows the convergence of the Hamiltonian constraint and the Momentum constraint for our three runs of interest. These are computed during the last iterative solve at each resolution. The data plotted are computed as

$$H = ||\frac{R_\Psi}{8\Psi^5}||, \tag{2.59}$$

$$M = ||\frac{R_\beta}{2\alpha\Psi^4}||. \tag{2.60}$$

Here R_Ψ and R_β denote the residuals of Eqs. (4.18) and (4.17), respectively, and $||.||$ represents the root-mean-square value over grid-points of the entire computational grid. This plot demonstrates that our initial data solver converges exponentially with resolution, even for very high spins, which gives confidence that we are indeed correctly solving the Einstein Field Equations.

The surface of the star is represented by a spherical harmonic expansion:

$$R_s(\theta, \phi) = \sum_{l,m}^{l_{\max}, m_{\max}} c_{lm} Y_{lm}(\theta, \phi), \tag{2.61}$$

where $l_{\max} = m_{\max} = 11$, unless stated otherwise. The stellar surface is located by finding a constant enthalpy surface, cf. Sec. 2.3.4, and the spherical subdomains that cover the star are deformed to conform to $R_s(\theta, \phi)$. To establish convergence of the position of the stellar surface we introduce the quantity

$$\Delta c(i) = \frac{1}{l(l+1)} \sqrt{\sum_{l,m}^{l_{\max}, m_{\max}} (c_{lm}(i) - c_{lm}(N))^2}. \tag{2.62}$$

Here i refers to the ith resolution in the initial data, and N refers to the final resolution. Figure 2.4 plots $\Delta c(i)$ vs. resolution. The surface location converges exponentially to better than 10^{-8}.

Finally, we assess the overall convergence of the solution through the global quantities E_{ADM} and $|J^i_{\text{ADM}}|$. The surface integrals at infinity in these two quantities are recast using
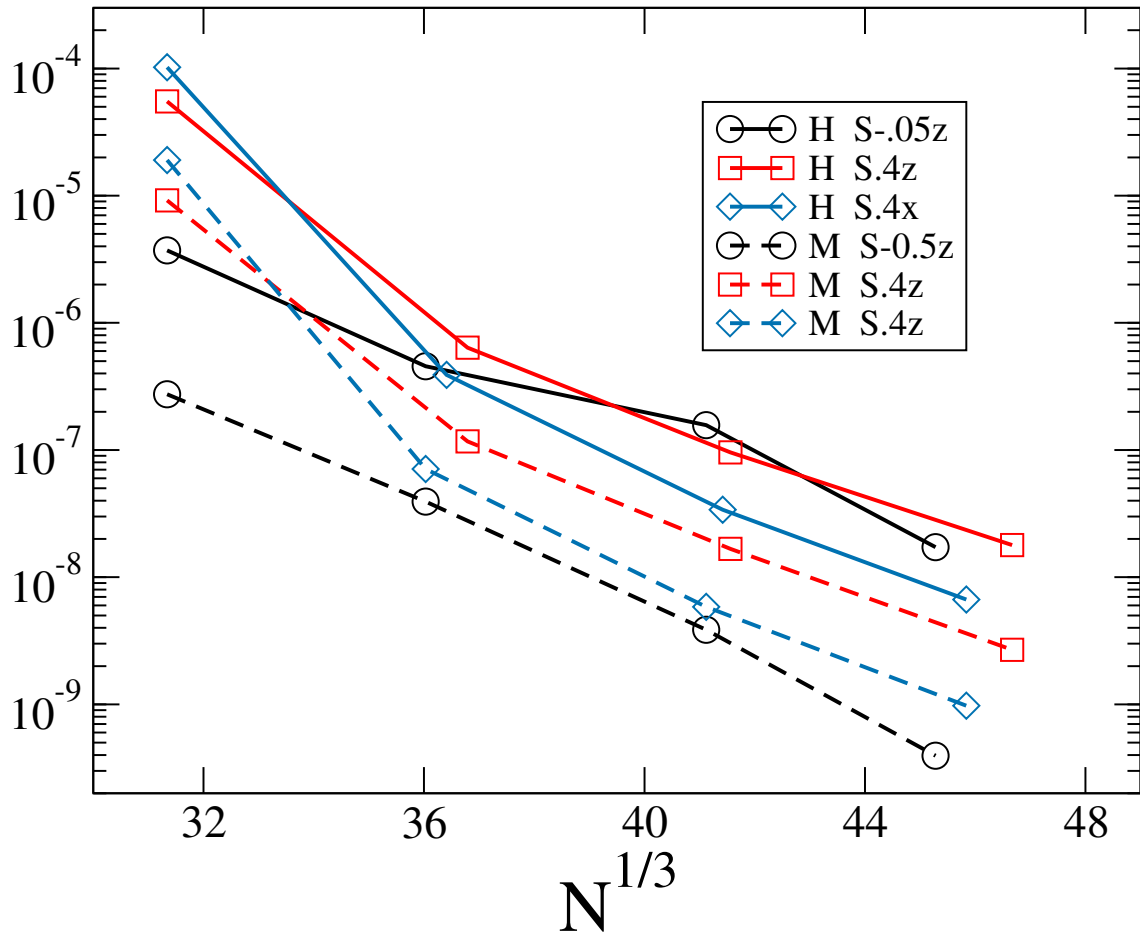
Figure 2.3: Hamiltonian and Momentum constraints as a function of resolution N. We see exponential convergence in all cases.
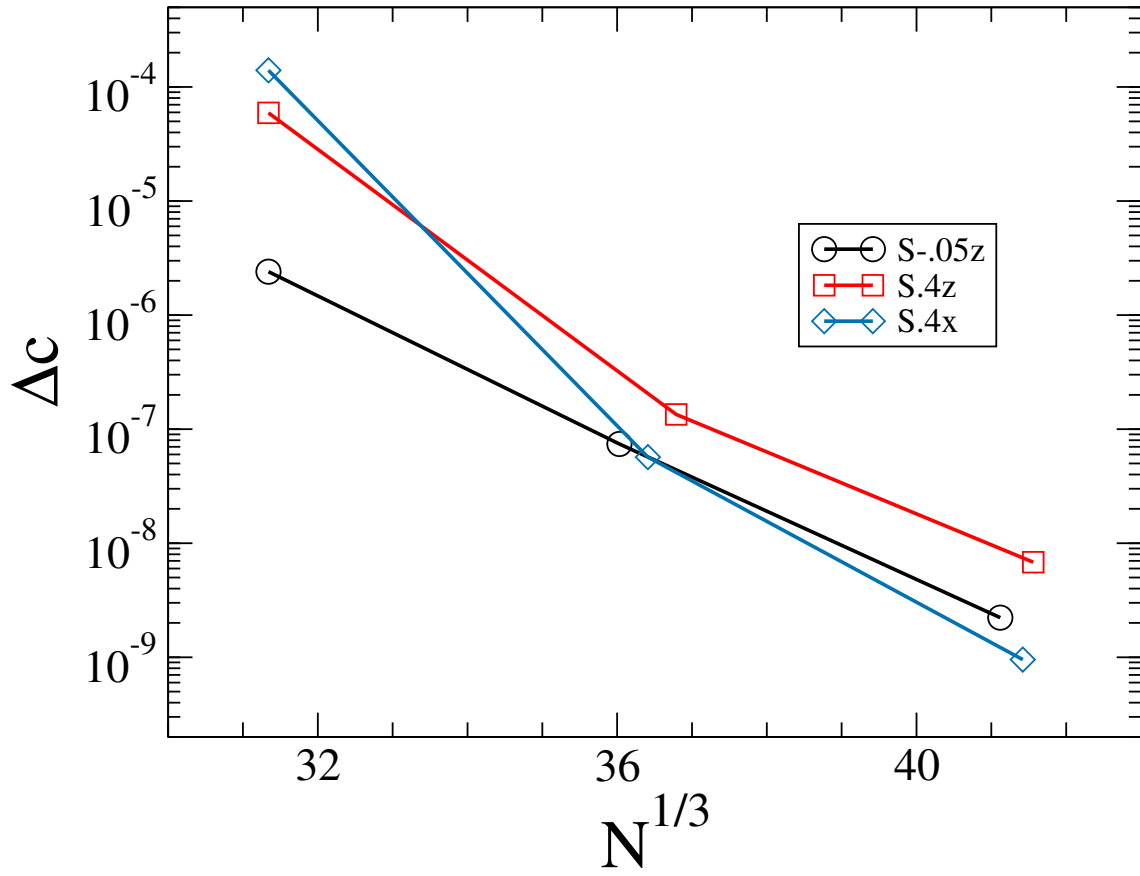
Figure 2.4: Convergence of the location of the stellar surface. Plotted is Δc as defined in Eq.(2.62), for three representative configurations.

Gauss' law (cf. Foucart et al. (2008)):

$$E_{\text{ADM}} = -\frac{1}{2\pi} \oint_{S_\infty} \delta^i_j \partial_i \Psi \, dS_j$$
$$= -\frac{1}{2\pi} \oint_S \delta^i_j \partial_i \Psi \, dS^j + \frac{1}{2\pi} \int_{\mathcal{V}} \delta^{ij} \partial_i \partial_j \Psi \, dV, \tag{2.63}$$

and

$$J^z_{\text{ADM}} = \frac{1}{8\pi} \oint_{S_\infty} \left(x K^{yj} - y K^{xj} \right) dS_j$$
$$= \frac{1}{8\pi} \oint_S \left(x K_{yi} - y K_{xi} \right) \delta^{ij} \Psi^2 \, dS_j. \tag{2.64}$$

Here $\mathcal{V}$ is the volume outside S, and the integrals are evaluated in the flat conformal space. To obtain the other components of J^i_{ADM}, cyclically permute the indices x,y,z. We define the quantities ΔE and ΔJ as the absolute fractional difference in these quantities between the current resolution and the next highest resolution. These are plotted in figure 6.5. In general, we find agreement at the $10^{-7} - 10^{-8}$ level by the final resolution.

2.4.3 Convergence of the quasi-local spin

We now turn to the angular momentum of the neutron stars, as measured with quasi-local angular momentum integrals on the stellar surface. We will discuss dimensionless spins χ, which depend on two distinct numerical resolutions: First, the resolution of the 3-dimensional grid used for solving the initial value equations. This resolution is specified in terms of N, the total number of grid-points. Second, the resolution used when solving the eigenvalue problem for approximate Killing vectors on the 2-dimensional surface, as given by L, the expansion order in spherical harmonics of the surface-parameterization $r_S(\theta, \phi) = \sum_{l=0}^{L} \sum_m r_{lm} Y^{lm}(\theta, \phi)$.

Throughout this paper, we use $L = 11$. The top panel of Fig. 2.6 shows convergence of χ with grid-resolution N, at fixed $L = 11$. We find near exponential convergence.

The influence of our choice $L = 11$ is examined in the lower panel by computing the quasi-local spin at lower resolution $L = 8$ and at higher resolution $L = 14$. Changing
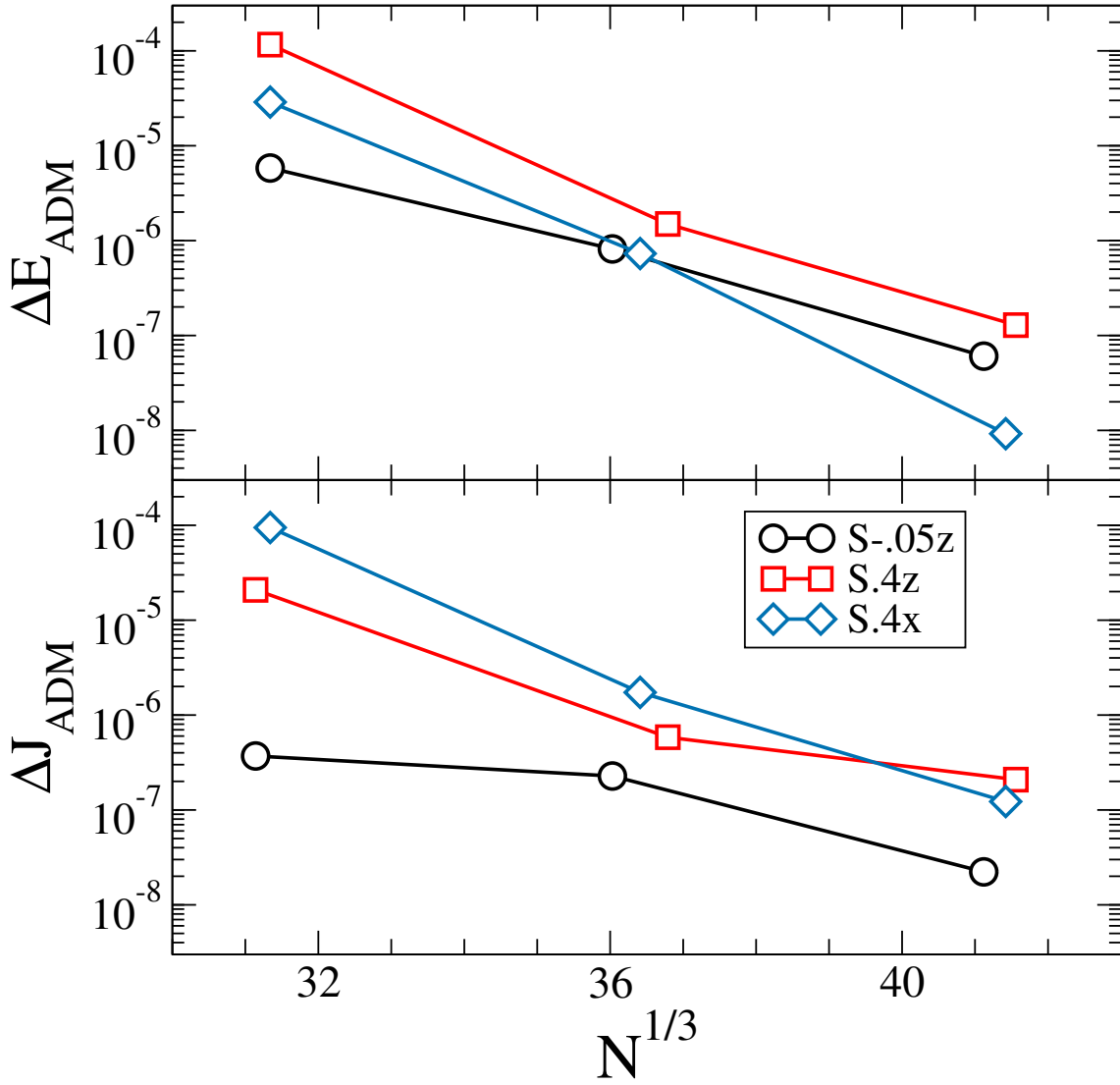
Figure 2.5: Convergence of ADM-energy and the magnitude of the ADM-angular momentum. Shown are the fractional differences between neighboring resolutions, as a function of the lower resolution.
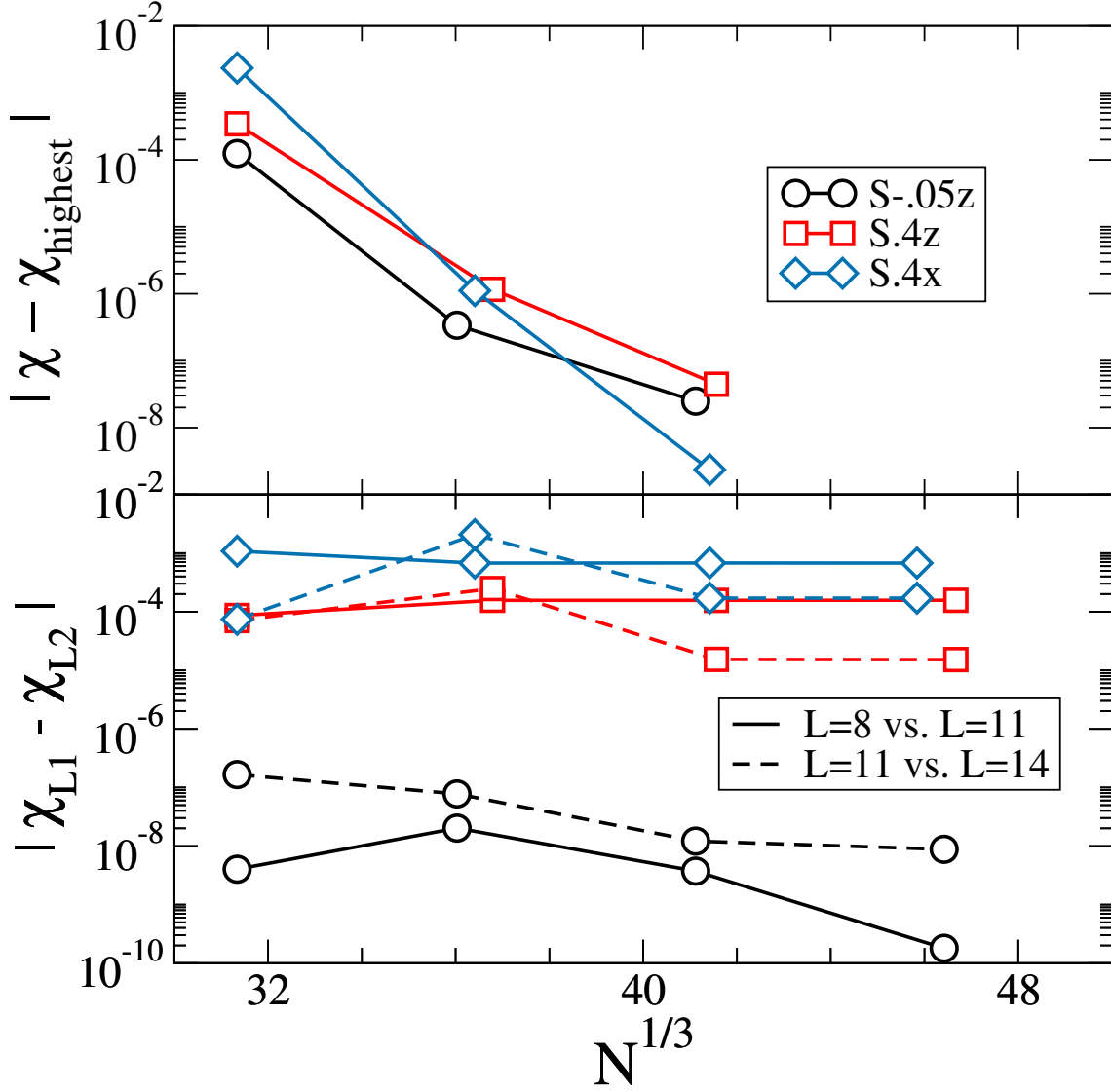
Figure 2.6: Convergence of the quasi-local spin computation. **Top panel:** difference of spin computed at resolution N with the spin computed at the highest resolution. **Bottom panel:** Difference between spins computed at different resolution L of the spin-computation. For `S-.5z`, we achieve an accuracy of $\sim 10^{-7}$, whereas for `S.4z` and `S.4x`, the accuracy is $\sim 10^{-4}$ due to finite L.
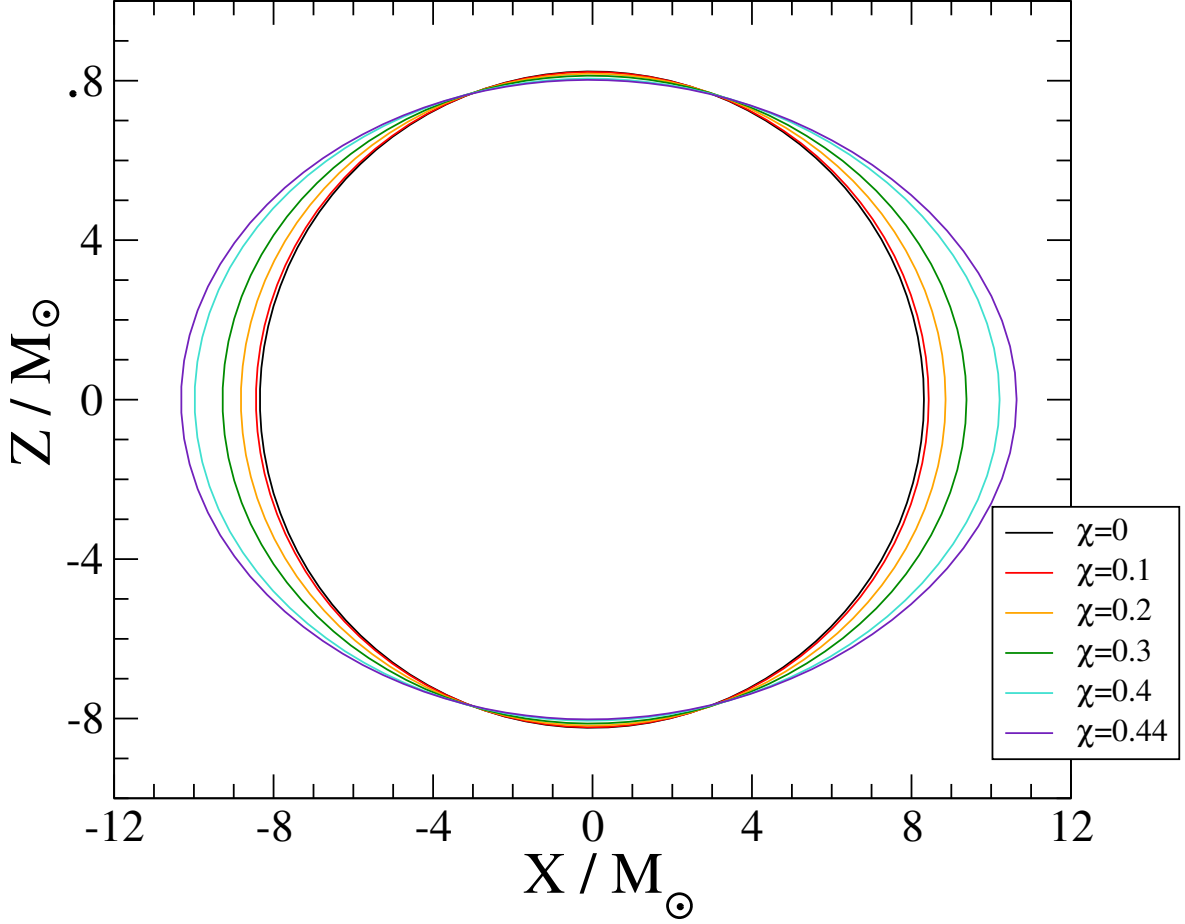
Figure 2.7: Stellar cross-sections in the X-Z plane for a series of different spins, aligned with the $\hat{z}$ axis, demonstrating that they bulge at the equator in the expected way with increasing spin.

L impacts χ by $\sim 10^{-8}$ for the low-spin case S-.05z, and by $\sim 10^{-4}$ for the high-spin cases S.4z and S.4x. For the high-spin cases, the spin measurement is convergent with increasing L, and the finite value of L dominates the error budget. For the low-spin case, numerical truncation error dominates the error budget and convergence with L is not visible. High NS spin leads to a more distorted stellar surface, and so a fixed $L = 11$ yields a spin result of lower accuracy. However, in all cases the the numerical errors of our spin measurements are still neglible for our purposes.

2.4.4 Quasi-local Spin

As discussed in section 2.3.5, we use a quasi-local spin to define the angular momentum carried by each neutron star. To our knowledge, this is the first application of this method to neutron stars in binaries.

In this section, we explore properties of the rotating BNS initial datasets and the employed quasi-local spin diagnostic.

To explore the spin-dependence of BNS initial data sets, we construct a sequence of equal-mass, equal-spin BNS binaries, with spins parallel to the orbital angular momentum. We fix the initial data parameters M_{NS}^b, D_0, Ω_0 and $\dot{a}_0$ to their values for a configuration that we will also evolve below (specifically, `S.4z` - Ecc1)

Figure 2.7 shows cross-sections through one of the neutron stars in the xz-plane, i.e. a plane orthogonal to the orbital plane which is intersecting the centers of both stars. With increasing spin, the stars develop an increasing equatorial bulge, an expected consequence of centrifugal forces.

Figure 4.2 presents the dimensionless spin of either neutron star as a function of ω. χ increases monotonically with the rotation parameter ω. The spin χ increases linearly with ω for small ω. For larger ω, the dependence steepens, as the increasing equatorial radius of the stars increase the moment of inertia Worley et al. (2008).

For $\omega = 0.01625 M_\odot^{-1}$ we achieve $\chi = 0.432$, the largest spin we are able to construct. This is reasonably close to the theoretical maximum value for $\Gamma = 2$ polytropes, $\chi \sim 0.57$ Ansorg et al. (2003). Above $\omega = 0.01625 M_\odot^{-1}$, the initial data code fails to converge. The steepening of the χ vs. ω curve is reminiscent of features related to non-uniqueness of solutions of the extended conformal thin sandwich equations Lovelace et al. (2008); Pfeiffer & York Jr. (2005); Baumgarte et al. (2007); Walsh (2007), and it is possible that our failure to find solutions originates in an analogous break-down of the uniqueness of solutions of the constraint equations.

While the focus of our investigation lies on rotating NS, we note that for $\omega = 0$ our
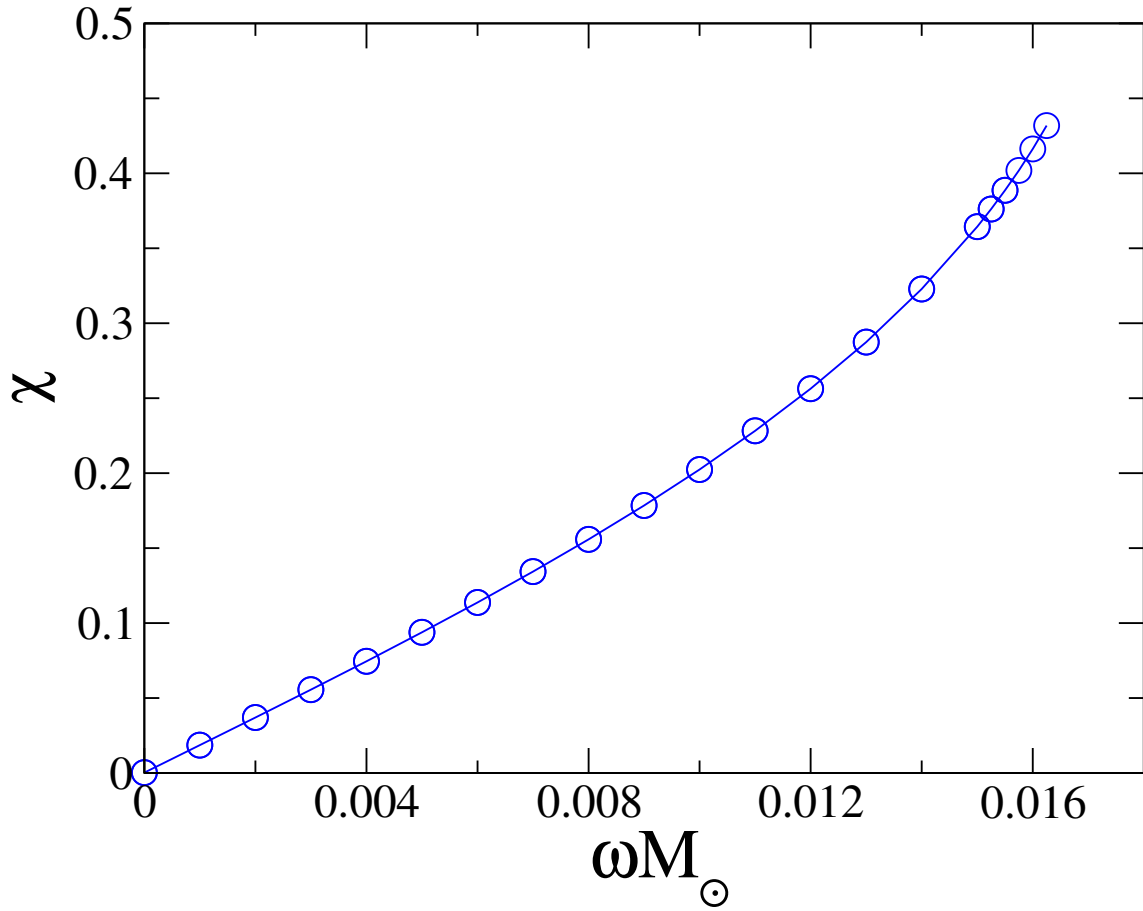
Figure 2.8: Dimensionless angular momentum χ as a function of Ω for a series of spin-aligned initial data sets with the same physical parameters as our runs of interest. We see, as expected, a linear relation between χ and Ω at low-spins, which eventually becomes non-linear at higher spins.

data-sets reduce to the standard formalism for irrotational NS. For $\omega = 0$, we find a quasi-local spin of the neutron stars is $\chi = 2 \times 10^{-4}$. This is the first rigorous measurement of the residual spin of irrotational BNS. Residual spin is, for instance, important for the construction and validation of waveform models for compact object binaries. The analysis in Ref. Boyle et al. (2007) indicates that spins of order 10^{-4} lead to a dephasing of about 0.01radians during the last dozen of inspiral orbits. This value is significantly smaller than the phase accuracy obtained by current BNS simulations, and so the residual spin is presently not a limiting factor for studies like Bernuzzi et al. (2015); Baiotti et al. (2011); Baiotti et al. (2010).

Finally, we demonstrate that the surface on which we compute the quasi-local spin, does not significantly impact the spin we measure: We choose coordinate spheres centered on the neutron star with radius R, and compute the quasi-local spin using these surfaces, rather than the stellar surface.

In Fig. 2.9, we plot the spin measured on various $R = $ const surfaces, for three different values of ω, from the same sequences shown in Fig. 4.2.

The circles denote spins extracted on coordinate spheres. The asterisks indicate the spins computed on the stellar surface. The asterisk is plotted at $R = R_{\mathrm{eq}}$, the equatorial radius of the neutron star under consideration. We find good agreement between spins extracted on coordinate spheres and the spin extracted on the stellar surface, as long as $R \geq R_{\mathrm{eq}}$. The maximum disagreement is seen in the high spin curve, where the two spins differ by $\sim 10^{-2}$.

For $R < R_{\mathrm{eq}}$, the coordinate extraction sphere intersects the outer layers of the neutron star and no longer encompasses the entire matter and angular momentum of the star. Therefore, $\chi(R)$ shows a pronounced decline for $R < R_{\mathrm{eq}}$ for each of the three initial-data sets considered in Fig. 2.9. For $R > R_{\mathrm{eq}}$, $\chi(R)$ continues to increase slightly, for instance, for the middle curve, $\chi(R = 9) = 0.202$ whereas $\chi(R = 11) = 0.204$.

In summary, Fig. 2.9 shows that the quasi-local spin extracted on coordinate spheres can serve as a good approximation of the quasi-local spin extracted on the stellar surface
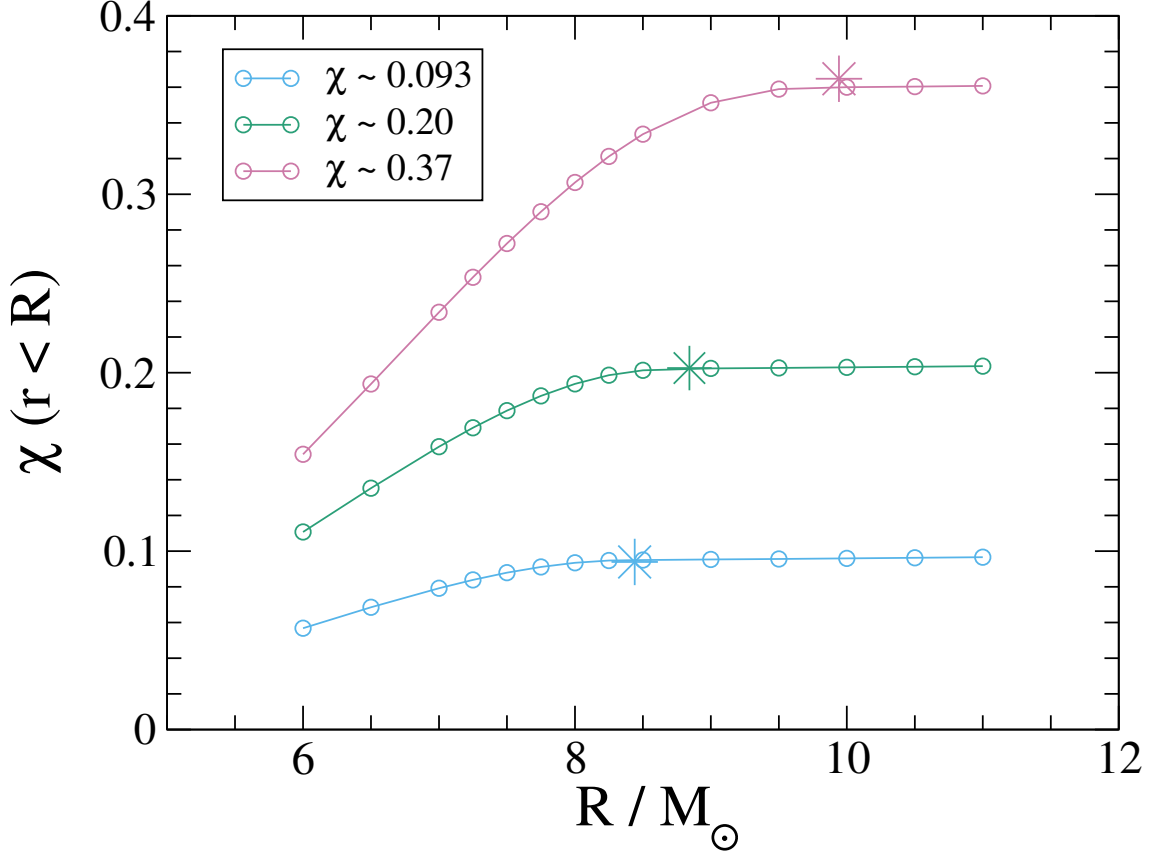
Figure 2.9: Dimensionless spin χ measured on coordinate spheres with radius R for three different aligned spin BNS systems. The asterik denotes the spin measured on the (non-spherical) stellar surface. Circles to the right of the asterik represent coordinate spheres entirely outside the neutron star, and circles on the left of the asterik indicate spin measurement surfaces that intersect the star or are entirely located inside the star.

(as long as the coordiate sphere is outside the star, of course).

This is important because during evolutions of the binary, we do not track the surface of the star. Instead, we will compute the spin on coordinate spheres, similarly to Fig. 2.9.

2.5 Evolution Results

We now evolve the three configurations discussed in Sec. 2.4. As indicated in Table 2.1, all three configurations are equal-mass binaries, with individual ADM masses $M_\star$ (in

Name	k	e	$\vec{\chi}$	$f_0(Hz)$	N_{orb}	$t_f(\mathrm{ms})$
S.4z	0,1,2	$\lesssim 0.001$	$0.381\hat{z}$	167.7	11.8	56.0
S-.05z	0,1,2	0.0006	$-0.050\hat{z}$	165.4	12.5	56.3
S.4x	0,1	$\lesssim 0.002$	$0.375\hat{x}$	164.8	9.1	45.7

Table 2.2: Information about our three evolutions. k indicates the numerical resolutions on which a simulation is performed, e indicates the smallest achieved orbital eccentricity. $\vec{\chi}$ and f_0 are the dimensionless spins at $t = 0$ and the initial orbital frequency. Finally, N_{orb} and t_f represent the number of orbits the configuration was evolved for, and the evolution time.

isolation) of $1.64M_{\odot}$ or $1.648M_{\odot}$ at initial separation of $D = 47.2M_{\odot}$, and using a polytropic equation of state with $\Gamma = 2.0$ and $\kappa = 123.6$. Both stars have equal spins, and the three configurations differ in spin magnitude and spin direction. Configuration S-0.05z has spin-magnitudes ~ 0.05 anti-aligned with the orbital angular momentum, and the confiurations S.4z and S.4x have spin magnitudes near 0.4, along the z-axis and x-axis, respectively.

Each configuration is evolved through $\gtrsim 10$ orbits, into the late-inspiral. In this paper we focus on the inspiral of the neutron stars. Table 2.2 summarizes parameters for these runs.

2.5.1 Evolution Code

In our evolution code, SpEC Buchman et al. (2012); Lovelace et al. (2012); M. A. Scheel, M. Boyle, T. Chu, L. E. Kidder, K. D. Matthews and H. P. Pfeiffer (2009); Kidder et al. (2000); Lindblom et al. (2006); Scheel et al. (2006); Szilágyi et al. (2009); Lovelace et al. (2011); Hemberger et al. (2013); Ossokine et al. (2013), we use a mixed spectral – finite-difference approach to solving the Einstein Field Equations coupled to general relativistic hydrodynamics equations. The equations for the space-time metric, $g_{\mu\nu}$ are solved on a spectral grid, while the fluid equations are solved on a finite difference grid, using a

high-resolution shock-capturing scheme. We use a WENO Jiang & Shu (1996); Liu et al. (1994) reconstruction method to reconstruct primitive variables, and an HLL Riemann solver A. Harten (1983) to compute numerical fluxes at interfaces. Integration is done using a 3rd order Runge-Kutta method with an adaptive stepsize. We interpolate between the hydro and spectral grids at the end of each full time step, interpolating in time to provide data during the Runge-Kutta substeps (see Duez et al. (2008); Foucart et al. (2012); Foucart et al. (2013); Muhlberger et al. (2014) for a more detailed description of the method).

Each star is contained in a separate cubical finite difference grid that does not overlap with that of the other star. The sides of the grids are initially 1.25 times the stars' diameters. We use grids that contain 97^3, 123^3 and 155^3 points for resolutions $k = 0, 1, 2$, respectively[2]. These resolutions correspond to linear grid-spacing of $340\,\mathrm{m}$, $268\,\mathrm{m}$ and $213\,\mathrm{m}$ respectively for the `S.4z` case. The precessing evolution `S.4x` uses similar grid-spacing, whereas the anti-aligned run `S-.05z` has a slightly smaller grid-spacing because the stars themselves are smaller. The region outside the NS but inside the finite difference grid is filled with a low density atmosphere with $\rho = 10^{-13}M_\odot^{-2}$. The motion of the NSs is monitored by computing the centroids of the NS mass distributions

$$X_{\mathrm{CM}}^i = \int x^i u^0 \rho_0 \sqrt{-g^{(4)}} d^3 x \qquad (2.65)$$

for each of the grid patches containing a NS.

The grids are rotated and their separation rescaled to keep the centers of the NS at constant grid-coordinates Scheel et al. (2006); Hemberger et al. (2013); Scheel et al. (2015). As the physical separation between the stars decreases, the rescaling of grid-coordinates therefore causes the size of the stars to increase in grid-coordinates. In order to avoid the stellar surfaces expanding beyond the geometric size of the finite difference grid, we monitor the matter flux leaving this grid along the x, y, and z-direction. If the

---

[2]For aligned-spin configurations `S-.05z` and `S.4z`, we take advantage of, and enforce, z-symmetry, which halves the number of grid-points along the z-axis.

matter flux is too large along a certain axis, we expand the grid in that direction. This procedure allows us to dynamically choose the optimal grid-size that limits matter loss to a small, user-specified level. When changing the size of the hydro grid, the number of grid-points is kept constant, so this process changes the effective resolution during the evolution.

The Einstein field equations are solved on a spectral grid using basis-functions appropriate for the shape of each subdomain. For rectangular blocks, Cheybyshev polynomials are used along each axis; for a spherical shell (i.e. where the center is excised), spherical harmonics in angles, and Chebyshev polynomial in radius are employed; and for an open cylinder (i.e. with the region near the axis excised), Chebyshev polynomials and a Fourier series. For full spheres and filled cylinders, multi-dimensional basis-functions respecting the continuity conditions at the orign/axis are employed Matsushima & Marcus (????); Verkley (1997). For more details see Muhlberger et al. (2014).

More specifically, our spectral grid, the central region of each star is covered by a filled sphere located at the center of the star. These have spherical harmonic modes up to $L = 12 + 2k$. The radial basis-functions are one-sided Jacobi polynomials with $7 + k$ collocation points. The filled spheres are surrounded by eight other spherical shells with the same radial and angular resolutions. At the start of the evolution, the stellar surface is generally located inside the third shell. The far field region is covered by 20 spherical shells starting at 1.5 times the inital binary separation and going out to 40 times that separation. These shells have angular resolution $L = 9 + 2k$ and radial resolution $6 + k$. The region between the innermost shell and the stars is covered by a set of cylindrical shells and filled cylinders.

We use a generalized harmonic evolution system Pretorius (2006; 2005); Lindblom et al. (2006) with coordinates x^μ such that they satisfy a wave equation

$$\nabla^\nu \nabla_\nu x^\mu = H^\mu, \tag{2.66}$$

for some freely-specifiable source function H^μ. The initial source function H^μ_{initial} is

determined by the intial data, assuming that the time derivatives of the lapse and shift functions initially vanish in the corotating frame. We then transition to a pure harmonic gauge, $H^\mu = 0$ by using a transition function, i.e.

$$H^\mu = e^{-(t/\tau)^4} \, H^\mu_{\text{initial}}. \tag{2.67}$$

The timescale τ is determined by $\tau = 2\sqrt{d^3/(2M_\star)}$. This is slow enough to avoid numerical gauge artifacts in the simulations.

2.5.2 Eccentricity Removal

Gravitational wave emission reduces orbital eccentricity rapidly during a GW-driven inspiral Peters & Mathews (1963); Peters (1964). Therefore inspiraling binary neutron stars are expected to have essentially vanishing orbital eccentricity in their late inspiral, unless they recently underwent dynamical interactions. Our goal is to model non-eccentric inspirals. In this subsection we demonstrate that we can indeed control and reduce orbital eccentricty, using the techniques developed for BH-BH binaries Pfeiffer et al. (2007); Boyle et al. (2007); Buonanno et al. (2011) and also applied to BH-NS binaries Foucart et al. (2008).

For fixed binary parameters (masses, spins), and fixed initial separation D_0, the initial orbit of the binary is determined by two remaining parameters: The initial orbital frequency Ω_0, and the initial radial velocity, which we describe through an expansion parameter $\dot{a}_0 = \dot{r}/r$. These two parameters will encode orbital eccentricty and phase of periastron, and our goal is to determine these parameters to reduce orbital eccentricity. We accomplish this using an iterative procedure first introduced for binary black holes Boyle et al. (2007); Buonanno et al. (2011). An initial data set is evolved for a few orbits, the resulting orbital dynamics are analyzed, and then the initial data parameters Ω_0 and $\dot{a}_0$ are adjusted.

For binary neutron stars, we initialize the first iteration of eccentricity removal, with $\dot{a}_0 = 0$ and use Ω_0 determined from irrotational BNS initial data, based on the equilibrium
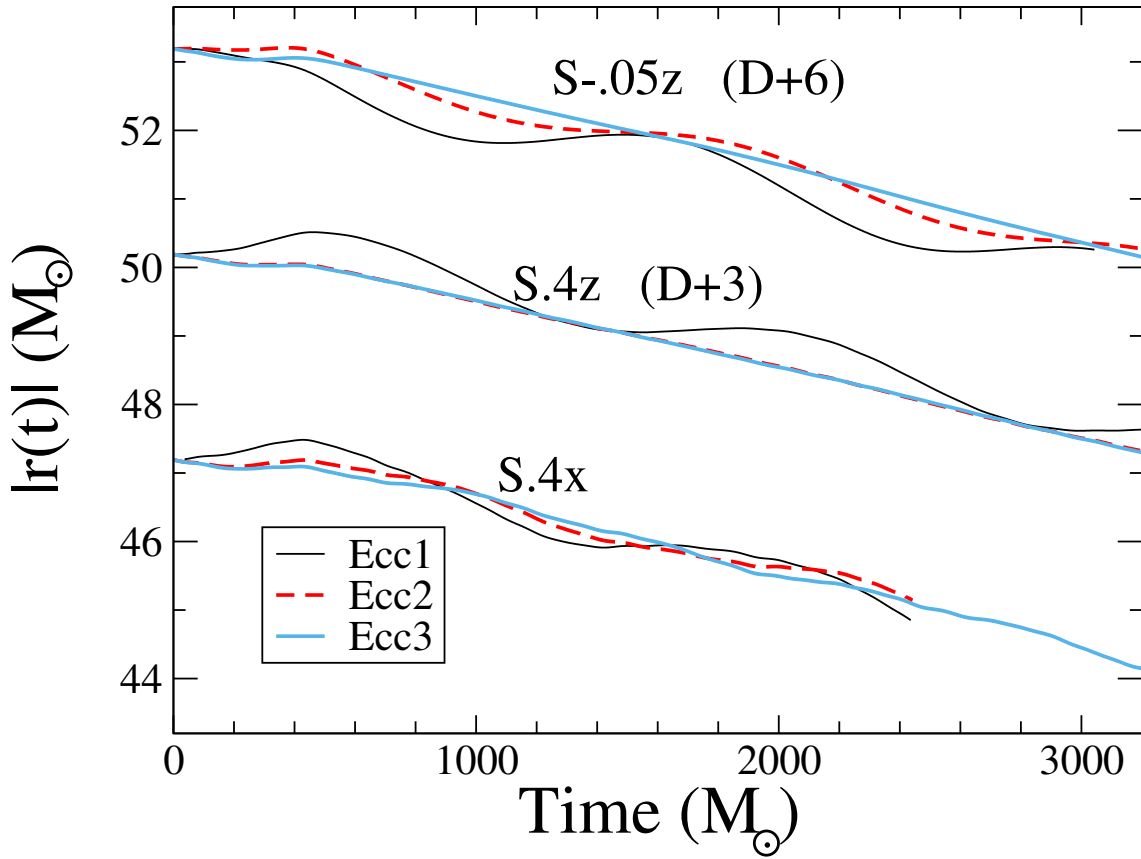
Figure 2.10: The binary separation as a function of time. Shown are three eccentricity removal iterations (Ecc1,Ecc2,Ecc3) for each of the three configurations studied. The data for `S-.05z` and `S.4z` is offset vertically by 6 and 3, respectively, for clarity of plotting.
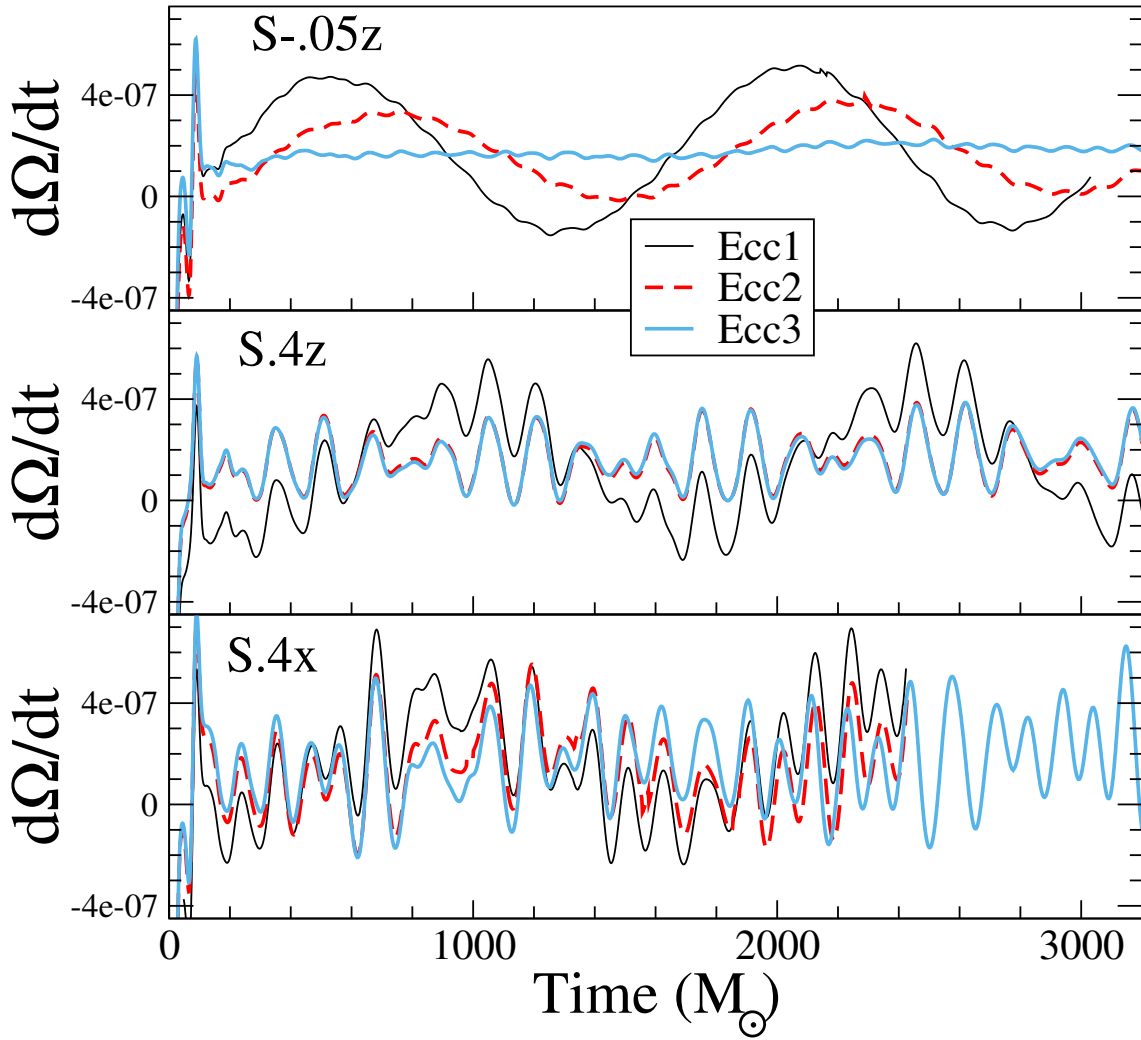
Figure 2.11: The derivative of the binary orbital frequency as a function of time for different levels of eccentriccity reduction for our three runs of interest. Note that $d\Omega/dt$ has units of $M_\odot^{-2}$.

Name	$\Omega \times 10^3$	$\dot{a}_0 \times 10^5$	e
S.4z - Ecc1	5.10538	0	0.006
S.4z - Ecc2	5.09591	-1.60	$\lesssim 0.001$
S.4z - Ecc3	5.09594	-1.75	$\lesssim 0.001$
S-.05z - Ecc1	5.10538	0	0.008
S-.05z - Ecc2	5.11561	0	0.004
S-.05z - Ecc3	5.11769	-1.71	0.0006
S.4x - Ecc1	5.10538	0	0.007
S.4x - Ecc2	5.10429	-2.27	0.004
S.4x - Ecc3	5.10064	-2.36	$\lesssim 0.002$

Table 2.3: Eccentricity removal for the three main runs discussed in this paper. Only initial orbital frequency Ω_0 and initial radial expansion factor $\dot{a}_0$ are changed between different EccN iterations. Recall that these quantities have units of $M_\odot^{-1}$.

condition in Eq. 2.38. Evolutions with these choices are labeled with the suffix "Ecc1", and show noticable variations in the separation between the two NS, cf. the solid black lines in Fig. 2.10.

We compute the trajectories of the centers of mass of each star, as determined by Eq. 2.65, $\vec{c}_1(t)$ and $\vec{c}_2(t)$, and using the relative separation $\vec{r} = \vec{c}_2(t) - \vec{c}_1(t)$, compute the orbital frequency

$$\Omega(t) = \frac{|\vec{r}(t) \times \dot{\vec{r}}(t)|}{r(t)^2}, \tag{2.68}$$

where an over-dot indicates a numerical time-derivative. Finally, we compute $\dot{\Omega}(t)$ and fit it to a function of the form

$$\dot{\Omega}(t) = A_1(t_c - t)^{-11/8} + A_2(t_c - t)^{-13/8}$$
$$+ B_0 \cos\left(B_1 t + B_2 t^2 + B_3\right). \tag{2.69}$$

The power law parts of this fit represent the orbital decay due to the emission of gravita-

tional waves, while the oscillatory part represents the eccentric part of the orbit. We then update Ω_0 and $\dot{a}_0$ with the formulae (see Buonanno et al. (2011) for a detailed overview)

$$\Omega_0 \leftarrow \Omega_0 - \frac{B_0 B_1}{4\Omega_0^2} \sin B_3, \tag{2.70}$$

$$\dot{a}_0 \leftarrow \dot{a}_0 + \frac{B_0}{2\Omega_0} \cos B_3. \tag{2.71}$$

We repeat this procedure twice, resulting in simulations with suffix Ecc2 and Ecc3. Table 2.3 summarizes the orbital parameters for the individual simulations, and Figs. 2.10 and 2.11 illustrate the efficacy of the procedure through plots of separation and time-derivative of orbital frequency. The eccentricity is successfully reducued from $e \sim 1\%$ to $\sim 0.1\%$. After two eccentricity reduction iterations, variations in $\dot{\Omega}(t)$ are so small that they are no longer discernible from higher-frequency oscillations in $\dot{\Omega}(t)$, cf. Fig. 2.11.

The high freuqency oscillations in $\dot{\Omega}(t)$ are caused by the quasi-normal ringing of the neutron stars, as discussed in detail below in Sec. 2.5.5. Here, we only note that these oscillations are convergently resolved, cf. Fig. 2.12, and are therefore a genuine feature of our initial data. Figure 2.12 also confirms that the lowest resolution $(k = 0)$ gives adequate resolution for eccentricity removal.

The eccentricity removal algorithm attempts to isolate variations on the orbital time-scale as the signature of eccentricity. For S.4z - Ecc2, it reports $e = 0.0005$ and for S.4z - Ecc3, $e = 0.0002$. However, given the large amplitude of the QN mode ringing, we consider these estimates unreliable, and therefore quote an upper bound of 0.001 in Table 2.3. Similarly, for S.4x - Ecc3, the fitting reports $e = 0.001$, and we quote a conservative upper bound of 0.002.

2.5.3   Aligned spin BNS evolutions: NS Spin

In this section, we will discuss the measurement of spins during our evolutions for the non-precessing cases, S.4z and S-.05z. Aligned spin binaries do not precess. Combined with the low viscosity we expect the NS spins to stay approximately constant during the
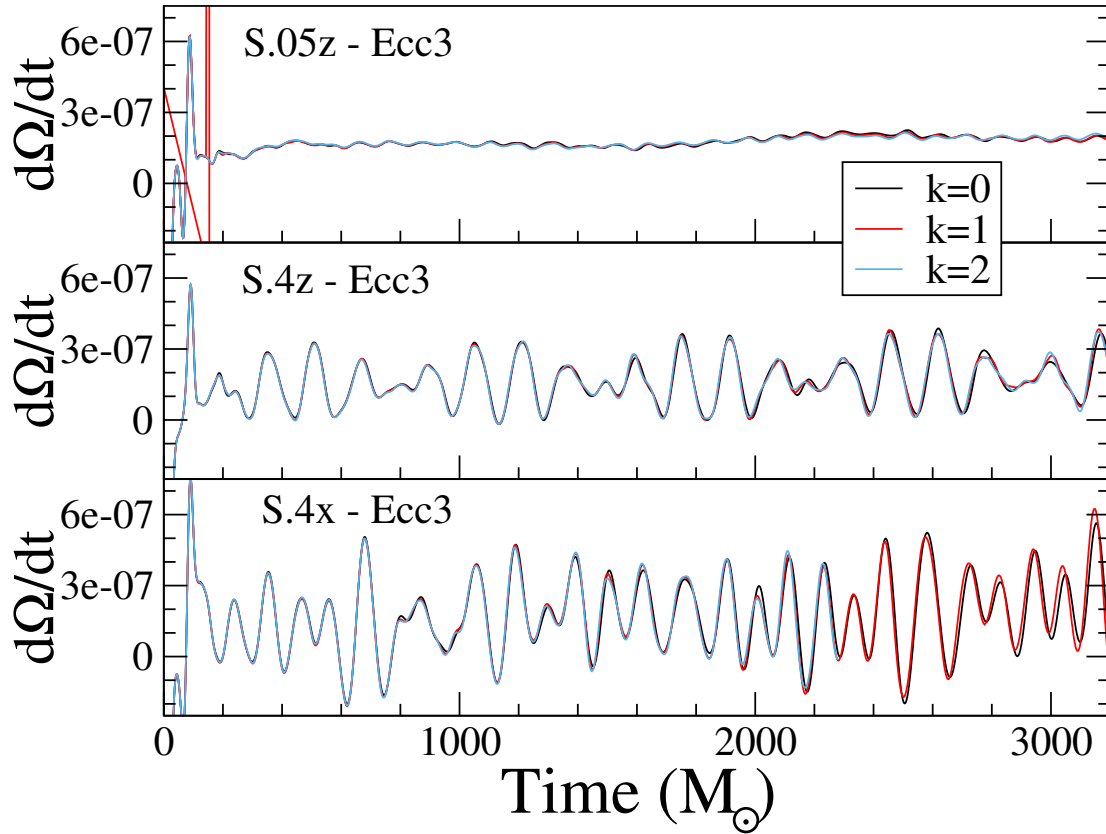
Figure 2.12: Convergence of $\dot{\Omega}(t)$. Shown are $\dot{\Omega}(t)$ at three different numerical resolutions ($k = 0, 1, 2$) for the final, lowest-eccentricity initial data. The oscillations in $\dot{\Omega}(t)$ are evidently not caused by numerical truncation error. Note that $\dot{\Omega}$ has units of $M_\odot^{-2}$.
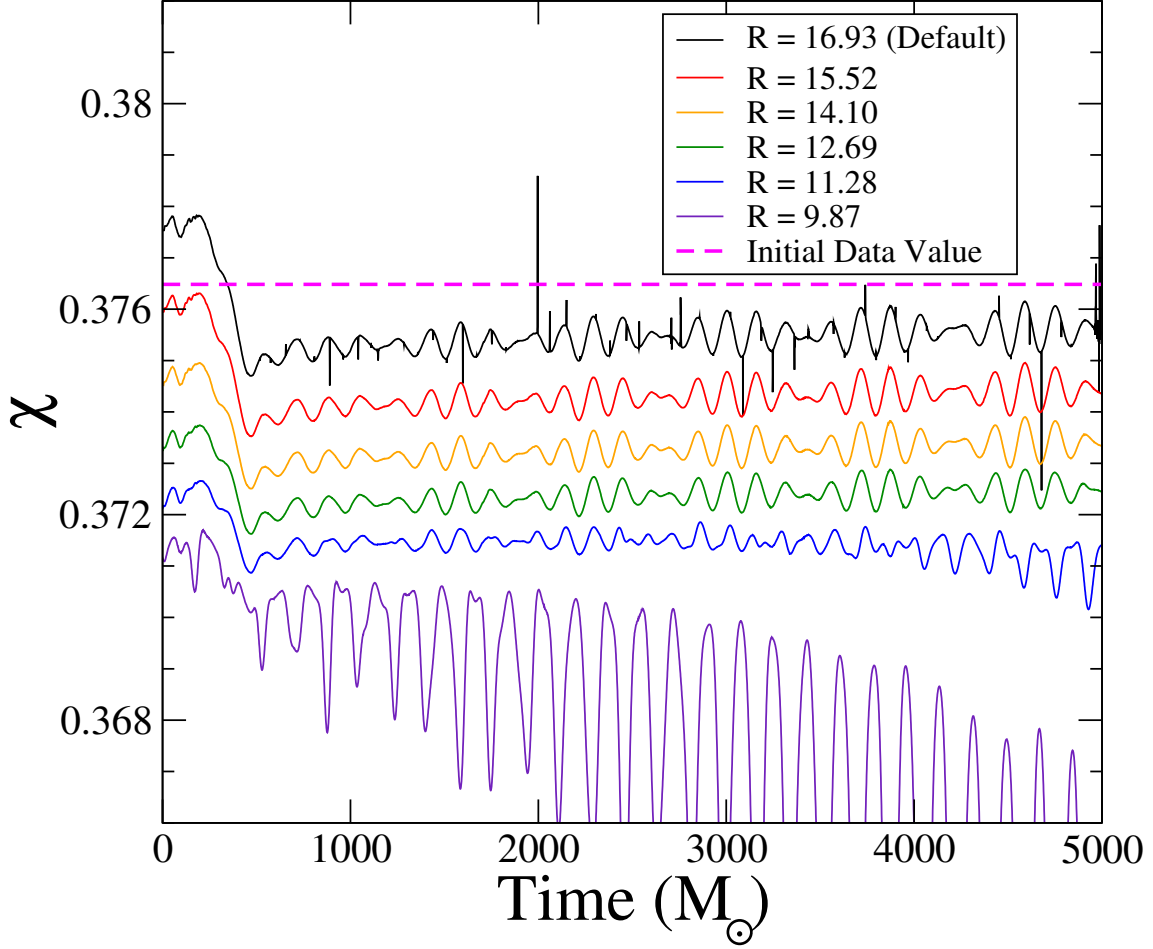
Figure 2.13: The spin measured on multiple coordinate spheres for the `S.4z` run.

evolutions. These systems therefore serve as a test on our spin diagnostics during the evolutions. In this section, and through the rest of this paper, we always use the final eccentricity reduction, "Ecc3". For brevity, we will omit the suffix "-Ecc3", and refer to the runs simply as `S-.05z`, etc.

We do not track the surface of the star during the evolution. Instead we simply evaluate the quasi-local spin of the stars on coordinate spheres in the frame comoving with the binary. We must therefore verify that the spin measured is largely independent of the radius of the sphere, and that it is maintained during the evolutions at the value consistent with that in the initial data. Figure 2.9 established that coordinate spheres can be used to extract the quasi-local spin in the initial data. Figure 2.13 shows the

results for the high-spin simulation `S.4x` during the inspiral.

For coordinate spheres with radii $R = 11.28M_\odot$ to $R = 16.93M_\odot$ in grid coordinates, the spins remain roughly constant in time. The different extraction spheres yield spins that agree to about 1%, with a consistent trend that larger extraction spheres result in slightly larger spins (as already observed in the initial data). The horizontal dashed line in Fig. 2.13 indicates the spin measured on the stellar surface (i.e. not on a coordinate sphere) in the initial data. We thus find very good agreement between all spin measurements, and conclude that the quasi-local spin is reliable to about 1%.

The extraction sphere $R = 9.87M_\odot$ in Fig. 2.13 intersects the outer layers of the neutron star. Because the quasi-local spin captures only the angular momentum within the extraction sphere, the value measured on $R = 9.87M_\odot$ falls as our comoving grid-coordinates cause this coordinate sphere to slowly move deeper into the interior of the star. This behavior, again, is consistent with Fig. 2.9.

These tests of using multiple coordinate spheres were only run for about half of the inspiral – enough to establish that the method is robust. Subsequently, we report spins measured on the largest coordinate sphere, $R = 16.93M_\odot$.

The full behavior of the spin during the inspiral is shown in figure 2.14 for both the `S.4z` and `S-.05z` runs. Comparing the spin at different resolutions, we note that the data for $k = 1$ and $k = 2$ are much closer to each other than compared to $k = 0$, indicating numerical convergence. We note that the impact of numerical resolution (as shown in Fig. 2.14) is small compared to the uncertainty inherent from the choice of extraction sphere, cf. Fig. 2.13. We also note that for the first $10000M_\odot$ of the run, the measured spin behaves as a constant, as expected, albeit with some small oscillations. However, afterward, we notice the absolute value of the spin starts to decrease in both cases. Finally, we note that in both cases, the spin measured in the inital data on the stellar surface is within $\Delta\chi = 0.008$ of the spin measured during the evolution.
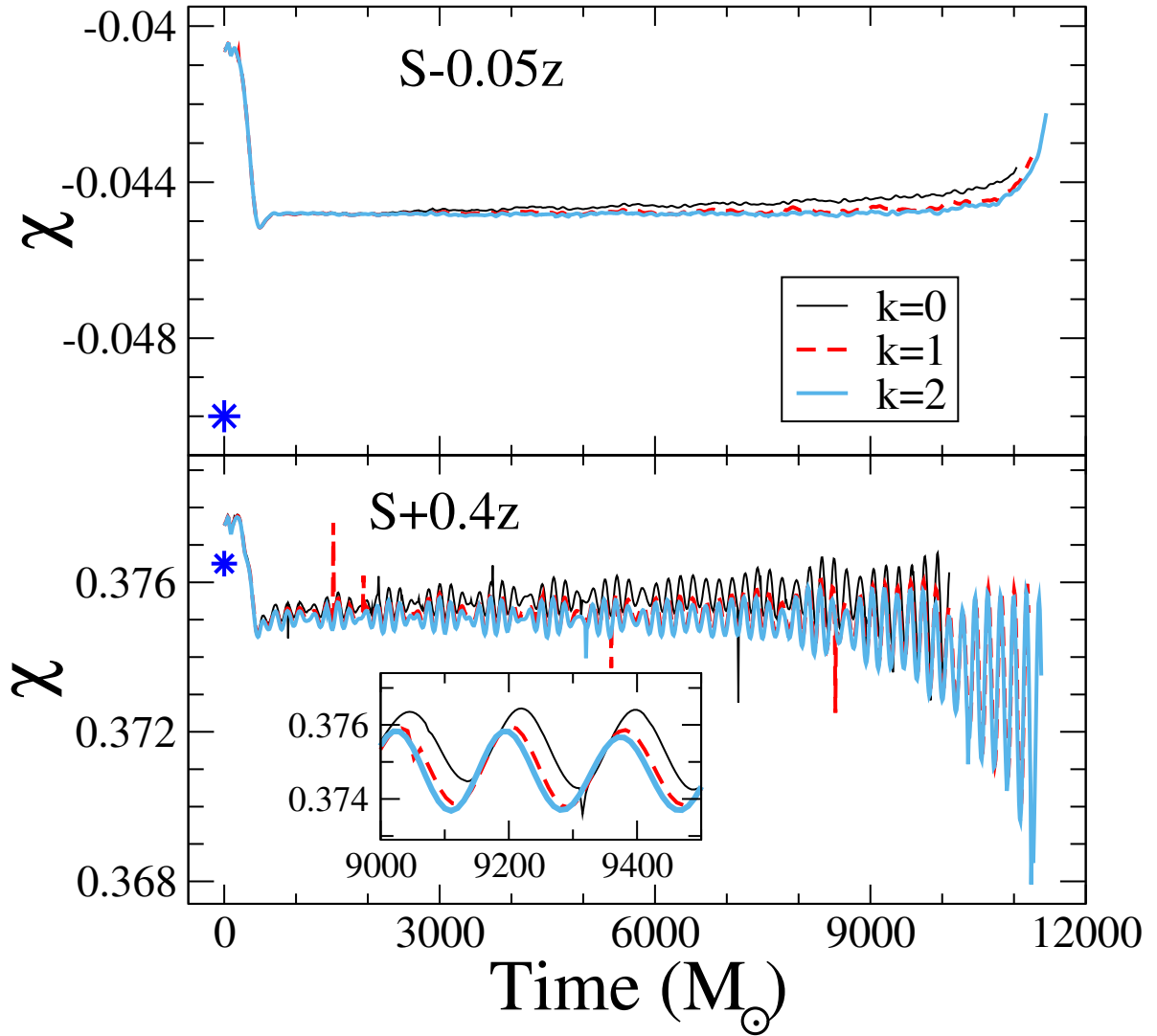
Figure 2.14: Neutron star spin during the two aligned-spin evolutions. Shown are three different numerical resolutions, $k = 0$ (lowest), $k = 1$, and $k = 2$ (highest). The asterisk indicates the spin measured on the stellar surface in the initial data.
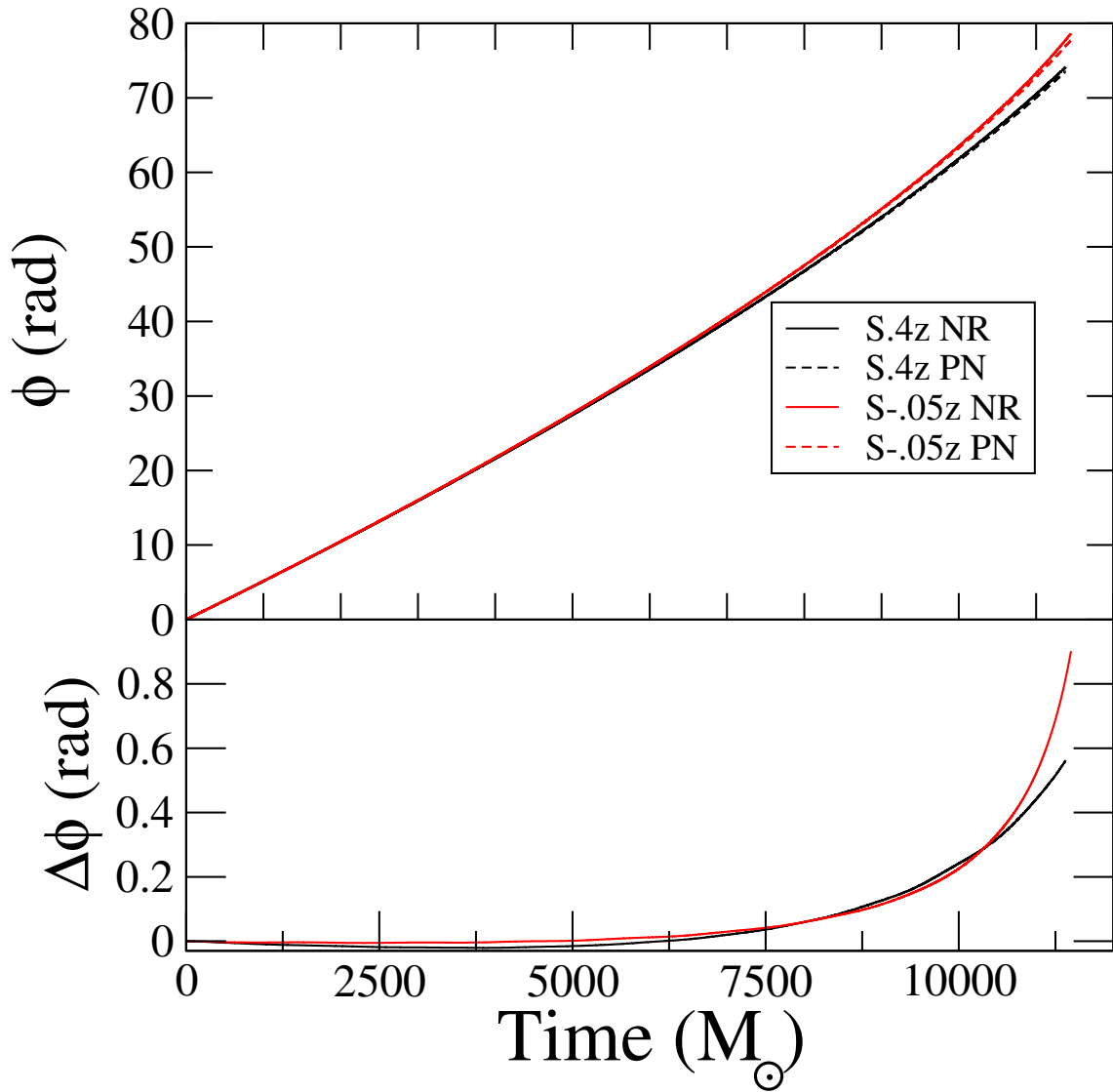
Figure 2.15: Accumulated orbital phase as a function of time for our anti-aligned, `S-.05z`, and aligned, `S.4z`, runs. The dashed lines are Taylor T4 PN simulations. The PN simulations were matched to NR in the intervals [1109,3956] and [2090,4904] respectively. Qualitatively, there is excellent agreement with the numerical data. The lower panel shows the difference $\Delta\phi(t) = \phi_{\mathrm{NR}}(t) - \phi_{\mathrm{PN}}(t)$.

Finally, we compute the orbital phase

$$\phi(t) = \int_0^t \Omega(t') \, dt', \tag{2.72}$$

where the orbital frequency $\Omega(t)$ is given by Eq. (2.68). The result is plotted in Fig. 2.15, along with the

Post-Newtonian prediction for the same binary parameters (spins, masses and initial orbital frequencies). We use the Taylor T4 model (see e.g.,Boyle et al. (2007)) at 3.5PN order expansion, with no tidal terms added, using the matching techniques described in Ossokine et al. (2015). We find excellent qualitative agreement in both cases, thereby giving additional evidence that our numerical simulations are working as expected. We do find large late time growth in the phase difference, however this is expected because we do not model tidal effects, which become increasingly important at late times, in our Post-Newtonian equations.

Figure 2.16 shows the gravitational waveforms for our two non-precessing simulations. We extract the waves on a sphere of radius $R = 627 M_\odot$.

2.5.4 Precession

We now turn to the precessing simulation, S.4x. Figure 2.17 shows the components of the spin-vector $\vec{\chi}$ of one of the neutron stars, as a function of time. The quasi-local spin diagnostic returns a spin with nearly constant magnitude, varying only by ± 0.002 around its average value 0.370. The spin components clearly precess, with the dominant motion in the xy-plane (the initial orbital plane), with the simulation completing about 2/3 of a precession cycle. A z-component of the NS spin also appears, indicating precession of the neutron star spin out of the initial orbital plane.

Fig. 2.17 shows a comparison of spin precession between numerical relativity and Post-Newtonain theory. We perform this comparison using the matching tecnhique in Ossokine et al. (2015). This gives very good agreement between PN (dotted) and NR
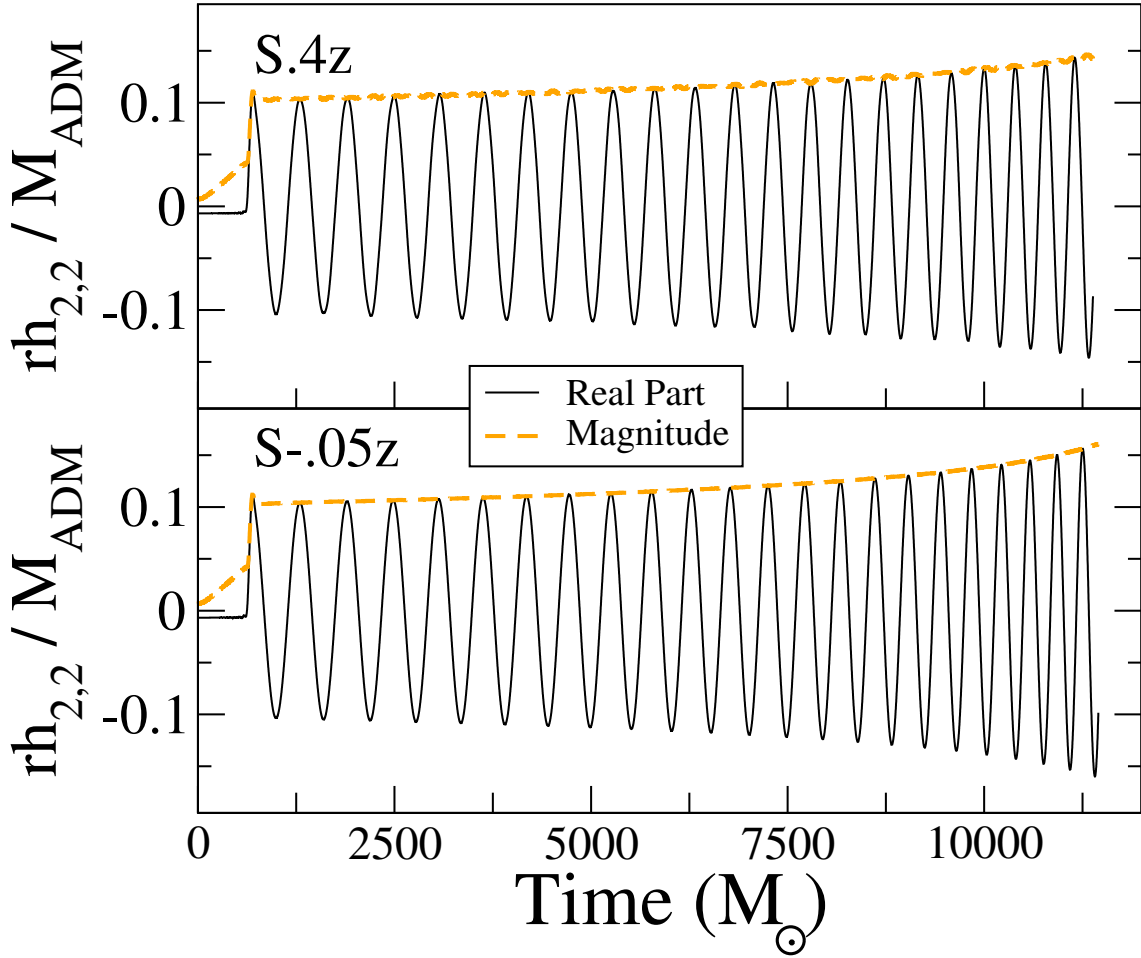
Figure 2.16: The gravitational waveforms for our anti-aligned, `S-.05z`, and aligned, `S.4z` runs. The black curve represents the real part of the waveform, $\Re(h_{2,2})$ while the orange curve represents the magnitude of the waveform.
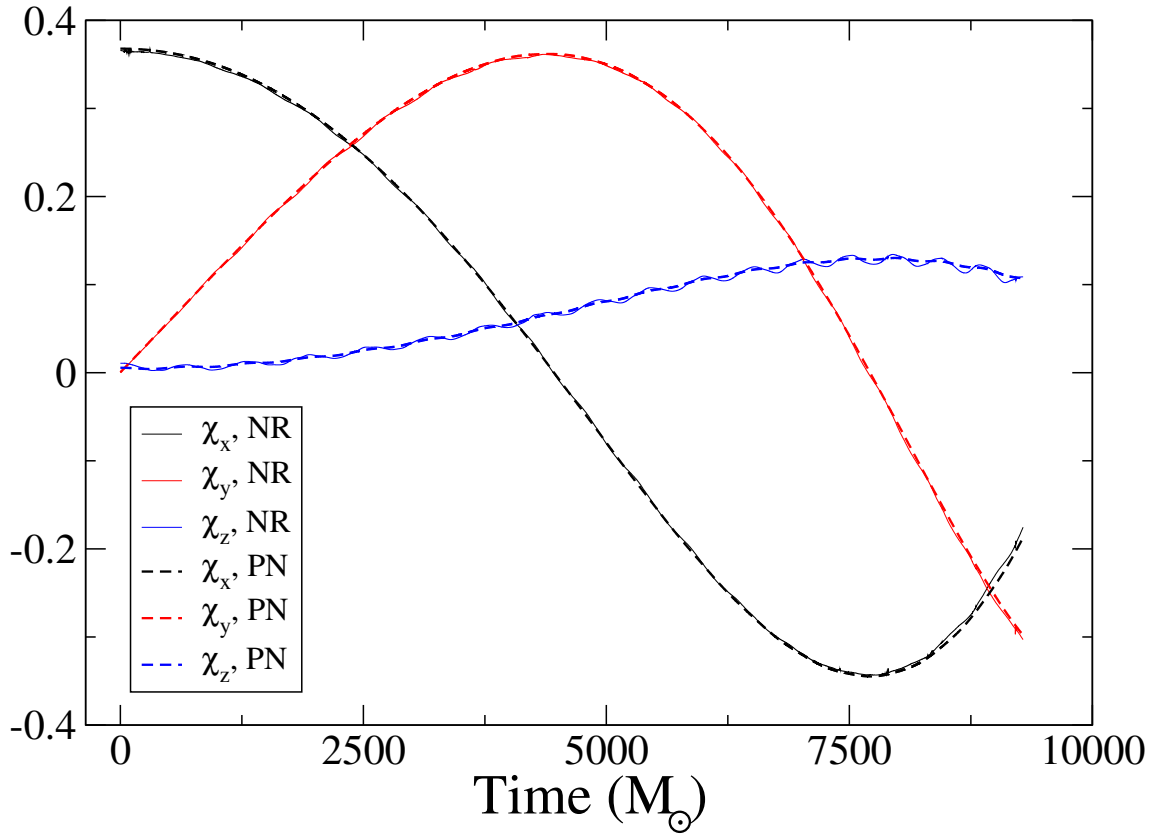
Figure 2.17: Spin-components of one of the neutron stars during the precessing simulation (thick, solid lines). The dotted and dashed lines represent the unmatched and matched PN results respectively. The agreement between PN and NR is good for both PN simulations. The orbital frequency was evolved using the Taylor T4 approximant. The matching was done in the interval [1892,4575].
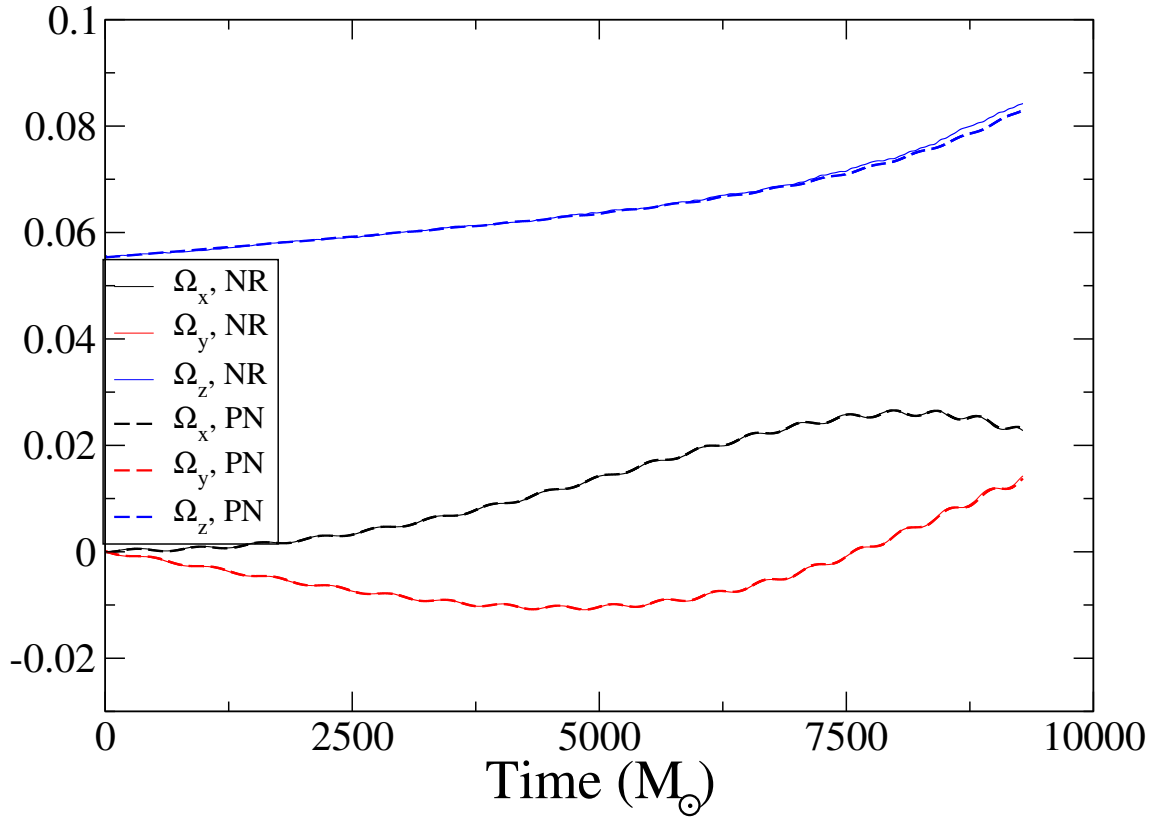
Figure 2.18: Components of the orbital frequency vector $\vec{\Omega}$. Thick solid lines represent the precessing BNS simulation and thin dashed lines represent the matched post-Newtonian simulations. The inclination reaches $\delta = 0.34$rad at $t = 7600 M_{\odot}$.
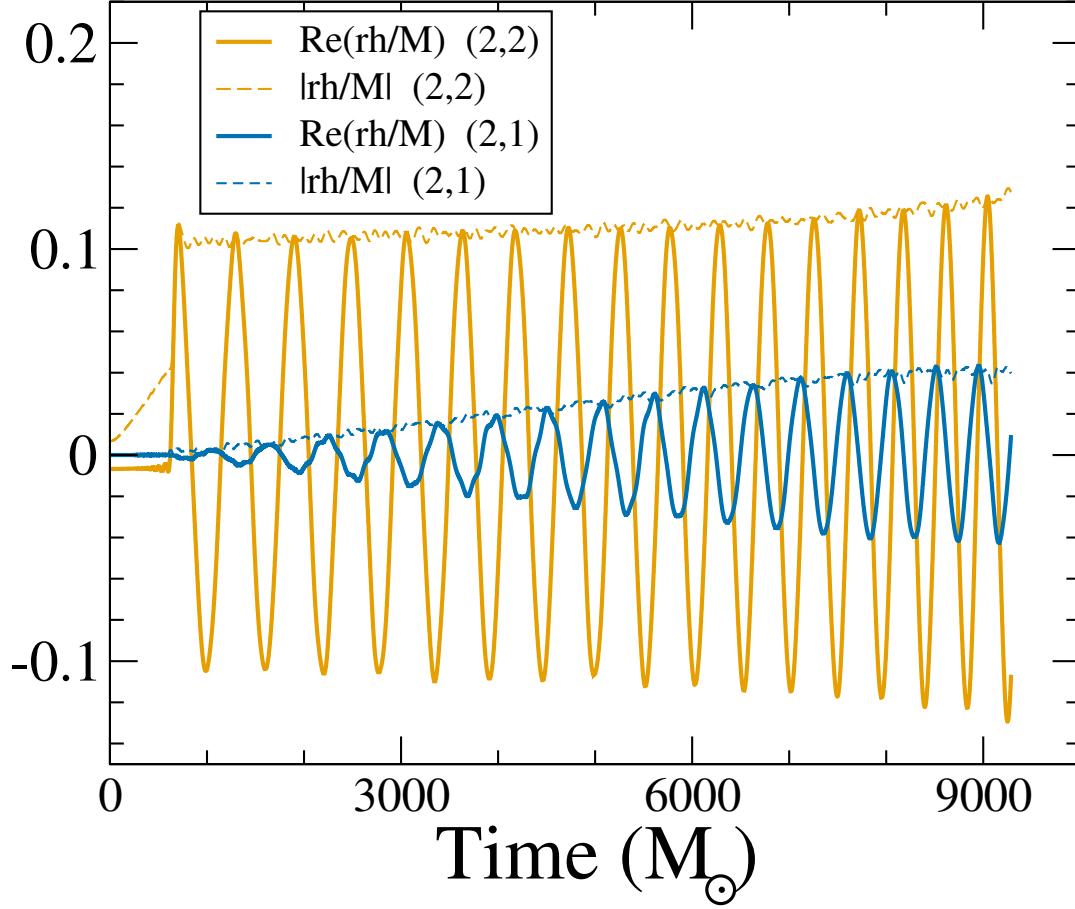
Figure 2.19: Gravitational waveforms of our precessing run. Shown are the $(l, m) = (2, 2)$ and $(2, 1)$ modes, as extracted in a spherical harmonic decomposition aligned with the z-axis. The emergence of the (2,1) mode indicates precession of the orbital plane away from the xy-plane.

(solid) as shown by Fig. 2.17. The NS spins indeed precess as expected, thus confirming both the quality of quasi-local spin measures, as well as the performance of the PN equations. Note that z-component of the spin in the NR data undergoes oscillations that are unmodelled by PN. These occur on a timescale of half the orbital timescale. Similar effects were found in Ossokine et al. (2015). The origin of these oscillations remains unclear. The precession of the orbital angular frequency is shown in Fig. 2.18. We find substantial precession away from the initial direction of the orbital frequency $\vec{\Omega}_0 \propto \hat{z}$, with the angle δ between $\vec{\Omega}(t)$ and the z-axis reaching $20°$. Once again, the PN equations reproduce the precession features successfully.

Finally, Fig. 2.19 shows the (2,2) and the (2,1) spherical harmonic modes of the gravitational wave-strain extracted at an extraction surface of radius $R = 647 M_\odot$. The (l,m)=(2,1) mode would be identically zero for an equal-mass aligned spin binary with orbital frequency parallel to the z-axis, so the emergence of this mode once again indicates precession in this binary.

2.5.5 Stellar Oscillations

The rotating neutron stars constructed here show oscillations in the central density, as plotted in Fig. 2.20. In the low spin run, the density oscillations have a peak-to-peak amplitude of about 0.6%, whereas in the high-spin runs (S.4z and S.4x), the density oscillations reach a peak-to-peak amplitude of 20%. The two high-spin simulations show oscillations of nearly the same amplitude and frequency, therefore oscillating nearly in phase throughout the entire inspiral. The oscillation-period is about $177 M_\odot \sim 0.87$ms, i.e. giving a frequency of 1.15kHz. It remains constant throughout the inspiral. The low-spin run S-0.5z exhibits a slightly smaller oscillation period of about $P \approx 170 M_\odot \approx$ 0.84ms, i.e. a frequency of ≈ 1.19kHz.

To investigate the spectrum of the density oscillations, we perform a Fourier-transform on $\rho(t)$. The result is shown in Fig. 2.21. The Fourier-transform confirms the dominant frequencies just stated, and reveals several more frequency components ranging up to 4kHz. The high spin evolutions S.4z and S.4x exhibit identical freqencies for all five discernible peaks. In contrast, the low-spin evolution S-.05z shows different frequencies.

We interpret these features as a collection of excited quasi-normal modes in each neutron star. The modes are excited because the initial data is not precisely in equilibrium. For the two high-spin cases the neutron stars have similar spin, and therefore the same quasi-normal modes, whereas in the low-spin model, the quasi-normal mode frequencies differ due to the different magnitude of the spin.

To strengthen our interpretation, we consider the series of rotating, relativistic, $\Gamma = 2$

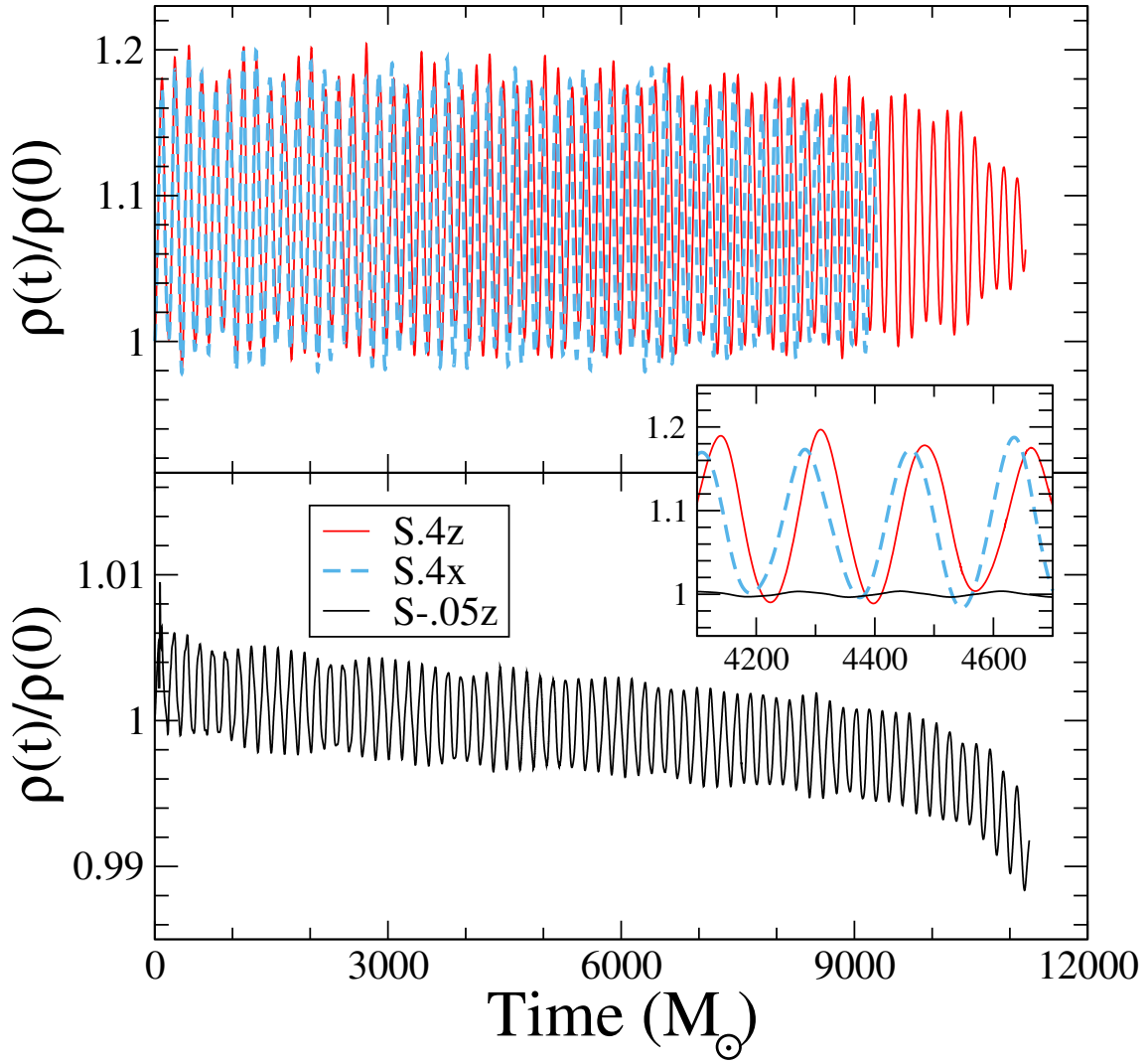Figure 2.20: The maximum density $\rho(t)$ in each of our runs, normalized by the initial maximum density $\rho(0)$. The inset shows an enlargement of all three runs, illustrating that the oscillations are more pronounced in the high-spin simulations.
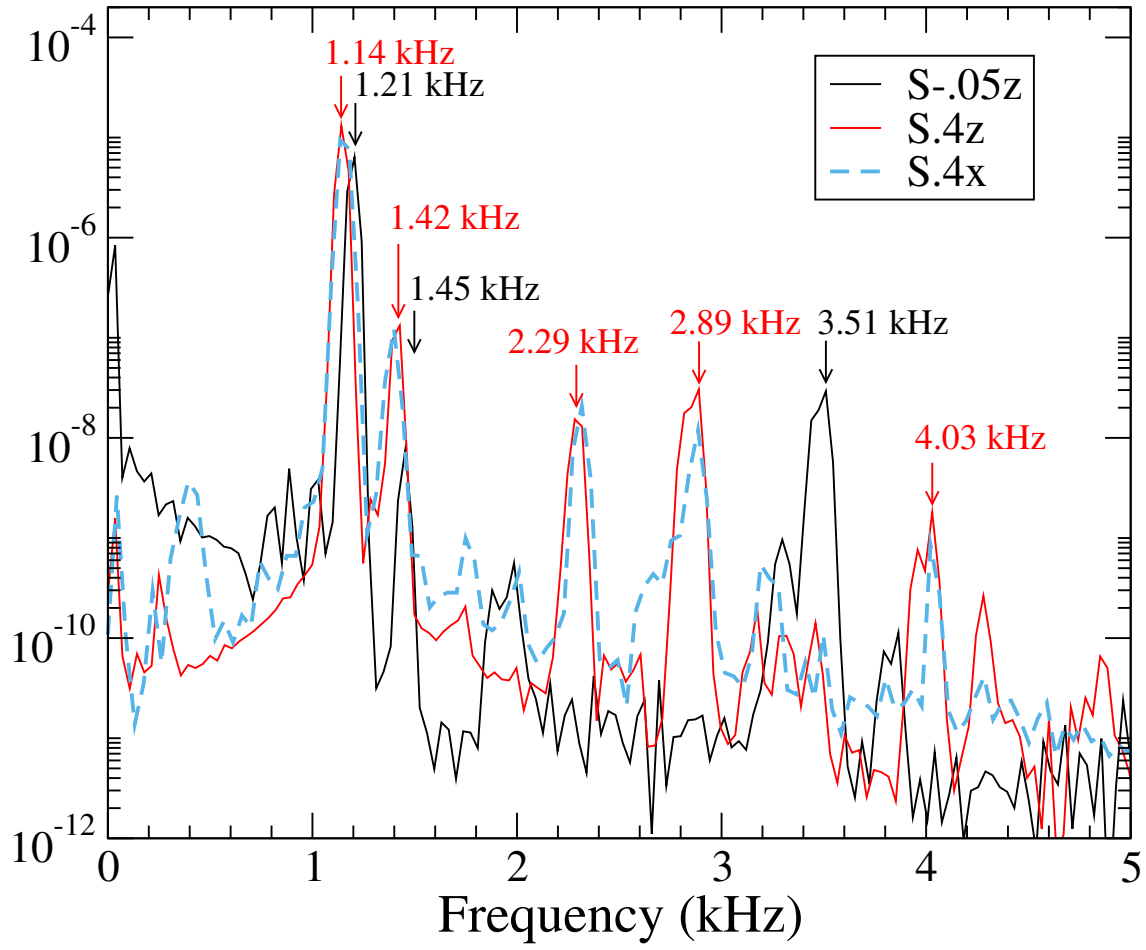
Figure 2.21: The Fourier transforms of the central density in all three of our runs. Labelled are the peak frequencies for the quasi-radial F mode and the $l = 2$, ^2f mode.

polytropes computed by Dimmelmeier et al Dimmelmeier et al. (2006).

Ref. Dimmelmeier et al. (2006)'s model "AU3" has a central density of $1.074 \times 10^{-3} M_\odot^{-2}$ and its rotation is quantified through the ratio of polar to equatorial radius, $r_p/r_e = 0.780$. Meanwhile, our high-spin runs have a central density of $1.02 \times 10^{-3} M_\odot^{-2}$ (measured as time-average of the data shown in Fig. 2.20) and from our initial data, we find $r_p/r_e \sim 0.8$. Given the similarity in these values, we expect Ref. Dimmelmeier et al. (2006)'s "AU3" to approximate our high-spin stars S.4x, S.4z. Ref. Dimmelmeier et al. (2006) reports a frequency of $f_F = 1.283$kHz for the spherically symmetric ($\ell = 0$) F-mode, and a frequency $f_{2f} = 1.537$kHz for the axisymmetric $\ell = 2$ mode ^2f. These frequencies compare favorably with the two dominant frequencies in Fig. 2.21, 1.14kHz and 1.42kHz.

Presumably, the small differences in these frequencies can be accounted for by the slight differences in stellar mass, radius, and rotation. Moreover, tidal interactions and orbital motion could factor in, as well. In our figure 2.21 we also see several other peaks at higher frequencies, which are reminiscent of the overtones and mode couplings in figure 10 of Dimmelmeier et al. (2006). If we identify our peak at $f_{H1} = 4.03$kHz with the H_1 mode, then (in analogy to Dimmelmeier et al. (2006) Fig. 10), $f_{H1} - f_F = (4.03 - 1.14)$kHz $= 2.89$kHz, and $2f_F = 2.28$kHz, two frequencies that are indeed present in our simulations. Although we find clear indications of axisymmetric $\ell = 2$-modes, we note that their power is smaller by two orders of magnitude, compared to the spherically symmetric, dominant F mode.

Turning to the low-spin run S.05z, we note that if, to first order, these frequencies scale like $f \sim \sqrt{\rho}$ (on dimensional grounds), then we expect to see $F = 1.22$kHz and $^2f = 1.49$kHz. This is very close to what is seen.

The density oscillations discussed in this section are reflected in analogous oscillations in various other diagnostic quantities, for instance, the orbital frequency, Fig. 2.12 and the quasi-local spin as shown in Fig. 2.14. The dominant frequencies 1.14kHz and 1.42kHz can be robustly identified throughout our data analysis. In figure 2.22 we plot the
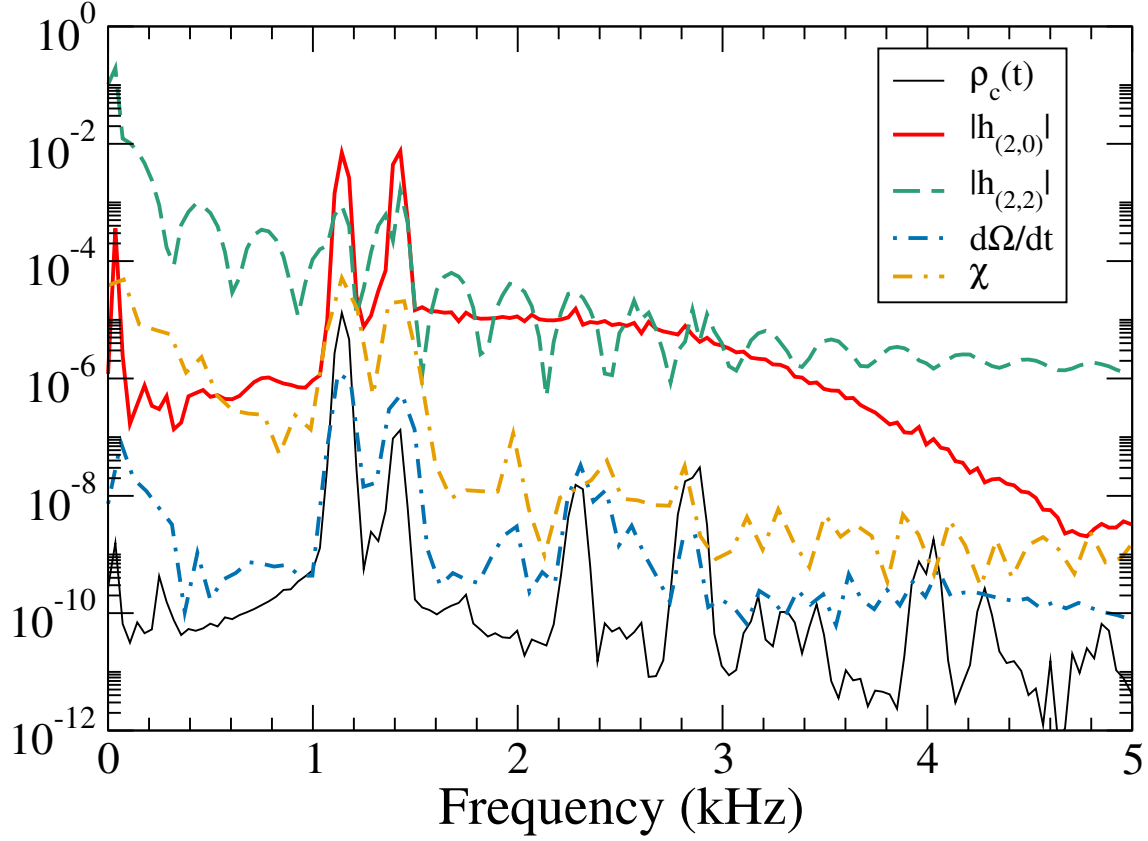
Figure 2.22: Fourier transforms of the central density $\rho_c(t)$, two modes of the magnitude of gravitational wave strain ($|h_{2,2}|$ and $|h_{2,0}|$), $\dot{\Omega}$ and χ for the S.4z run. All quantities show excess power at 1.14kHz and 1.4kHz, corresponding to the frequencies of excited neutron star quasi-normal modes.

Fourier transform of the density, the $(2,0)$ and $(2,2)$ gravitational wave strains, the orbital angular velocity time derivative $d\Omega/dt$ and the measured spin χ for the S.4z run. All show peaks in power at these two frequencies, $F \sim 1.14$kHz and $^2f \sim 1.4$kHz. Gold et. al. Gold et al. (2012), in the simulation of close encounters in eccentric, irrotational, NSNS binaries, where the modes are physical and much stronger than the quasi-circular case, find an excited f-mode frequency of 1.586 kHz.

We believe that the stellar modes are excited because the initial data are not in perfect equilibrium. We expect the quasi-equilibrium approximations that enter the initial data formalism to become less valid at higher spins, consistent with our observation that

the high spin models exhibit stronger oscillations. This interpretation is strengthened by additional simulations of neutron stars at larger separation. Increasing the intial separation by a factor 1.5, while keeping the same rotation parameter ω as in the `S.4z`-case, we find quasi-normal oscillations of similar amplitude than in `S.4z`. If the oscillations were caused by the neglect of tidal deformation, we would expect the amplitude to drop with the 3rd power of separation, inconsistent with our results.

Finally, we point out that the radial rotation profile, cf. Eq. (2.48) influences the amplitude of the induced quasi-normal oscillations. If the initial data is constructed with the rotation profile Eq. (2.49), instead of equation 2.48, then the amplitude of the density oscillations for high spin doubles. This further supports our conjecture that the origin of this mode comes from non-equilibrium initial data.

2.6   Discussion

In this paper we implement Tichy's method Tichy (2012) to construct binary neutron star initial data with arbitrary rotation rates. We demonstrate that our implementation is exponentially convergent, as expected for the employed spectral methods.

We measure the spin of the resulting neutron stars using the quasi-local angular momentum formalism Brown & York (1993); Cook & Whiting (2007); Lovelace et al. (2008); Owen (2007). The resulting angular momentum is found to be nearly independent on the precise choice of extraction sphere, cf. Fig. 2.9, and provides a means to define the quasi-local angular momentum of each neutron star to about 1%, both in the initial data and during the evolution, cf. Fig. 2.13. We are able to construct binary neutron star initial data with dimensionless angular momentum of each star as large as $\chi = S/M^2 \sim$ 0.43, both for the case of aligned spins, and also for a precessing binary where the initial neutron star spins are tangential to the initial orbital plane.

For irrotational BNS initial data sets, we find a quasi-local angular momentum of $\chi \sim 2 \times 10^{-4}$, cf. Fig. 4.2. This spin is small enough that present waveform modeling

studies for BNS (e.g. Bernuzzi et al. (2015); Baiotti et al. (2011); Baiotti et al. (2010)) are not yet limited by residual spin.

When evolving the initial data sets, the dimensionless spin measured in the initial data drops by about 0.004, and then remains constant through the 10 inspiral orbits for which we evolved the neutron star binaries. During these evolutions, we also demonstrated iterative eccentricity removal: By analyzing the orbital frequency $\Omega(t)$ during the first few orbits, we can correct the initial data parameters Ω_0 and $\dot{a}_0$, and thus decrease the orbital eccentricity from $e \approx 0.01$ to $e \lesssim 0.001$.

For the precessing simulation `S.4x`, we find precession of the neutron star spin directions. The numerically established precession of the spin axes and of the orbital angular momentum agrees well with post-Newtonian predictions.

The rotating neutron stars constructed here exhibit clear signals of exciting quasi-normal modes. We are able to identify multiple modes in the Fourier spectrum of the central density. The amplitude of the excited quasi-normal modes increases steeply with rotation rate of the neutron stars. For `S-.05z` (spin magnitude $\chi = 0.045$) the density oscillations have peak-to-peak amplitude of 0.6%, raising to 20% for the two runs with high spins (`S.4x` and `S.4z`).

2.7 Summary

Write a summary.

Chapter 3

Gravitational and Electromagnetic Radiation from Spinning Magnetized Binary Neutron Stars

3.1 Chapter Overview

Below is a bullet list of things to include in this chapter.

- Motivations - what are the luminosities we expect. Pulsar, single magnetized star, double magnetized stars.

- Initial data we constructed. What parameters and why. Convergence thereof.

- Results?

3.2 Introduction

My Introduction

3.3 Initial Data

3.4 Summary

My Summary.

Chapter 4

Spinning Neutron Stars in Mixed Binaries

4.1 Chapter Overview

An Overview of my chapter here.

4.2 Chapter TDL

- Previous work on mixed binaries with spinning stars?

- Plot of omega vs chi for NS spin

- 3d parameter space plot

- Information about how easy/difficult it is to do the solution? Number of gridpoints, constraints, its?

- Geoffrey massive disk formation

4.3 Papers to read

Insert here

4.4 Introduction

Black hole - neutron stars (Bh-ns) inspirals and mergers are an important potential source of gravitaitonal waves for ground-based detectors like Advanced LIGO and Virgo. Information abou tthe inspiral can help determine the neutron star equation of state. Electromagnetic signals from the merger can give clues about the violent physical processes that occur. Gravitaitonal waves help test general relativity in the genuinely non-linear regime.

The parameter space of Bh-ns binaries is quite rich. The mass ratio, q, and black hole spin, $\vec{\chi}$, have been of particular interest in numerical simulations. Foucart cite gave an analytic description of how this combination can predict the time of neutron star disruption. The neutron star equation of state is also of great interest. The size of the star is directly lninked ot when tidla disruption occurs. One aspect that has not been studied, however, is the effect of neutron star spin. All simulations to date use irrotational neutron star in their Bh-NS binaries. Since no Bh-NS binaries have been directly observed, the NS spins are, at least observationally, unconstrained. Spinning NS will affect the gravitational waveforms and cause the inspiral to proceed more slowly (for spin-aligned NS). cite XX found that NS spins of XX in Bh-ns binaries could cause Advanced LIGO to miss XX percent of potential signals. The spin could also affect the time of NS disruption, as the stellar material will be less tightly bound to the stellar surface.

Recently, Tacik et al. (2015) used the `SpEC` code to create and evolve initial data sets of binary neutron star systems with arbitrary spins. In this chapter, we extend this code to create initial data for Bh-ns systems where the NS spin is arbitrary. The structure

of this chapter is as follows: In section XX, we review the formalism developed in Tichy (2011) to create binaries with spinning NS, and discuss how this is extended to Bh-NS systems. In section XX we present data demonstrating the robustness and convergence of this initial data. Finally, we conclude the chapter in section XX.

4.5 Initial Data Formalism

In this section we will discuss the formalism used to solve the Einstein field equations and create quasi-equilibrium initial data for black-hole - neutron star (BHNS) binaries with spinning neutron stars. We begin with the $3 + 1$ decomposition of the space-time metric tensor,

$$g_{\mu}\nu dx^{\mu}dx^{\nu} = -\alpha^2 dt^2 + \gamma_{ij}\left(dx^i + \beta^i dt\right)\left(dx^j + \beta^j dt\right),\tag{4.1}$$

where α is the lapse function, $beta^i$ is the shift vector, and γ_{ij} is the induced metric on a spatial hypersurface $\Sigma(t)$. The normal vector n^{μ} to $\Sigma(t)$ is related to the coordinate time t by

$$t^{\mu} = \alpha n^{\mu} + \beta^{\mu}.\tag{4.2}$$

The extrinsic curvature of $\Sigma(t)$ is given by

$$K_{\mu\nu} = -\frac{1}{2}\mathcal{L}_n\gamma_{\mu\nu}\tag{4.3}$$

where $\gamma_{\mu\nu} = g_{\mu\nu} + n_{\mu}n_{\nu}$. We restrict our attention to the spatial part K^{ij} of the extrinsic curvature, since $n_{\mu}K^{\mu\nu} = 0$ by construction. It is convenient to decmopose it into its trace and trace-free parts,

$$K^{ij} = A^{ij} + \frac{1}{3}K\gamma_{ij}.\tag{4.4}$$

The matter in the system is modelled with the stress-energy tensor of a perfect fluid

$$T_{\mu\nu} = \left(\rho + P\right)u_{\mu}u_{\nu} + Pg_{\mu\nu}\tag{4.5}$$

where ρ is the fluid's energy density, P is its pressure, and u^μ is its four-velocity. It is further useful to define the projections of the matter quantities

$$E \;=\; T^{\mu\nu}n_\mu n_\nu, \tag{4.6}$$

$$S \;=\; \gamma^{ij}\gamma_{i\mu}\gamma_{j\nu}T^{\mu\nu}, \tag{4.7}$$

$$J^i \;=\; -\gamma^i_\nu T^{\nu\tau} n_\tau. \tag{4.8}$$

The spatial metric is decomposed with the conformal transformation

$$\gamma_{ij} = \Psi^4 \tilde\gamma_{ij} \tag{4.9}$$

where Ψ is called the conformal factor, and $\tilde\gamma_{ij}$ is the conformal metric. The other quantities in the initial value problem use the following conformal transformations:

$$E \;=\; \Psi^{-6}\tilde E, \tag{4.10}$$

$$S \;=\; \Psi^{-6}\tilde S, \tag{4.11}$$

$$J^i \;=\; \Psi^{-6}\tilde J^i, \tag{4.12}$$

$$A^{ij} \;=\; \Psi^{-10}\tilde A^{ij} \tag{4.13}$$

$$\alpha \;=\; \Psi^6 \tilde\alpha \tag{4.14}$$

$\tilde A^{ij}$ is related to the shift and to the time derivative of the conformal metric, $\tilde u_{ij} = \partial_t \tilde\gamma_{ij}$, by

$$\tilde A^{ij} = \frac{1}{2\tilde\alpha}\left[\left(\tilde{\mathrm L}\beta\right)^{ij} - \tilde u^{ij}\right], \tag{4.15}$$

where $\tilde L$ is the conformal longitudinal operator,

$$\left(\tilde L V\right)^{ij} = \tilde\nabla^i V^j + \tilde\nabla^j V^i - \frac{2}{3}\tilde\gamma^{ij}\tilde\nabla_k V^k. \tag{4.16}$$

We solve the extended thing sandwich (XCTS), which are a set of 5 coupled non-linear equations.

$$2\tilde\alpha\left[\tilde\nabla_j\left(\frac{1}{2\tilde\alpha}\left(\tilde L\beta\right)^{ij}\right) - \tilde\nabla_j\left(\frac{1}{2\tilde\alpha}\tilde u^{ij}\right)\right.$$
$$\left. -\frac{2}{3}\Psi^6\tilde\nabla^i K - 8\pi\Psi^4\tilde J^i\right] \;=\; 0, \tag{4.17}$$

$$\tilde{\nabla}^2\Psi - \frac{1}{8}\Psi\tilde{R} - \frac{1}{12}\Psi^5 K^2$$
$$+\frac{1}{8}\Psi^{-7}\tilde{A}_{ij}\tilde{A}^{ij} + 2\pi\Psi^{-1}\tilde{E} \;=\; 0, \tag{4.18}$$

$$\tilde{\nabla}^2\left(\tilde{\alpha}\Psi^7\right) - \left(\tilde{\alpha}\Psi^7\right)\left[\frac{1}{8}\tilde{R} + \frac{5}{12}\Psi^4 K^2 + \frac{7}{8}\Psi^{-8}\tilde{A}_{ij}\tilde{A}^{ij}\right.$$
$$\left.+2\pi\Psi^{-2}\left(\tilde{E} + 2\tilde{S}\right)\right] = -\Psi^5\left(\partial_t K - \beta^k\partial_k K\right). \tag{4.19}$$

These are solved for Ψ, the densitized lapse, $\alpha\Psi$, and the shift.

The matter content of $\Sigma(t)$ is determined by $\tilde{E}$, $\tilde{S}$, and $\tilde{J}^i$. The free data are γ_{ij}, $\tilde{u}_{ij}$, K and $\partial_t K$. $\tilde{u}_{ij} = 0$ and $\partial_t K = 0$ are natural choices in a coordinate system corotating with the binary. We use the choice of maximal slicing, $K = 0$. The choice of the conformal metric will be later discussed in section XX.

Let us now further discuss the matter content of the neutron star. The energy density of the fluid is $\rho = \rho_0\left(1 + \epsilon\right)$, where ρ_0 is the baryon density and ϵ is the internal energy. The specific enthalpy of the fluid is

$$h = 1 + \epsilon + \frac{P}{\rho_0}. \tag{4.20}$$

It is convenient to introduce the following projection of the four velocity:

$$\gamma \;=\; \gamma_n\gamma_0\left(1 - \gamma_{ij}U^iU_0^j\right) \tag{4.21}$$

$$\gamma_0 \;=\; \left(1 - \gamma_{ij}U_0^iU_0^j\right)^{-1/2} \tag{4.22}$$

$$\gamma_n \;=\; \left(1 - \gamma_{ij}U^iU^j\right)^{-1/2} \tag{4.23}$$

$$U_0^i \;=\; \frac{\beta^i}{\alpha} \tag{4.24}$$

$$u^\mu \;=\; \gamma_n\left(n^u + U^\mu\right) \tag{4.25}$$

$$U^\mu n_\mu \;=\; 0 \tag{4.26}$$

Following Tichy (2011), the three-velocity is written as the sum of an irrotational part (the gradient of a potential ϕ) and a rotational part W:

$$U^i = \frac{\Psi^{-4}\tilde{\gamma}^{ij}}{h\gamma_n}\left(\partial_j\phi + W_j\right).$$ (4.27)

W is a freely chosen vector in this formalism; we will discuss this choice in section XX.

The matter fluid must satisfy the continuity equation and the Euler equation. The continuity equation is a second order elliptic equation for the potential ϕ:

$$\frac{\rho_0}{h}\nabla^\mu\nabla_\mu\phi + \left(\nabla^\mu\phi\right)\nabla_\mu\frac{\rho_0}{h} = 0.$$ (4.28)

Under the assumptions made in Tichy (2011), this equation can be written as

$$\begin{aligned}
\rho_0\Bigg\{&-\tilde{\gamma}^{ij}\partial_i\left(\partial_j\phi + W_j\right) + \frac{h\beta^i\Psi^4}{\alpha}\partial_i\gamma_n + hK\gamma_n\Psi^4 \\
&+ \left[\tilde{\gamma}^{ij}\tilde{\Gamma}^k_{ij} + \gamma^{ik}\partial_i\left(\ln\frac{h}{\alpha\Psi^2}\right)\right]\left(\partial_k\phi + W_k\right)\Bigg\} \\
&= \tilde{\gamma}^{ij}\left(\partial_i\phi + W_i\right)\partial_j\rho_0 - \frac{h\gamma_n\beta^i\Psi^4}{\alpha}\partial_i\rho_0.
\end{aligned}$$ (4.29)

The Euler equation is solved for the specific enthalpy h. The solution is, as shown in Tichy cite:

$$h = \sqrt{L^2 - \left(\nabla_i\phi + W_i\right)\left(\nabla^i\phi + W^i\right)},$$ (4.30)

where

$$L^2 = \frac{b + \sqrt{b^2 - 4\alpha^4\left(\left(\nabla_i\phi + W_i\right)W^i\right)^2}}{2\alpha^2},$$ (4.31)

and

$$b = \left(\beta^i\nabla_i\phi + C\right)^2 + 2\alpha^2\left(\nabla_i\phi + w_i\right)w^i.$$ (4.32)

The boundary condition at the surface of the neutron star can deduced from the $\rho_0 \to 0$ limit of the continuity equation:

$$\tilde{\gamma}^{ij}\left(\partial_i\phi + W_i\right)\partial_j\rho_0 = \frac{h\gamma_n\beta^i\Psi^4}{\alpha}\partial_i\rho_0.$$ (4.33)

The boundary condition at infinity (which is in practice, in our computational grid, at $R = 10^{10}$) are the requirement of a Minkowski metric in the intertial frame:

$$\beta^i = 0, \tag{4.34}$$

$$\alpha\Psi = 1, \tag{4.35}$$

$$\Psi = 1. \tag{4.36}$$

The interior of the black hole is excised from the computation domain. The boundary conditions at the surface of the black hole horizon are cite

$$\tilde{s}^k\nabla_k \log\Psi = -\frac{1}{4}\left(\tilde{h}^{ij}\tilde{\nabla}^i\tilde{s}_j - \Psi^2 J\right) \tag{4.37}$$

$$\beta_\perp = \alpha \tag{4.38}$$

$$\beta_\parallel = \Omega_j^{BH} x_k \epsilon^{ijk} \tag{4.39}$$

whre s is the outward pointing unit normal to the apparent horizon surface, $\mathrm{A}h^{ij}$ is the 2-metric on the surface, J is a projection fo the excision surface clarify this, and Ω^{BH} is a free parameter that determines the spin of the black hole.

The force balance equation at the centre of the NS is

$$\nabla \log h = 0. \tag{4.40}$$

We can re-write this equaiton as

$$\nabla \ln\left(\alpha^2 - \gamma_{ij}\beta^i\beta^j\right) = -2\nabla\ln\Gamma, \tag{4.41}$$

where

$$\Gamma = \frac{\gamma_n\left(1 - \left(\beta^i + \frac{W^i\alpha}{h\gamma_n}\right)\frac{\nabla_i\phi}{\alpha h\gamma_n} - \frac{W_iW^i}{\alpha^2\gamma_n^2}\right)}{\sqrt{1 - \left(\frac{\beta^i}{\alpha} + \frac{W^i}{h\gamma_n}\right)\left(\frac{\beta_i}{\alpha} + \frac{W_i}{h\gamma_n}\right)}}. \tag{4.42}$$

, which is a second order equation for the orbital frequency Ω. If desired, this equation can be solved to find a best guess for the orbital frequency. Alternatively, eccentricity removal techniques, such as those used in Tacik et al. (2015) can be used to find the best value of the orbital frequency.

W is chosen as as to give the NS a uniform rotational profile. Following our work in Tacik et al. (2015), we use

$$W^i = \epsilon^{ijk}\omega^j r^k, \tag{4.43}$$

where $\epsilon^{ijk} = \{\pm 1, 0\}$, r^k is the position vector relative to the centre of the star, and ω^j is a freely chosen constant vector.

The angular momentum of the black hole is computed as

$$S = \frac{1}{8\pi} \oint_{\mathcal{H}} \phi^i s^j K_{ij} dA \tag{4.44}$$

where $\mathcal{H}$ is the black hole's apparent horizon, s^j is the outward-pointing unit-normal and ϕ^i is an azimuthal vector field. The dimensionless spin is defined as

$$\chi = \frac{S}{M^2} \tag{4.45}$$

where M is the Christodoulou mass

$$M^2 = M_{\text{irr}}^2 + \frac{S^2}{4M_{\text{irr}}^2}. \tag{4.46}$$

The irreducible mass is related to the surface area of the horizon

$$M_{\text{irr}} = \sqrt{A/16\pi}. \tag{4.47}$$

Following the method introduced in Tacik et al. (2015) we also compute the dimensionless spin of the neutron star in the same way, normalizing it by its ADM mass.

4.6 Numerical Methods

Let us now discuss how we solve these ellitpic equations. We use the pseduo-spectral multi-grid elliptic solver developped in Pfeiffer et al. (2003) and enhanced in Foucart et al. (2008) to incorporate matter. The computational domain is divided into a number of subdomains. A small cube is placed at the centre of the NS. Overlapping this cube is a spherical shell whose outer boundary deforms to fit the NS surface. These are surrounded

by an additional spherical shell. The black hole is represented by two concentric spherical shells. Their inner bounday is required to be an apparent horizon. Three rectangular parallelpipeds surround the axis passing through the centres of the BH and the NS - one between them and one on each side of the objects. An additional eight cylindrical shells are placed around the same axis to cover the intermediate field region. The far-field region is covered by a large spherical shell whose outer boundary is placed at $R = 10^{10}$ using an inverse radial mapping. This domain is visualized in Fig. **??**.
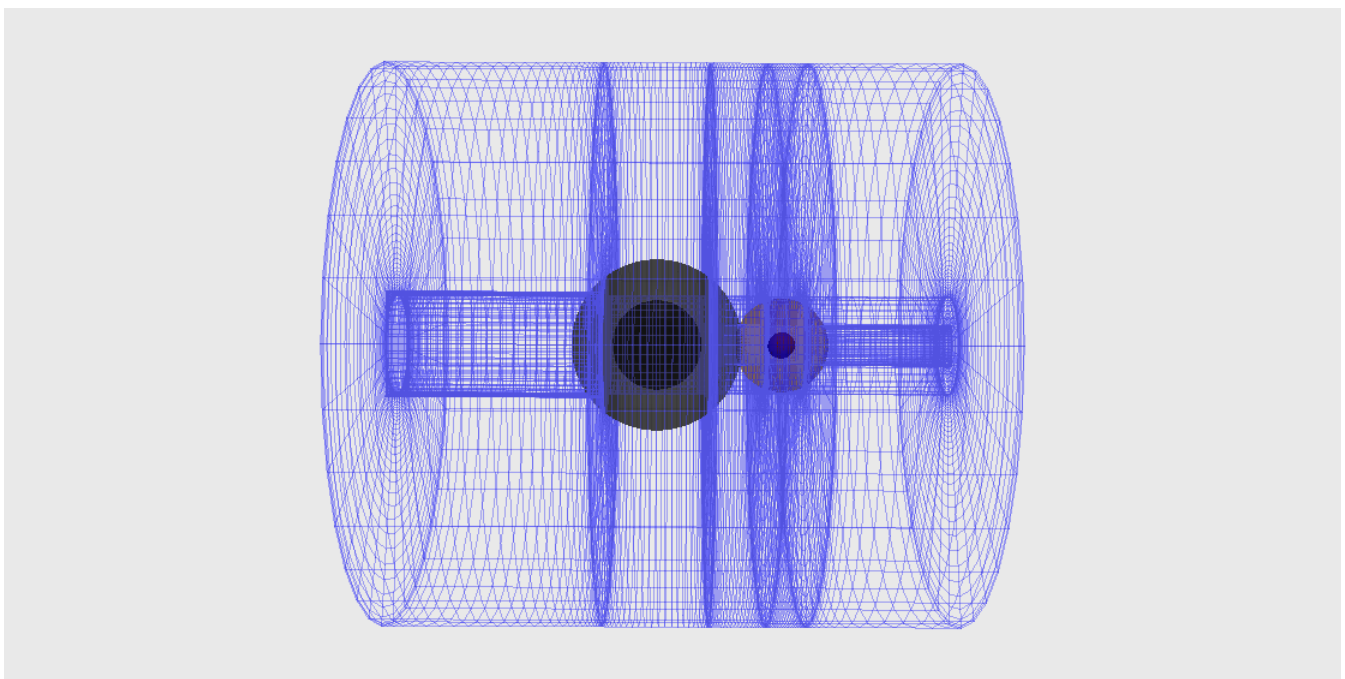
Figure 4.1: Visualization of the Bh-Ns domain decomposition. The black object on the left is the black hole and the orange object on the right is the neutron star. The blue wireframes represent the various cylinders and rectangular parallelpipeds in the domain.

All variables (metric and hydrodynamical) decomposed on sets of basis functions on each subdomain. Finite difference schemes are needed for hydrodynamical quantities during evolutions so as to capture shocks, but for initial data spectral methods are

suitable and exponentical convergence can be guaranteed. The resolution of each domain is synonymous with the number of colocation points used. The resolution of each domain is chosen by hand at the start of the initial data solve, and then modified several times using an adaptive scheme. To discuss the resolution of the computational domain for the purpose of convergence tests, we will use the notation

$$N^{1/3} = \left(\sum N_i \right)^{1/3},\tag{4.48}$$

where we are summing the colocation points of the all the subdomains. A typical initial data solve might start with, using example numbers, $N^{1/3} \sim 33.3$ and end with $N^{1/3} \sim 80.8$

Construction of initial data begins by choosing values for the free parameters in the problem. In particular, these are

- The black hole mass M_{BH}

- The black hole's target dimensionless spin $\vec{\chi_{BH}}$

- The neutron star's baryon mass M_b

- The neutron star's equation of state

- The neutron star's spin vector ω^i

- The separation between the centres of the BH and NS, D

- The orbital angular velocity Ω_0

- The initial infall velocity $\dot{a}$

We will discuss later how we make the choices of Ω_0 and $\dot{a}$. Additionally, one must make a perscription for the free metric variables. We use maximal slicing $K = 0$, and a choice for the conformal metric $\tilde{g}_{ij}$ such that it is Kerr-Schild near the black hole, and flat near the neutron star.

Let's now discuss the algorithm we use the solve for the initial data.

1. If on the first resolution step, set $\omega^i = 0$, otherwise set to the desired value. This has been found to help with convergence. Additionally, impose a maximum radius out to which to apply $W^i = \epsilon^{ijk}\omega^j r^k$, otherwise low density material at high radius can lead to superluminal velocities.

2. Solve the non-linear XCTS equations for the metric variables $X = (\beta^i, \Psi, \alpha\Psi)$ assuming the matter source terms are fixed. Update the metric variables using a relaxation scheme

$$X^{n+1} = \lambda X^* + (1 - \lambda)X^n. \tag{4.49}$$

We use $\lambda = 0.3$.

3. Impose equatorial symmetry. This should only be done if both the NS and the BH have no spin components in the plane. But if it can be imposed, it will speed convergence.

4. Locate the surface of the star. The surface of the star is reprsented in terms of spherical harmonics

$$R(\theta, \phi) = \sum c_{lm} Y^{lm}(\theta, \phi) \tag{4.50}$$

, and for a polytropic equation of state, the surface should satisfy $h(R) = 1$.

5. Compute the ADM linear momentum P_{ADM}, and if necessary move the center of the black hole to zero-out momentum. Add more detail here.

6. If desired, adjust the orbital angular frequency using Eq. 4.41.

7. Get the spin of the BH by evaluating Eq. 4.44. Then modify the parameter Ω in Eq. 4.37 to drive the black hole spin to the target value.

8. Fix the Euler constant by evaluating the integral

$$M_B = \int \rho_0 \Psi^6 \gamma_n dV \tag{4.51}$$

as a function of the Euler constant, and use the secant method to drive the baryon mass to the desired value.

9. Solve the elliptic equations for the velocity potential, ϕ, and update using the same relaxation scheme as described above.

10. Are all equations satisfied to the desired accuracy? If no, go to step two, otherwise proceed.

11. Compute the truncation error for the current solution by examining the spectral coefficients of the metric variables. If the truncation error is too large, adjust the number of grid points and return to step 1.

4.7 Results

4.7.1 Initial Data Set Parameters

Let us begin by discussing the parameters for the initial data sets to be discussed in this work. As a starting point, we use the six BH-NS configurations described in Table 1 of Foucart et al. (2013). All binaries have a mass ratio $q = 7$ and a black hole spin magnitude of $\chi_{\mathrm{BH}} = 0.9$. The neutron star in each binary has an ADM mass of $1.4M_\odot$. In practice, this means that is fixed to have the same baryon mass as that of an isolated, non-spinning neutron star with ADM mass $1.4M_\odot$. There are three different NS equations of state used. They are all polytropic equations of state ($P = \kappa\rho^\Gamma$) with $\Gamma = 2$, but vary in terms of κ, resulting in different neutron star compactnesses. The values of κ used are 84.28, 92.12, 101.45, which result in compactnesses, respectively, of 0.170, 0.156, 0.144, for non-spinning neutron stars with ADM Mass $1.4M_\odot$. We will use the notation $R12$, $R13$ and $R14$ to refer to these configurations, respectively. The $R12$ and $R13$ configurations are only set with the black hole spin aligned with the orbital angular momentum. For $R14$, we also create data sets with the black hole spin misaligned by 20°, 40° and 60°. The

non-parallel part of the black hole spin is set parallel to the $\hat{x}$ axis. In each case the initial separation between the black hole and the neutron star is $D = 7.44M$. The initial infall velocity parameter $\dot{a}$ is set to 0. The orbital angular velocity is the same as in Foucart et al. (2013) and is indicated in table 4.1.

The above constitutes 6 different configurations. For each of these 6 configurations, we choose an additional 6 configurations of neutron star spins (thus 36 total configurations). In particular we choose three directions - aligned with the orbital angular momentum, anti-aligned with the orbital angular momentum, and completley in the orbital plane, parallel to the $\hat{x}$ direction. For each of these 3 directions, we use a "high-spin" and a "low-spin". These are typically $\chi_{NS} \sim 0.4$ and $\chi_{\rm NS} \sim 0.1$, respectively. In our naming notation, we use a large arrow ($\Uparrow$) for the "high-spin" configurations and a small arrow ($\uparrow$) for the "low-spin", with the direction of the arrow indicating the direction of the NS spin vector. The full parameters of the initial data sets are summarized in Table 4.1.

Name	$\Theta_{\rm BH}$	$M_{\rm NS}^b$	$M\Omega_{\rm orbit}$	$\vec{\omega_{\rm NS}}$	$\vec{\chi_{\rm NS}}$
R12i0↑	$0°$	1.5212	0.0413	$0.00667\hat{z}$	$0.0995\hat{z}$
R12i0⇑	$0°$	1.5212	0.0413	$0.0225\hat{z}$	$0.4093\hat{z}$
R12i0↓	$0°$	1.5212	0.0413	$-0.00667\hat{z}$	$-0.0895\hat{z}$
R12i0⇓	$0°$	1.5212	0.0413	$-0.0225\hat{z}$	$-0.4030\hat{z}$
R12i0→	$0°$	1.5212	0.0413	$0.00667\hat{x}$	$0.0936\hat{x}$
R12i0⇒	$0°$	1.5212	0.0413	$0.0225\hat{x}$	$0.3989\hat{x}$
R13i0↑	$0°$	1.5128	0.0413	$0.00555\hat{z}$	$0.0997\hat{z}$
R13i0⇑	$0°$	1.5128	0.0413	$0.019\hat{z}$	$0.3911\hat{z}$
R13i0↓	$0°$	1.5128	0.0413	$-0.00555\hat{z}$	$-0.0845\hat{z}$
R13i0⇓	$0°$	1.5128	0.0413	$-0.019\hat{z}$	$-0.3793\hat{z}$
R13i0→	$0°$	1.5128	0.0413	$0.00555\hat{x}$	$0.0913\hat{x}$
R13i0⇒	$0°$	1.5128	0.0413	$0.019\hat{x}$	$0.3771\hat{x}$
R14i0↑	$0°$	1.5049	0.0413	$0.005541\hat{z}$	$0.1188\hat{z}$

R14i0⇑	0°	1.5049	0.0413	$0.017\hat{z}$	$0.4109\hat{z}$
R14i0↓	0°	1.5049	0.0413	$-0.005541\hat{z}$	$-0.0965\hat{z}$
R14i0⇓	0°	1.5049	0.0413	$-0.017\hat{z}$	$-0.3915\hat{z}$
R14i0→	0°	1.5049	0.0413	$0.005541\hat{x}$	$0.1066\hat{x}$
R14i0⇒	0°	1.5049	0.0413	$0.017\hat{x}$	$0.3907\hat{x}$
R14i20↑	20°	1.5049	0.0412	$0.005541\hat{z}$	$0.1188\hat{z}$ —
R14i20⇑	20°	1.5049	0.0412	$0.017\hat{z}$	$0.4110\hat{z}$
R14i20↓	20°	1.5049	0.0412	$-0.005541\hat{z}$	$-0.0964\hat{z}$
R14i20⇓	20°	1.5049	0.0412	$-0.017\hat{z}$	$-0.3915\hat{z}$
R14i20→	20°	1.5049	0.0412	$0.005541\hat{x}$	$0.1064\hat{x}$
R14i20⇒	20°	1.5049	0.0412	$0.017\hat{x}$	$0.3905\hat{x}$
R14i40↑	40°	1.5049	0.0412	$0.005541\hat{z}$	$0.1193\hat{z}$
R14i40⇑	40°	1.5049	0.0412	$0.017\hat{z}$	$0.4117\hat{z}$
R14i40↓	40°	1.5049	0.0412	$-0.005541\hat{z}$	$-0.0961\hat{z}$
R14i40⇓	40°	1.5049	0.0412	$-0.017\hat{z}$	$-0.3908\hat{z}$
R14i40→	40°	1.5049	0.0412	$0.005541\hat{x}$	$0.1064\hat{x}$
R14i40⇒	40°	1.5049	0.0412	$0.017\hat{x}$	$0.3905\hat{x}$
R14i60↑	60°	1.5049	0.0415	$0.005541\hat{z}$	$0.1200\hat{z}$
R14i60⇑	60°	1.5049	0.0415	$0.017\hat{z}$	$0.4132\hat{z}$
R14i60↓	60°	1.5049	0.0415	$-0.005541\hat{z}$	$-0.0954\hat{z}$
R14i60⇓	60°	1.5049	0.0415	$-0.017\hat{z}$	$-0.3898\hat{z}$
R14i60→	60°	1.5049	0.0415	$0.005541\hat{x}$	$0.1061\hat{x}$
R14i60⇒	60°	1.5049	0.0415	$0.017\hat{x}$	$0.3903\hat{x}$

Table 4.1: table

In addition to these parameters, we consider several other sequences of Bh-Ns data sets to verify the robustness of the solutions across the whole parameter space.

In the runs below we choose the orbital parameters so that

First, we consider a seqeunce where we vary the neutron star spin from $\chi = 0$ to $\chi = 0.7$. Add details

Rough text to add

- The Hamiltonian constraint is computed as

$$H = ||\frac{R_\psi}{8\psi^5}|| \tag{4.52}$$

where R_ψ is the residual of Eq. 4.18 and $||$ represents the $L2$ norm over the computational domain. Similarly, the momentum constraint is computed as

$$M = ||\frac{R_\beta}{2\alpha\Psi^4}|| \tag{4.53}$$

where R_β is the residual of Eq. 4.17.

Second, we consider a sequence where we vary the black hole spin from $\chi = 0$ to $\chi = 0.99$. Add details

Finally, we consider a sequence where we vary the mass ratio from $q = 2$ to $q = 10$. Add details

4.8   Conclusion

Concluding remarks

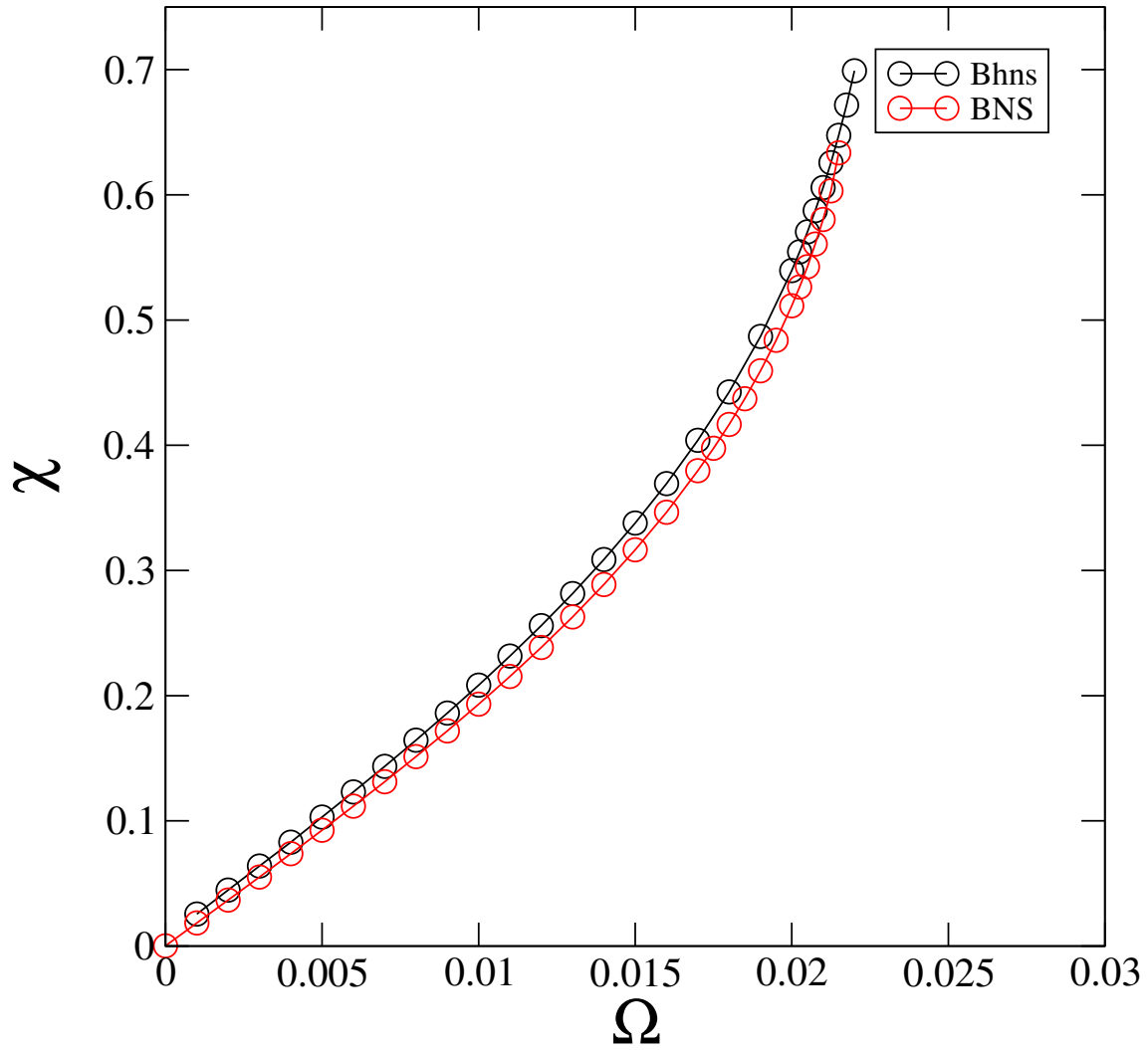Figure 4.2: Neutron star spin χ as a function of neutron star spin parameter ω for a sequence of initial data sets. The black hole spin is constant at $\chi = 0.9$ and the mass ratio is $q = 7$. Add text describing the BNS curve
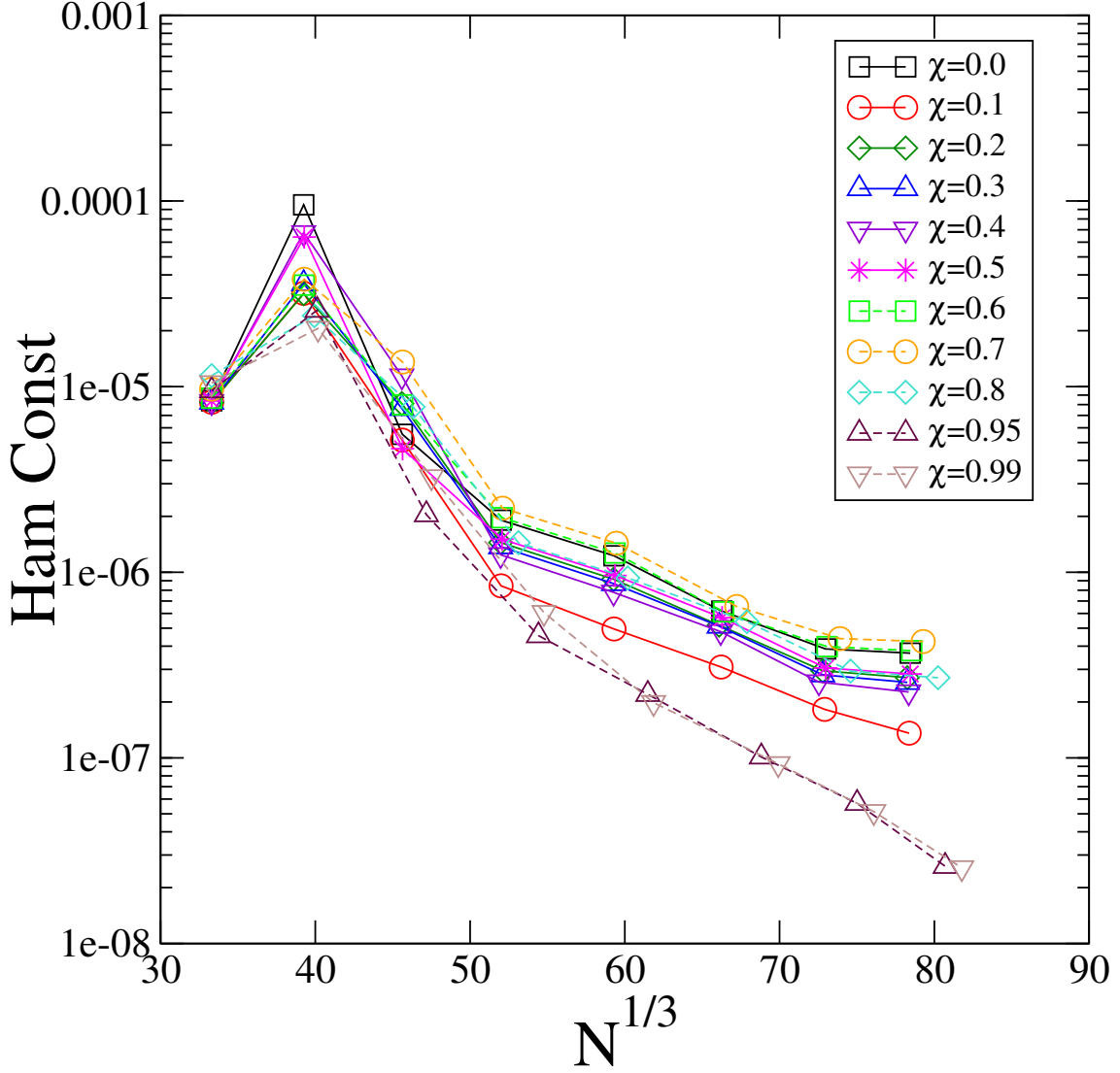
Figure 4.3: Hamiltonian constraint versus resolution for our sequence of binaries where the black-hole spin is varied from $\chi_{BH} = 0$ to $\chi_{BH} = 0.99$. The neutron star spin is constant at $\chi_{NS} \sim 0.4$ and the mass ratio is $q = 7$. We find exponential convergence in all cases.
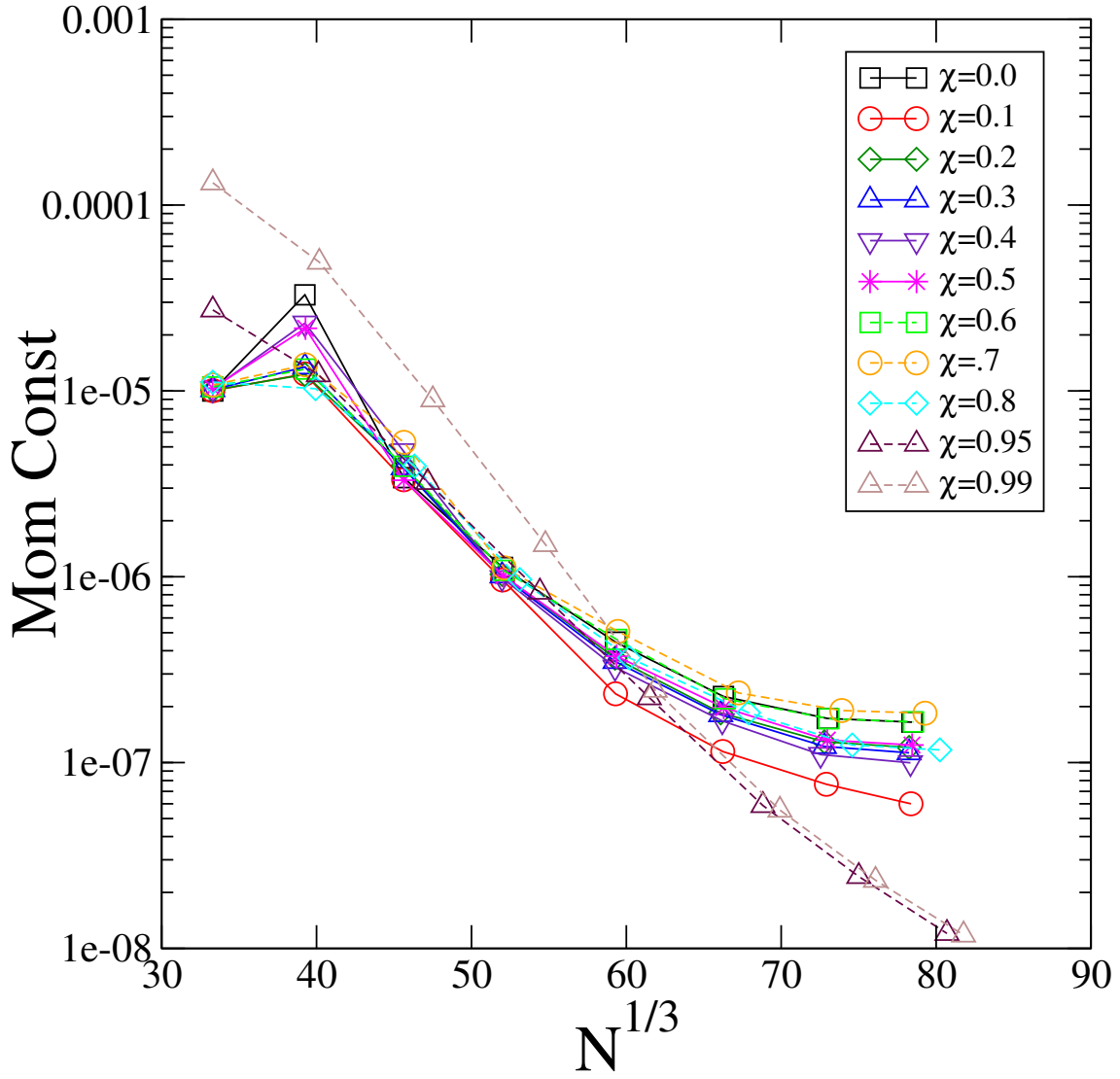
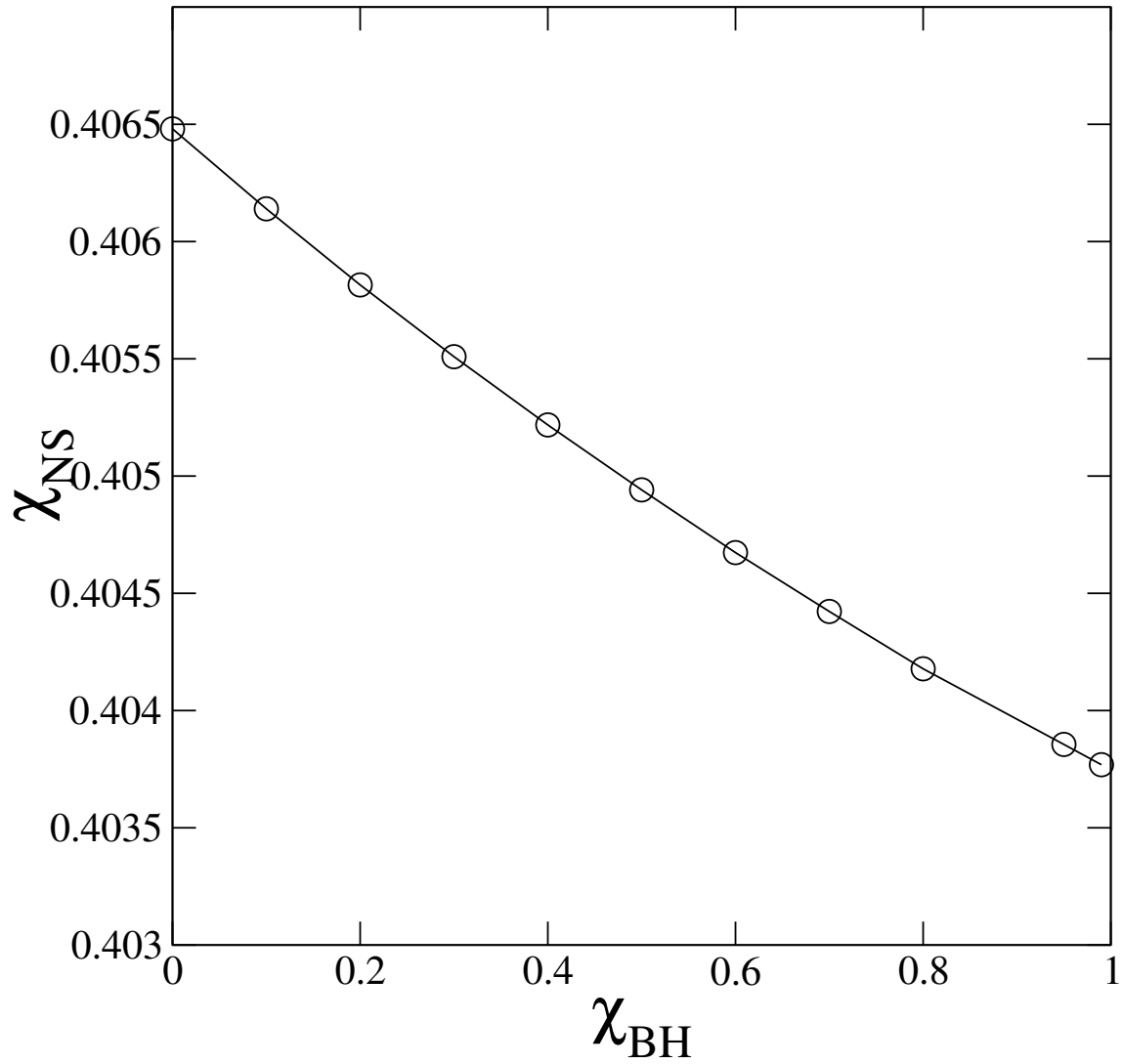Figure 4.4: Same as Fig. 4.3 but for the momentum constraint.

Figure 4.5: Neutron star spin χ_{NS} as a fucntion of black hole spin χ_{BH} for this sequence. We notice a small but significant downward linear trend. Can we explain this?
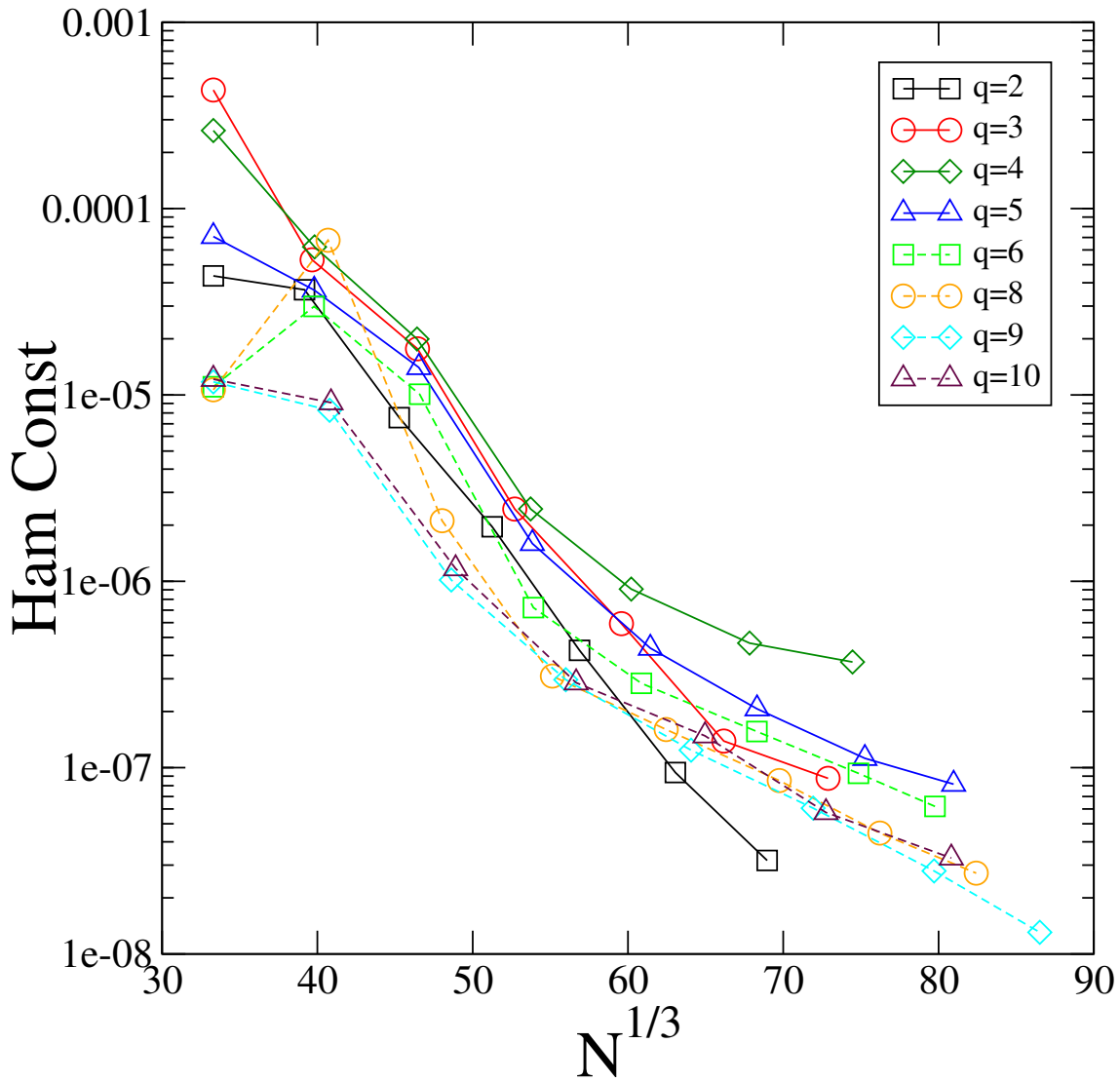
Figure 4.6: Hamiltonian constraint versus resolution for our sequence of binaries where the mass ratio is varied from $q = 2$ up to $q = 10$. The neutron star spin is constant at $\chi_{NS} \sim 0.4$ and the black hole spin is $\chi_{BH} = 0.9$. We find exponential convergence, as expected, in all cases.
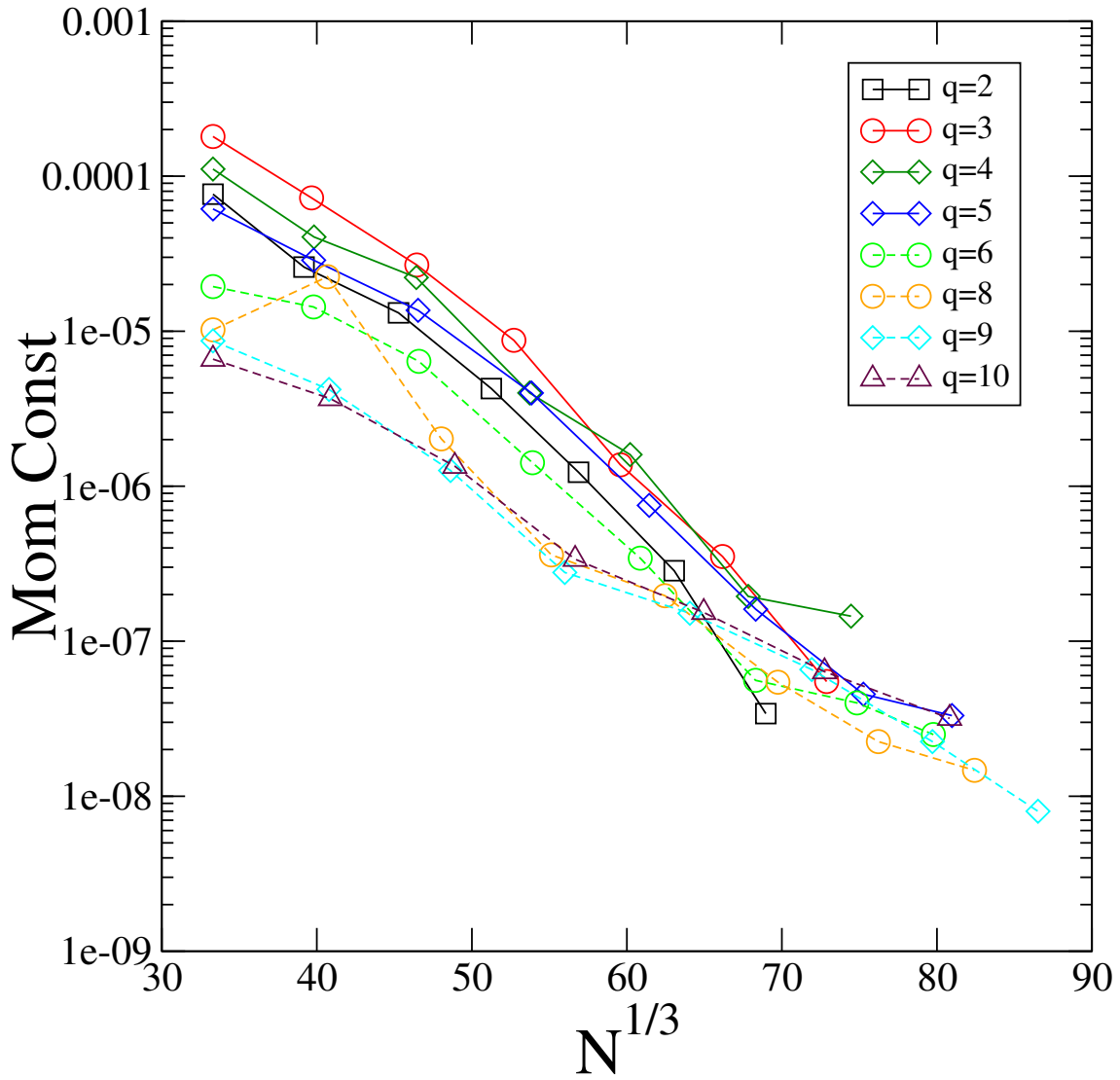
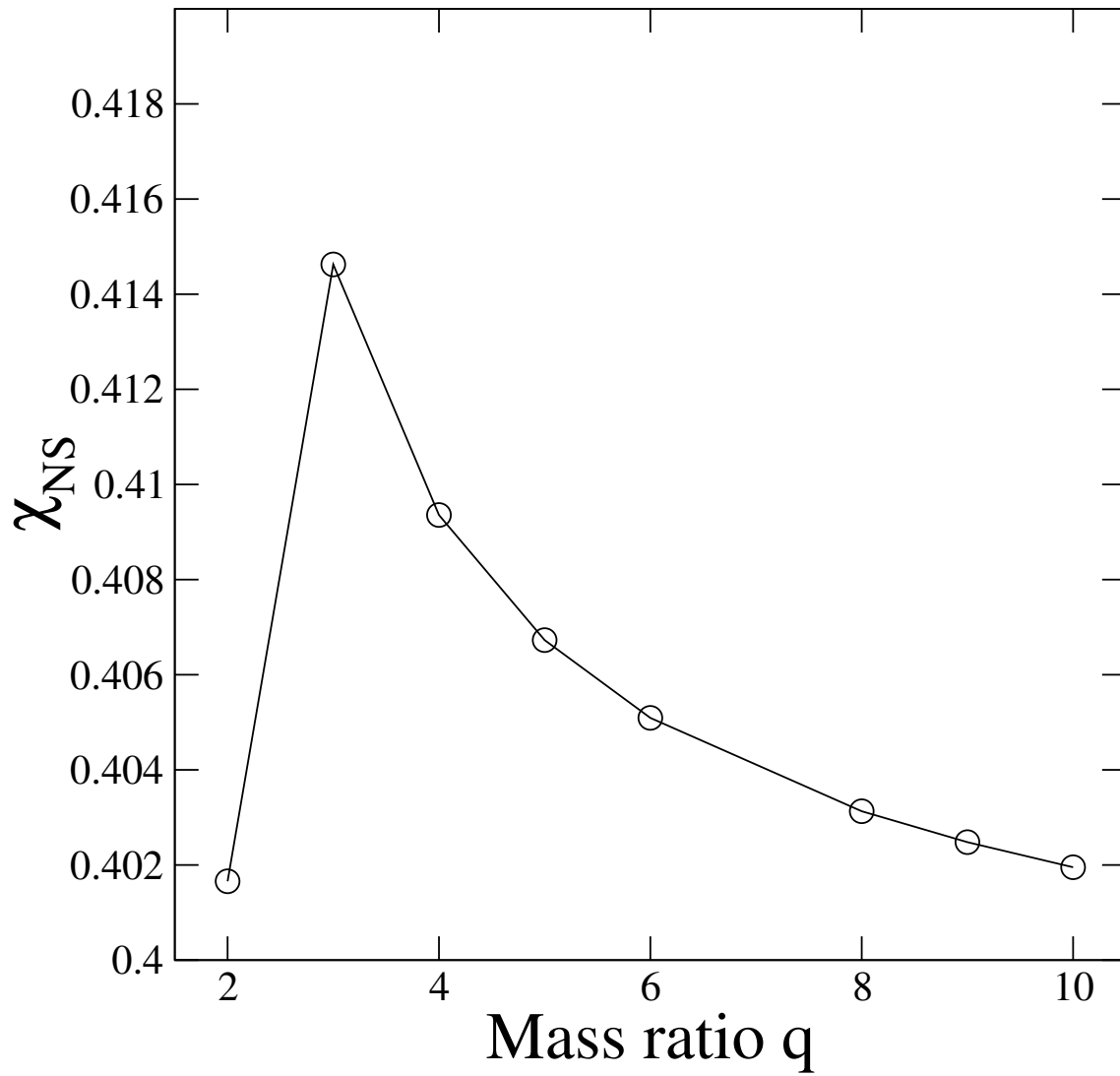Figure 4.7: Same as Fig. 4.6 but for the momentum constraint.

Figure 4.8: Neutron star spin χ_{NS} as a function of mass ratio q for this sequence. We notice a downward trend for $q \geq 3$. Can we explain this?
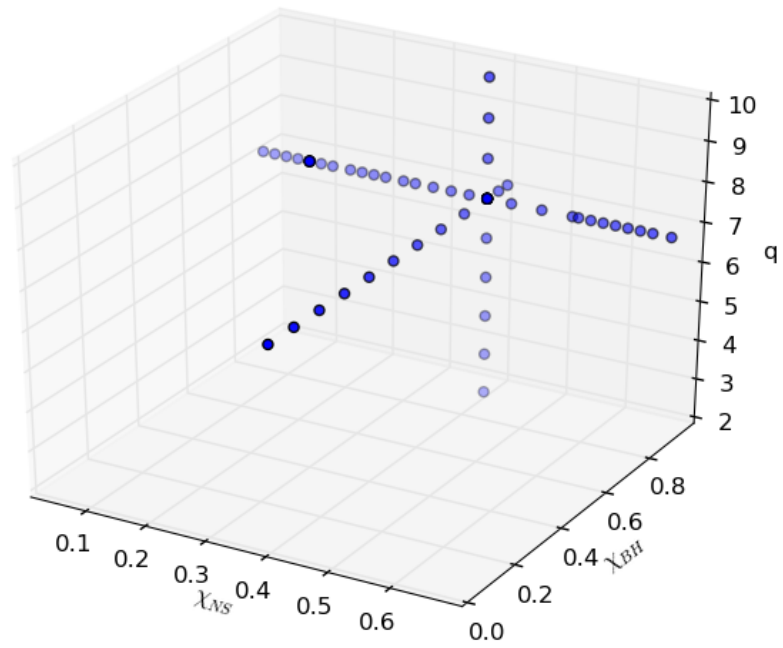
Figure 4.9: A parameter space scatter plot summarized where our sets of initial data have covered. The three axes are the magnitude of the black hole spin, the magnitude of the neutron star spin, and the mass ratio.

Chapter 5

Junk Radiation in Binary Black Hole Simulations

5.1 Chapter Overview

An Overview of my chapter here.

5.2 Chapter TDL

- Many citations in the introduction and very much out of date. It should be re-written.

- Are there any new papers on junk radiation to discuss that have come out since this time? Ask Harald / do a literature search.

- Discuss more about boundary conditions in IVP for bbh

- Maybe make a table detailing all the simulations that were done. Come up with a better naming system for the runs.

- There is a note about the uncertainity from numerical trunctation in E_J for SKS. Not sure what to do about that. I think it can reasonably left the way it is.

- Combine data into a single plot for wave extraction plot

- Decide what to do for δM for SKS, given that the data is so weird

- Write the results section closely citing all the figures properly. Are we overfitting the data? Be careful with how to report the data. Maybe just focus on the plots, and not the fits.

- Write a conclusion. What are the implications of these kinds of numbers?

5.3 Introduction

The inspiral and merger of solar-mass binary black holes are one of the most promising sources for ground-based gravitational wave detectors such as LIGO Barish & Weiss (1999), VirgoAcernese et al. (2006), and LCGTKuroda & the LCGT Collaboration (2010). In the next few years, as it is upgraded to higher sensitivity, Advanced LIGO is expected to begin making detections, with a realistic event rate estimated at about 20 per year Abadie et al. (2010). For the gravitational radiation to be detected, and to learn about the properties of the source, waveform templates must be accurately modelled. Although analytic prescriptions like Post-Newtonian (PN)Blanchet (2006) or Effective One-Body (EOB)Buonanno & Damour (1999) can accurately model some of the inspiral, Numerical Relativity (NR) simulations are needed to accurately model late inspiral and merger of the black holes.

In current NR simulations, there is always a burst of spurious gravitational radiation at the start of the simulation, often referred to as "junk radiation". This pulse always occurs at the start of the simulation, it is of much higher frequency and amplitude than the astrophysical gravitational radiation, and it has significant contributions from modes other than the standard $(l, m) = (2, 2)$ spherical harmonic mode, which is the dominant contribution for the astrophysical part of the waveform. Therefore, this pulse is not astrophysical.

We illustrate this effect in Fig. 5.1, showing the gravitational waveform at the start of a typical simulation. The waves are extracted on a coordinate sphere at $r = 160M$ [1], so the waves start appearing at $t \approx 160M$. We see the burst of junk radiation last about $100M$ in time, with significant contributions from both the $(2, 2)$ and $(2, 0)$ modes. The junk radiation then dies out, and subsequently, the expected sinusoidal $(2, 2)$ mode emerges.

This junk radiation is undesirable in simulations for several reasons. It adds to the computational cost of the simulation as the junk radiation must leave the computational grid before any useful physical information can be extracted. It can unrealistically shorten the time until the black holes mergeBode et al. (2008). It also makes it more difficult to compare general relativistic simulations with Post-Newtonian calculations. It is therefore a useful endeavour to try to better understand the junk radiation, how important it is, and how to reduce it.

Junk radiation is thought to be caused by assumptions made during the initial data construction, which are not compatible with black holes in perfect equilibrium. Specifically, black holes are generally treated in the initial data as independent and non-interacting, while in reality there should be some non-trivial tidal interactions between them. If we imagine a sequence of initial data sets where the initial separation between the holes is decreasing, we would expect that this effect becomes more important as the initial separation decreases. Moreover, the black holes in the initial data are often constructed with techniques that do not even allow to construct a single, equilibrium black hole. Specifically, often, conformal flatness is assumed. As detailed in section 5.4.1, the construction of initial data has a free choice for the conformal metric, $\tilde{g}_{ij}$, on the initial hypersurface. A common choice is conformal flatness, i.e., $\tilde{g}_{ij}$ is equal to the flat Euclidean metric. Since every spherically symmetric space is conformally flat, this would be fine for one Schwarzschild black hole. However, a binary system of compact objects

---

[1]We use units where $G = c = 1$. The only natural length and time scale is then the total mass of both black holes, M.
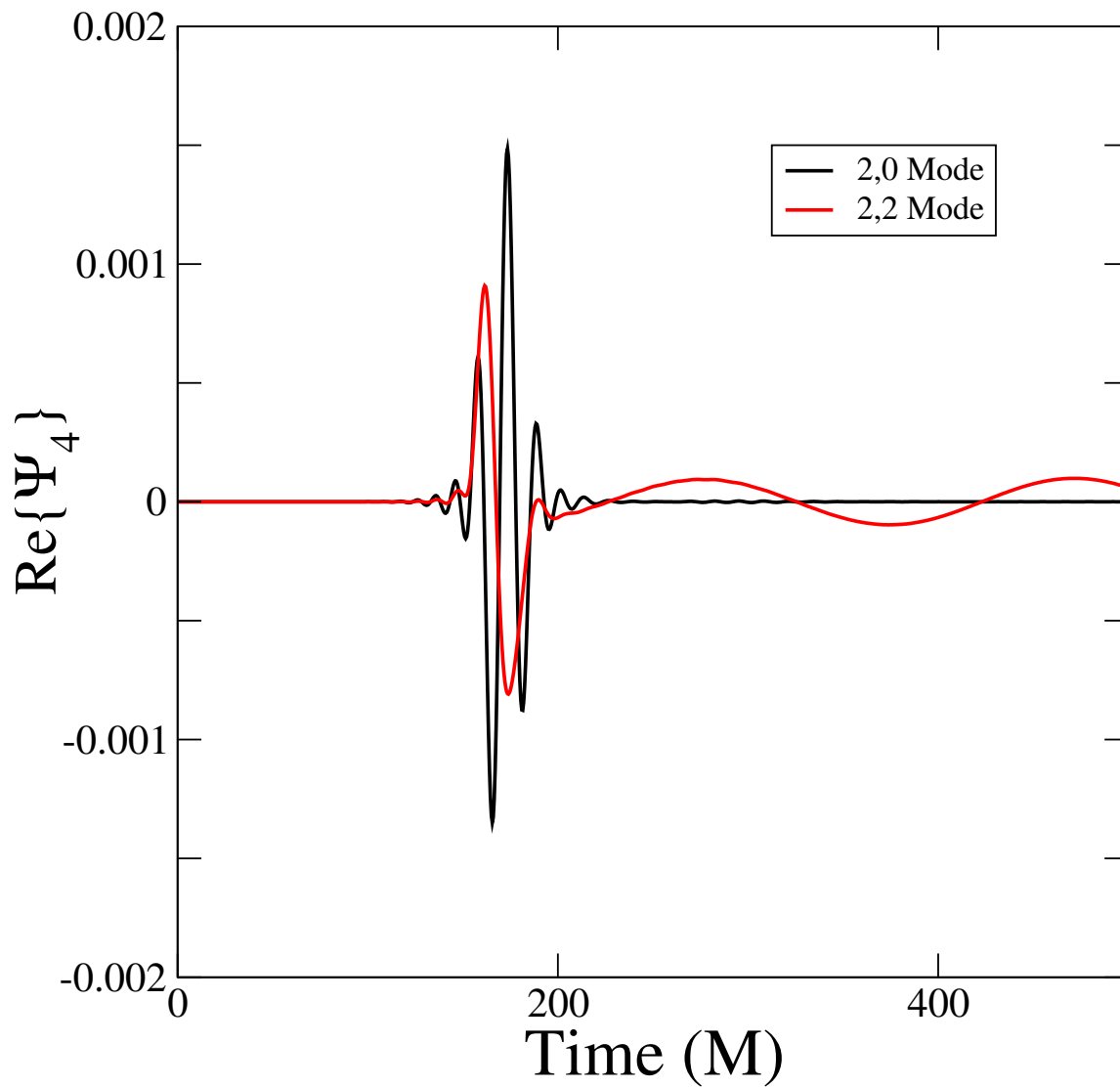
Figure 5.1: A typical run illustrating the spurious burst of junk radiation. We see at early times a burst of high-frequency, high-amplitude radiation. At later times, the $(2,0)$ mode dies out, and the $(2,2)$ mode settles into the usual inspiral-type radiation

is not conformally flat at second PN orderRieth (1997), and the Kerr space-time does not admit a conformally flat slicing Garat & Price (2000) that continuously approach Schwarzschild coordinates as the spin goes to zero. The former effect should decrease in importance with increasing separation of the binary. The latter is caused by a deficiency of conformally flat slicing that is present even for single spinning black holes, and so we expect its importance to be approximately independent of binary separation.

Lovelace Lovelace (2009) investigated the effects on junk radiation of using superposed Kerr-Schild Matzner et al. (1998); Marronetti & Matzner (2000); Pfeiffer et al. (2002); Lovelace et al. (2008) (conformally curved) initial data for equal mass, non-spinning black holes. The metric is written as

$$\tilde{g}_{ij} = f_{ij} + e^{-(r_A/w)^2} \left(g_{ij}^A - f_{ij} \right) + e^{-(r_B/w)^2} \left(g_{ij}^B - f_{ij} \right), \tag{5.1}$$

where f_{ij} is the Euclidean metric, $r^{A,B}$ are the distances from black holes A and B, and $g_{ij}^{A,B}$ is the Kerr-Schild metric boosted in the direction of the black hole's motion. This has the effect that the metric looks like Schwarzschild near the black holes, and looks flat far away. The Gaussian scalings were needed to help improve the convergence of the initial data. It was found that in general, the conformally curved initial data can decrease the amplitude of the junk radiation by a factor of ~ 2. Superposed Kerr-Schild initial data is built around the Kerr-Schild metric, which exactly represents single spinning black holes. Therefore, one would expect that the advantages of superposed Kerr-Schild become particularly apparent for spinning black holes.

In this paper we investigate the parameter space dependence of junk radiation. We measure its dependence on the spin and on the initial separation of the black holes, for low eccentricity, equal-mass, spin-aligned binaries. We also perform a comparison between conformally flat initial data, and superposed Kerr-Schild initial data.

The paper is organized as follows: Section 5.4 presents the numerical methods, and Section 5.5 describes how we quantify junk radiation and other initial transients in the

BBH initial data sets. We present our results in Sec. 5.6 and close with a discussion in Sec. 2.6.

5.4   Numerical Methods

5.4.1   The Initial Value Problem

Employing the usual 3+1 decomposition Arnowitt et al. (1962); York, Jr. (1979) space-time is foliated by a family of spacelike hypersurfaces Σ_t. Each hypersurface has a future-pointing unit normal n^μ, induced metric g_{ij}, and extrinsic curvature $K_{\mu\nu} = -\frac{1}{2}\mathcal{L}_n g_{\mu\nu}$. The metric is written as

$$g_{\mu\nu} = -\alpha^2 dt^2 + g_{ij}\left(dx^i + \beta^i dt\right)\left(dx^j + \beta^j dt\right),\tag{5.2}$$

where α and β are the lapse function and the shift vector respectively. The lapse measures the proper time between neighbouring hypersurfaces, and the shift vector determines how coordinate labels move between neighbouring hypersurfaces. On the initial hypersurface Σ_0, spatial metric and extrinsic curvature must satisfy the vacuum constraint equations

$$R + K^2 - K_{ij}K^{ij} = 0,\tag{5.3}$$

$$\nabla_j\left(K^{ij} - g^{ij}K\right) = 0.\tag{5.4}$$

To solve the constraint equations one writes Lichnerowicz (1944) the metric in terms of a conformal metric $\tilde{g}_{ij}$ and a conformal factor Ψ:

$$g_{ij} = \Psi^4 \tilde{g}_{ij}.\tag{5.5}$$

We also split the extrinsic curvature into trace and trace-free parts

$$K^{ij} = A^{ij} + \frac{1}{3}g^{ij}K,\tag{5.6}$$

and employ the extended conformal thin sandwich formalism York (1999); Pfeiffer & York (2003) to further decompose A^{ij}. One must then choose $\left(\tilde{g}_{ij}, \partial_t \tilde{g}_{ij}, K, \partial_t K\right)$ as the

free data. Compared to the extrinsic curvature decomposition Murchadha & York, Jr. (1974), the conformal thin sandwich formalism allows for physically motivated choices to a larger number of the free data. Elliptic equations with appropriate boundary conditions are then solved for Ψ, $\alpha\Psi$, and β^i, and the physical data is re-assembled. $\partial_t \tilde{g}_{ij} = \partial_t K = 0$ is chosen so that system is initially stationary in the co-rotating frame. This then leaves $\tilde{g}_{ij}$ and K as the free data to choose.

The two types of initial data we compare are described in detail in Ref. Lovelace et al. (2008): Conformally flat, quasi-equilibrium initial data employs conformal flatness, maximal slicing ($K = 0$) and inner boundary conditions that enforce that the black holes are instantaneously in equilibrium Caudill et al. (2006); Cook & Pfeiffer (2004); Cook (2002). Superposed Kerr-Schild initial data, first used in Marronetti & Matzner (2000); Matzner et al. (1998), takes the spatial metric and extrinsic curvature as superposition of elements of Kerr-Schild metrics (one for each black hole). As explained in Ref.Lovelace et al. (2008), we introduce Gaussian attenuation functions to ensure regularity at spatial infinity. Inner boundary conditions are PROVIDE DETAILS.

5.4.2   Code

The initial data is solved using the spectral solver `Spells` Pfeiffer et al. (2003) of the Spectral Einstein Code `SpEC` SpE (????). This is a multi-domain elliptic PDE solver that uses pseudo-spectral methods, whereby quantities of interest are expressed as a linear summation of basis functions. This method gives exponential convergence (with the number of basis functions) as long as the quantities of interest are smooth. The black hole singularities are dealt with by excision from the computational grid. We use the dual frame method described in Scheel et al. (2006). The domain decomposition and position of the black holes are fixed in a comoving frame, but the equations of motion are solved in an inertial frame that is asymptotically Minkowski. The frames are related by a rotation term (due to orbital motion) and a contraction term (due to inspiral motion).

Gravitational waves are extracted on outer spherical shells of the domain using the Newman-Penrose scalar Ψ_4. Given a spacelike hypersurface with unit normal n^μ and a spatial unit vector in the direction of wave propagation r^μ, Ψ_4 is defined as

$$\Psi_4 = -C_{\alpha\mu\beta\nu}l^\mu l^\nu m^\alpha \bar{m}^\beta \tag{5.7}$$

where $C_{\alpha\mu\beta\nu}$ is the Weyl tensor, $l^\mu = (n^\mu - r^\mu)/\sqrt{2}$ and m^μ is a complex null vector satisfying $m^\mu \bar{m}_\mu = 1$. We then expand Ψ_4 in spin-weighted spherical harmonics

$$\Psi_4(t, r, \theta, \phi) = \sum_{l,m} \Psi_4^{lm}(t, r)_{-2}Y_{lm}(\theta, \phi) \tag{5.8}$$

The number of terms used in this expansion is generally $l \leq 8$ in our simulations. At large r, Ψ_4 is related to the gravitational wave amplitude, h, by

$$\Psi_4 = \frac{d^2}{dt^2}h_+ - i\frac{d^2}{dt^2}h_\times. \tag{5.9}$$

5.4.3   Eccentricity Reduction

Gravitational radiation tends to circularize in-spiralling compact binaries Peters & Mathews (1963); Peters (1964). We reduce orbital eccentricity with an iterative method similar to the one described in Refs.Boyle et al. (2007); Chu et al. (2009). One guesses the initial orbital frequency Ω_0 from Kepler's third law or from a Post-Newtonian calculation, while assuming that the initial radial velocity, v_r is zero. After the first simulation has run for a sufficiently long length, about two orbits, we fit the time derivative of the orbital frequency, $\dot{\Omega}(t)$ as suggested in Buonanno et al. (2011). We fit parameters $\{A_0, A_1, T_c, B, \phi, \omega, q\}$ with the function

$$\begin{aligned}\dot{\Omega}(t) &= A_0 \left(T_c - t\right)^{-11/8} + A_1 \left(T_c - t\right)^{-13/8} \\ &+ B\cos\left(\varphi + \omega t + qt^2\right),\end{aligned} \tag{5.10}$$

where T_C is the time of merger. The first two terms represent the smooth inspiral motion of the black holes, while the oscillatory second terms represents unwanted effects due to

eccentricity. The updating formulae

$$\delta\Omega_0 = -\frac{B\omega\sin\varphi}{4\Omega_0^2} \qquad (5.11)$$

$$\delta v_r = \frac{Bd_0\cos\varphi}{2\Omega_0}, \qquad (5.12)$$

where d_0 is the binary separation, are designed to circularize low eccentricity Newtonian binaries. This process is continued iteratively, typically another one or two times, until the eccentricity is reduced to $e \lesssim 0.002$. The effect of eccentricity on junk radiation is discussed in section 5.5.2.

5.4.4 Simulations

We run BBH evolutions using both conformally flat and SKS initial data. We consider five different initial separations for CF data, $D/M = \{12, 15, 20, 25, 30\}$, and $D/M = \{12, 15, 20\}$ for SKS data, where M is the total mass of both black holes, and at each separation we consider six different spins, $\chi = \{0, 0.1, 0.2, 0.3, 0.4, 0.5\}$. In each case the black holes are of equal mass, equal spin, and the spin is aligned with the orbital angular momentum, i.e., in the the $+z$ direction. To test the convergence of quantities of interest, each run is done at four resolutions, which we will refer to has N0-N3. Each evolution is run to about $t = 1000M$, which is long enough to accurately measure the eccentricity, and make sure that it is sufficiently low. As discussed in section 5.5.2, sufficiently low means $e \lesssim 0.002$.

5.5 Methodology

We shall employ three diagnostics to measure the initial relaxation of the initial data, the outgoing pulse of radiation (junk radiation), the change in black hole mass during relaxation, and the change in black hole spin during relaxation.

5.5.1 Pulse in the Gravitational Waveform

In this section we discuss our methods of quantifying the amount of junk radiation present in a given simulation. It is not immediately obvious what the best way to do this is. Lovelace Lovelace (2009) considered the maximum value of the Newman-Penrose waveform, $\max\{r|\Psi_4^{lm}|\}$. The $(l, m) = (2, 2)$ and $(2, 0)$ modes were found to dominate. We find, however, that this method has some inadequacies. This is illustrated by comparing two runs (CF data, $D = 15M$, $\chi = 0.2$), one at our typical resolution N3, and another at a very high resolution, N7[2]. The $(2, 0)$ and $(2, 2)$ modes are shown in the top panel of Fig. 5.2. It is clear that the $(2, 0)$ mode is significantly different between N3 and N7, in both the largest peak and in the subsequent smaller peaks, and that these differences are not well encapsulated simply by $\max\{r|\Psi_4|\}$. In Fig. 5.2 we also show $|r\Psi_4|$ for an SKS run with the same parameters. The waveform is significantly different from the CF waveform in both the number of peaks and their relative heights, and it is clear that $\max\{r|\Psi_4^{lm}|\}$ does not encapsulate this waveform very well.

As a more robust quantity that incorporates the whole waveform, and is less resolution dependent than $\max|r\Psi_4^{lm}|$, we look at the total energy carried away from the system by gravitational waves. The gravitational wave energy flux is Boyle et al. (2008)

$$F(t) = \frac{1}{16\pi} \sum_{l,m} \dot{h}_{lm}^2(t) \tag{5.13}$$

where $h = h_+ - ih_\times$. $\dot{h}$ is related with Ψ_4 by

$$\dot{h}_{lm}(t) = \int_{t_0}^{t} \Psi_4^{lm}(t')dt' + H_{lm}. \tag{5.14}$$

where The H_{lm} is a constant of integration constants. To measure the initial pulse of radiation, we chose $t_0 = 0$ and $H_{lm} = 0$. The energy flux $F(t)$ is shown in the red curves in Fig. 5.3 for conformally flat initial data (top panel) and SKS initial data (bottom panel). The initial burst is apparent in these figures; at late times $t - R \gtrsim 40M$, $F(t)$

---

[2]It terms of the total number of basis functions X, $X^{1/3} \sim 58$ for N3 and $X^{1/3} \sim 78$ for N4
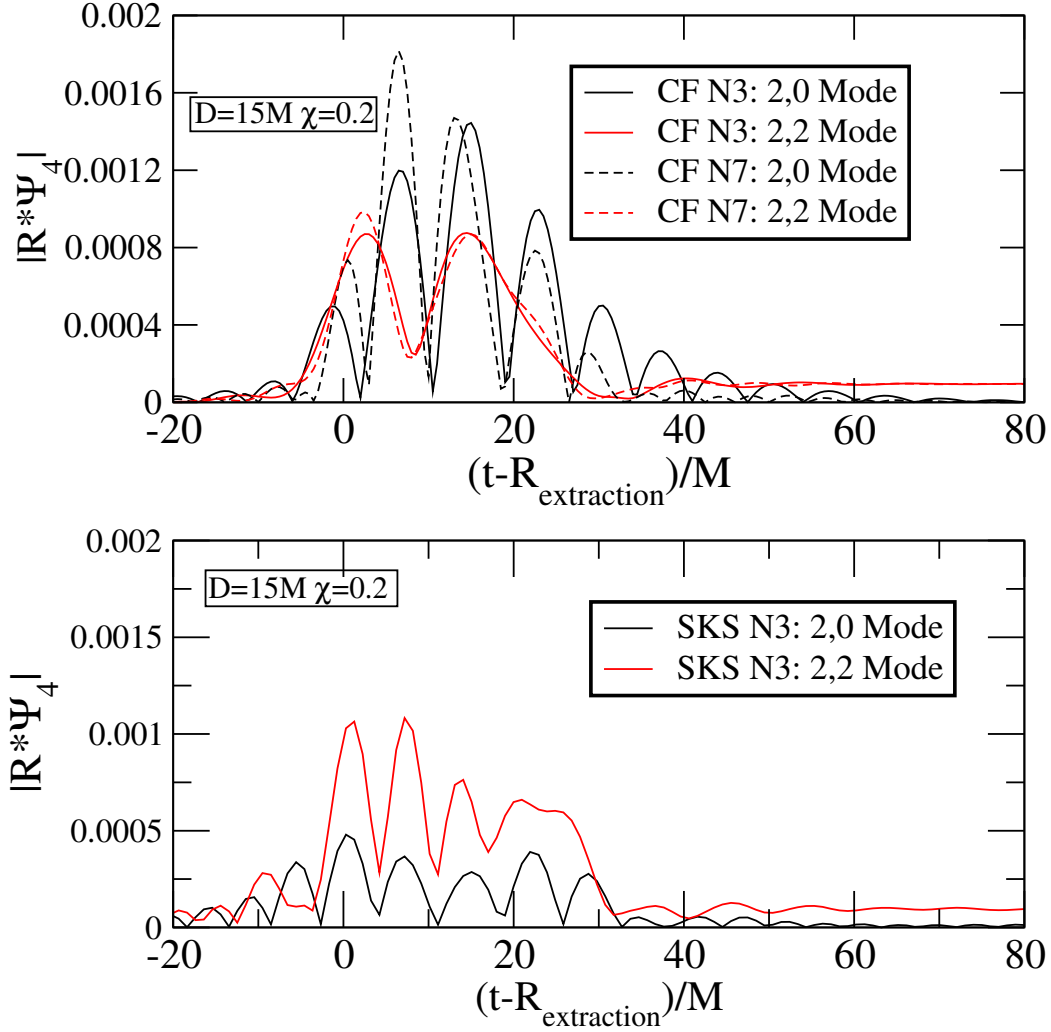
Figure 5.2: <u>Top Panel:</u> Comparison of the junk radiation profiles for our usual highest resolution (N3) and an additional run at very highest resolution (N7). We see, especially for the $(2,0)$ mode, that the maximum peak of the junk radiation is much higher for N7, but additional peaks are comparable or higher for N3.

<u>Bottom Panel:</u> Junk radiation profile for an SKS run with the same parameters as in the top panel. The waveform is significantly different in structure from the CF waveform.

approaches the nearly constant energy flux of the astrophysical inspiral. We are now faced with two problems: We would like to isolate the energy carried in junk-radiation from the energy-flux astrophysical inspiral. And, we would like to do so in a robust way, independent of arbitrary choices. We proceed as follows:

First, we assume that the astrophysical energy flux begins at a time t_{22}, i.e.

$$F_{22}(t) = F_0 \, \theta(t - t_{22}). \tag{5.15}$$

Here, F_0 represents the value of $F(t)$ after the pulse of junk-radiation and θ represents the step-function. The choice of a constant value F_0 is reasonable since the timescale on which F_{22} changes significantly is much longer than the junk radiation timescale. This energy flux is indicated by the blue dashed curves in Fig. 5.3. We will discuss our choice for t_{22} shortly. The energy in the junk-radiation is given by

$$E_J = \int_0^{t_C} \big[(F(t) - F_{22}(t)\big]dt, \tag{5.16}$$

where the cut-off time t_C is chosen after the junk radiation has decayed, i.e. $t_C - R \gtrsim 50M$. The energy attributed to the junk radiation is thus the shaded area in Fig. 5.3. As already apparent from Fig. 5.3, the precise value of t_C is irrelevant not really irrelevant because we discuss it later, because at late times $F(t) - F_{22}(t) \approx 0$.

It remains to chose a prescription for the choice of t_{22}, the time when we deem the astrophysical waveform to "turn on". A simple method would be to choose t_{22} to correspond to $\max\{F(t)\}$. This seems reasonable for the conformally flat curve in Fig. 5.3, but the more wide double-peaked structure of the SKS curve shows that another approach is needed. Instead we take t_{22} to correspond to the flux weighted centre of the junk radiation waveform. The first moment of $F(t) - F_{22}(t)$, in other words. So,

$$t_{22} = \frac{\int_0^{t_J} t(F(t) - F_0\theta(t - t_{22}))dt}{\int_0^{t_J} (F(t) - F_0\theta(t - t_{22}))dt}. \tag{5.17}$$

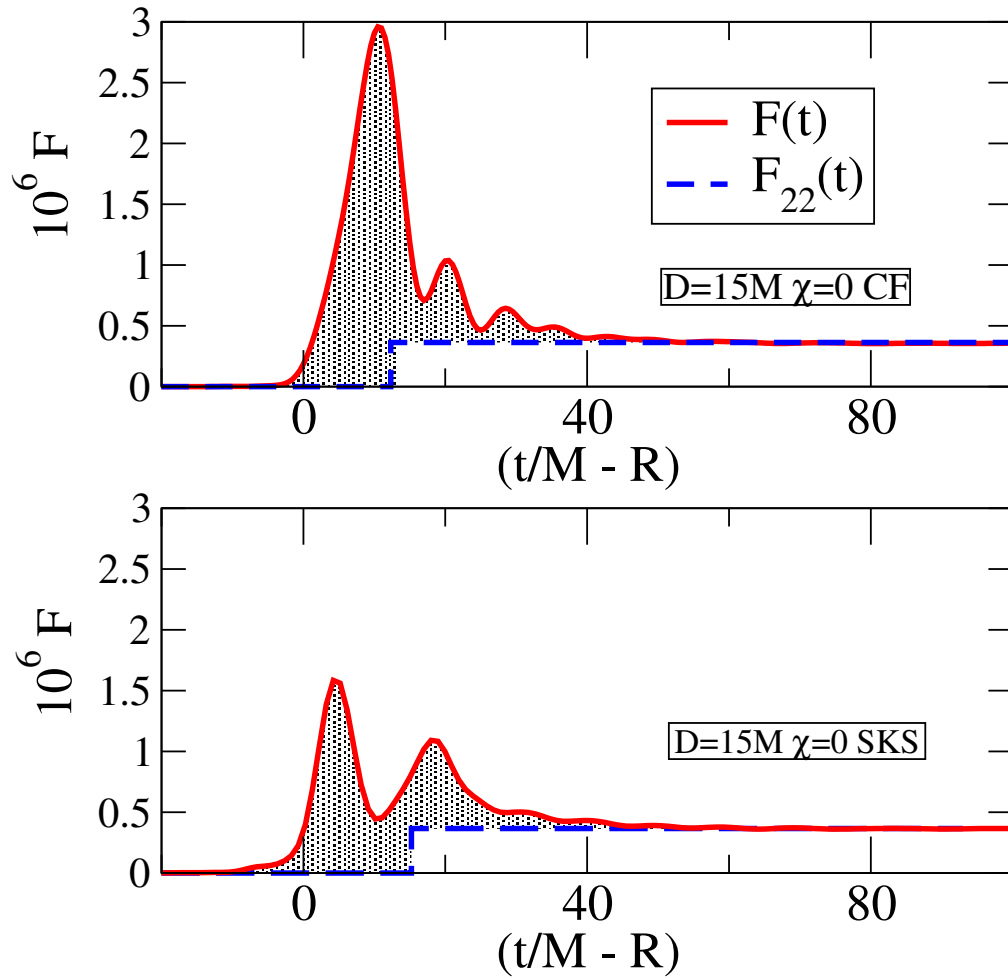This equation must be solved iteratively for t_{22}.

Figure 5.3: The flux $F(t)$ is plotted for two different runs, both with parameters $D = 15M$ and $\chi = 0$. Conformally flat initial data is in the top panel and SKS initial data is in the bottom panel. The solid red curve represents the total flux, $F(t)$. The dashed blue curve represents $F_{22}(t)$, the astrophysical flux that we subtract from $F(t)$. The shaded area between the two curves is the energy in junk radiation, E_J.

5.5.2   Uncertainty in E_J

Several effects may influence the quantity E_J computed by Eqs. (5.16) and (5.17). <u>Numerical truncation error</u> can be estimated by performing the simulations with different numerical resolution. Our simulations show that in general, E_J increases with resolution. This is because junk radiation is a short wavelength feature, so greater resolution allows for more of the features present to be captured. To estimate the uncertainty in E_J, we compare our $D = 15M$, $\chi = 0.2$ runs at N3 and N7, as discussed earlier. We find that at N7, E_J is about 13% greater than at N3. Since we don't have such high resolutions runs available for each of our cases, we assume that we can use this same 13% difference for each of our runs. We This also assumes that at N7 the junk radiation is nearly fully resolved, so that this difference is a good indication of the true value. [What about SKS – the technology is completely different, so a separate number needs to be determined] *Nick: Working on something here...*

A second uncertainty arises through the <u>choice of t_C</u>. This number is chosen manually for each run, introducing a subjective element into the analysis. Examining the flux curves in Fig. 5.3, for example, t_C could conceivably be chosen differently by $\sim 10M$ and still be a reasonable choice. Our definition Eq. (5.16) was meant to be robust to small changes in t_C. For E_J to be a robust measurement, it should therefore not change significantly in response to changes δt_C that are of that order. Indeed, this is enforced by our definition of E_J, which subtracts out the additional flux in the astrophysical $(2, 2)$ mode. To verify this assertion, we compute E_J with t_C in Eq. (5.16) replaced by $t_C + \delta t_C$. Figure 5.4 shows that indeed E_J is almost independent of δt_C. In Fig. 5.4, E_J is plotted against t_C in the representative $D = 15M$, $\chi = 0$ case. For each run we define a fractional error parameter due to the choice of t_C, where we average the differences for $\delta t_C = -10M$ and $\delta t_C = 10M$:

$$\frac{\Delta E}{E} = \frac{|E(t_C + 10M) - E(t_C)| + |E(t_C) - E(t_C - 10M)|}{2E(t_C)} \tag{5.18}$$

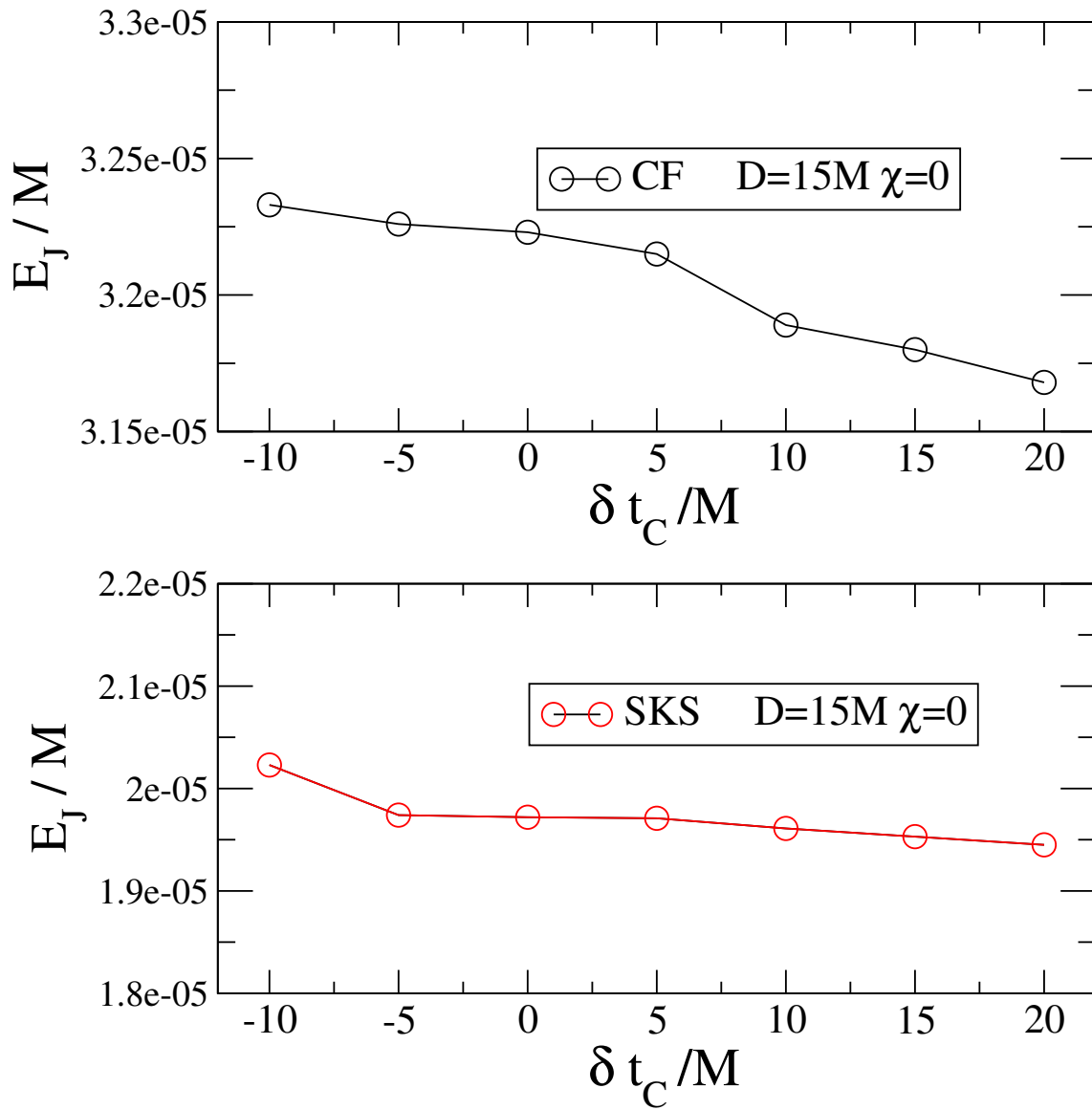This uncertainty ranges from $\sim 0.25\%$ to $\sim 3.75\%$ throughout all of ours runs.

Figure 5.4: E_J is plotted against δt_C, representing changes to the selected value of t_C for runs where $D = 15M$, $\chi = 0$. The results for conformally flat initial data are shown in the top panel, and SKS initial data in the bottom panel. Typical changes in E_J are on the order of a few percent.

A third error in E_J arises through the finite radius of gravitational wave extraction. In this study, gravitational waves are extracted at radii $R_{\text{ex}} \sim 300 - 400M$. Gravitational waves extracted at finite radii are subject to near-field effects which may cause the extracted waveforms to differ from the one that would be observed at infinity. To estimate the error in E_J due to the finite extraction radius, we use the following procedure. For each of our runs, we take E_J at several extraction radii, and examine E_J as a function of $1/R_{ex}$. We then extrapolate

$$E_\infty = \lim_{1/R_{ex}\to 0} E_J(1/R_{\text{ex}}) \tag{5.19}$$

using a linear fit in $1/R_{\text{ex}}$ to estimate the behaviour of E_J at infinity. We then take the fractional difference

$$\frac{\Delta E}{E} = \frac{E_\infty - E_J}{E_J} \tag{5.20}$$

as our error estimate. This parameter is on the order of 10% for most of our runs. Note, however, that we still use E_J and not E_∞ as our measure of energy in the pulse. In Fig. 5.5 we illustrate an example of this procedure, plotting E_J vs. $1/R_{ex}$ for one case, $D = 15M\chi = 0$, for both CF and SKS data.

[To clarify: You perform 1/R extrapolation separately for every configuration? That's a lot of work.]*Nick: Yes - at every D for both CF and SKS; but not at each spin. They're similar enough that I use the $\chi = 0$ estimate for each spin.*

A final factor that could influence the estimated E_J is the eccentricity of the orbit of the black holes. Previously we argued that it is important for astrophysically realistic binaries to have low eccentricity. We now consider how it affects the junk radiation, specifically the effect on E_J. We examine the case $D = 25M\chi = 0.1$ for CF data, as this particular case led to a fairly large range of eccentricities in the reduction process; $e \sim \{0.03, 0.008, 0.0006\}$. The measured E_J for these three cases is $10^6 E_J = \{7.053 \pm 0.38\%, 7.204 \pm 0.53\%, 7.174 \pm 0.58\%\}$. Here, the quoted uncertainty is purely due to the choice of t_C. The differences between the first two eccentricities is 2.10% and it is 0.42%
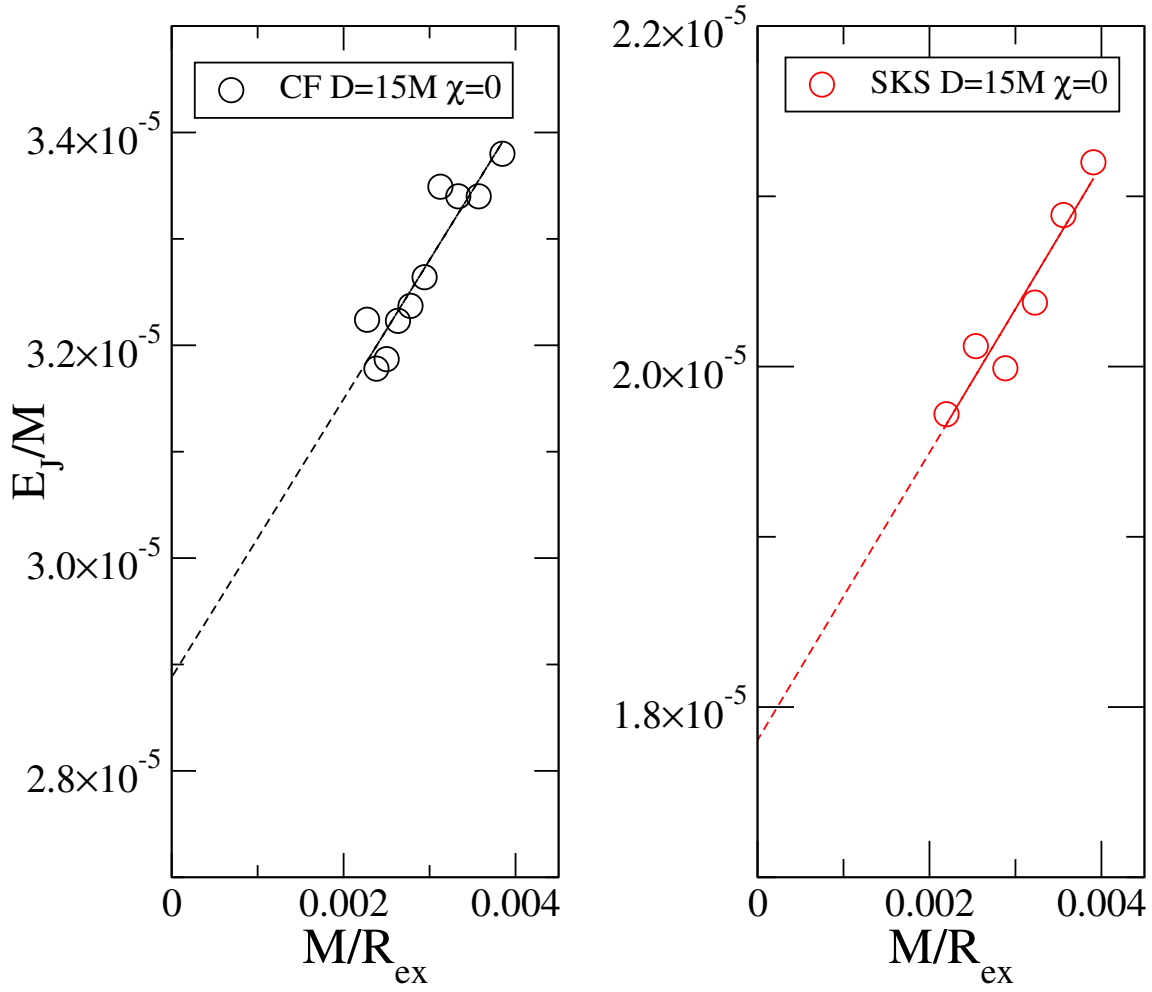
Figure 5.5: E_J as a function of $1/R_{ex}$, where R_{ex} is the extraction radius. This is for the case where $D = 15M$, $\chi = 0$, with CF initial data in the left panel and SKS initial data in the right panel. The extrapolation to $1/R_{ex} \to 0$ allows us to estimate the error on E_J due to finite extraction radius effects. [Combine data into single plot]

for the last two. Because the latter difference is less than the uncertainty due to the choice of t_C, the two runs are effectively indistinguishable, and we conclude that we can safely ignore the effects of residual eccentricity once we have $e \lesssim 0.008$. However, to be "safe", we have generally reduced the eccentricity of all of our runs to $e \lesssim 0.002$.

5.5.3 Transient behaviour in Black Hole quantities

Mass Increase

Besides the energy carried away in junk radiation, we utilize two further diagnostics of transients ~~due to~~ arising from imperfect initial data. The first diagnostic is the irreducible mass of the black hole, $M_{irr} = \sqrt{A/(16\pi)}$, where A is the area of the black hole's apparent horizon. In the first few M during the evolution, the apparent horizon mass $M_{\mathrm{irr}}(t)$ increases by a small amount, before settling down to an approximately constant value. This effect is easily apparent for CF initial data plotted in the upper panel of Fig. 5.6. We characterize the increase in mass due to initial transients by

$$\delta M(t) = \frac{M_{irr}(t)}{M_{irr}(0)} - 1 \tag{5.21}$$

and the equilibrium parameter $\delta M_{eq} = \delta M(t_{\mathrm{eq}})$. Here t_{eq} is a time where the mass-increase is complete, and levels off; typically $\sim 20M$.

For SKS initial data the behaviour of $M_{\mathrm{irr}}(t)$ is more complex. Within the first few M, $M_{\mathrm{irr}}(t)$ shows a rapid, albeit small increase, presumably due to relaxation of the geometry in the immediate vicinity of the black holes. The trend here is similar to the CF initial data, in that larger spins result in a larger increase of $M_{\mathrm{irr}}(t)$, albeit the magnitude of the increase is about a factor 50 smaller for SKS initial data. Subsequently, starting at $t \sim 40M$, the SKS-runs show a second set of features, ~~rather large amplitude~~ oscillations with amplitude $\sim 2 \times 10^{-5}$ lasting about $60M$. The features of these oscillations are similar to each other even for runs with different spin χ. Therefore, it is likely that these oscillations are caused by features in the initial data set <u>away</u> from the black holes.

[Revisit what to do with this text] In Fig. 5.6, curves of $M_{irr}(t)$ are shown at different spins, at constant $D = 15M$, with Conformally flat initial data in the top panel, and SKS initial data in the bottom panel. There is a clear qualitative between the CF and SKS curves. The CF data evidently forms a increasing sequence of δ_M with χ, and δ_M is clearly well-defined in each case. However, the SKS data exhibits oscillatory behaviour that is relatively spin independent, and there is not a clear way to define δ_M. The scale of the oscillations is on the order of 10^{-5}. Our conclusion is that these are numerical oscillations and the contribution from junk radiation is not directly measurable, and we do not seek to characterize their parameter space dependence any further.

Figures 5.7 and 5.8 show convergence tests for one of the spin-values shown in Fig. 5.6. ($D = 15M$, $\chi = 0.3$). The top panels of Figs. 5.7 and 5.8 show $M_{\mathrm{irr}}(t)$ of one black hole computed at different numerical resolutions, and the bottom panels show differences in $M_{\mathrm{irr}}(t)$ computed at neighbouring resolutions. Note that our parameter space studies presented in Sec. 5.6 were usually performed on resolution "N3"; we have run "N4" only for select cases to test convergence. The CF initial data shows rapid convergence and the features in the upper panel of Fig. 5.6 are well resolved. For the SKS data, Fig. 5.8 indicates convergence, albeit much more slowly.

The magnitude of the change of $M_{\mathrm{irr}}(t)$ is much smaller for SKS initial data than for CF initial data ($\sim 10^{-5}$ vs. $\sim 5 \times 10^{-4}$). The changes in $M_{\mathrm{irr}}(t)$ for SKS initial data approach our numerical truncation error, and are furthermore ambiguous due to the extra features apparent in Fig. 5.6. Therefore, we shall not attempt to quantify them ~~below~~ in detail, beyond giving upper bounds of the change on M_{irr} for SKS data.

Spin Decrease

Our third and final quantification of junk radiation comes from the black hole's spin $S(t)$. At early times in each simulation –seen in Fig. 5.9, the spin of each black hole decreases and oscillates rapidly. Eventually, at some time t_{eq}, the spin reaches some approximately constant value, which is lower than the initial spin, $S(0)$. This effect can be interpreted
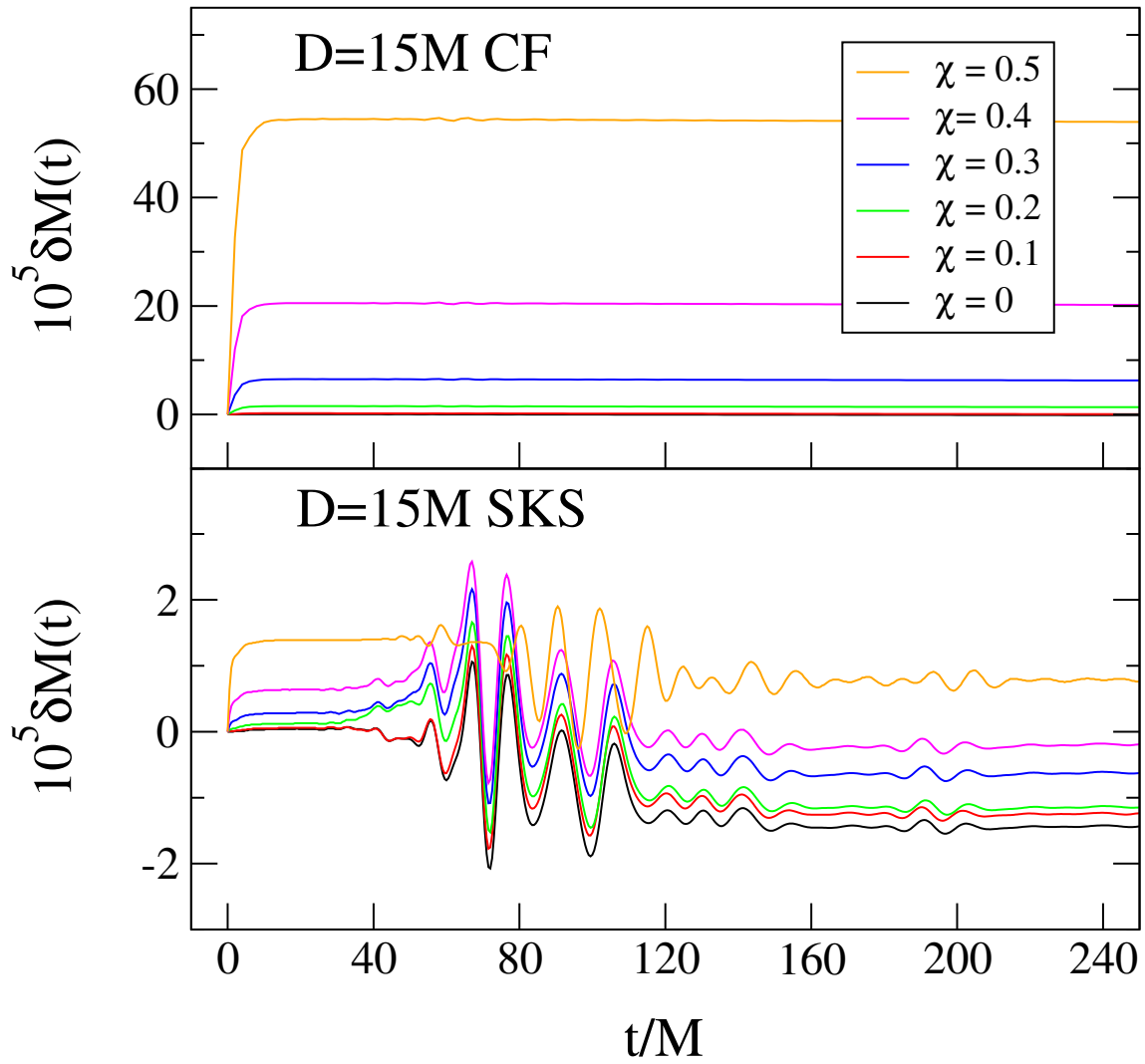
Figure 5.6: Normalized irreducible mass curves for CF data (top panel) and SKS data (bottom panel) for all of the different spins in the covered parameter space and $D = 15M$ remaining constant.
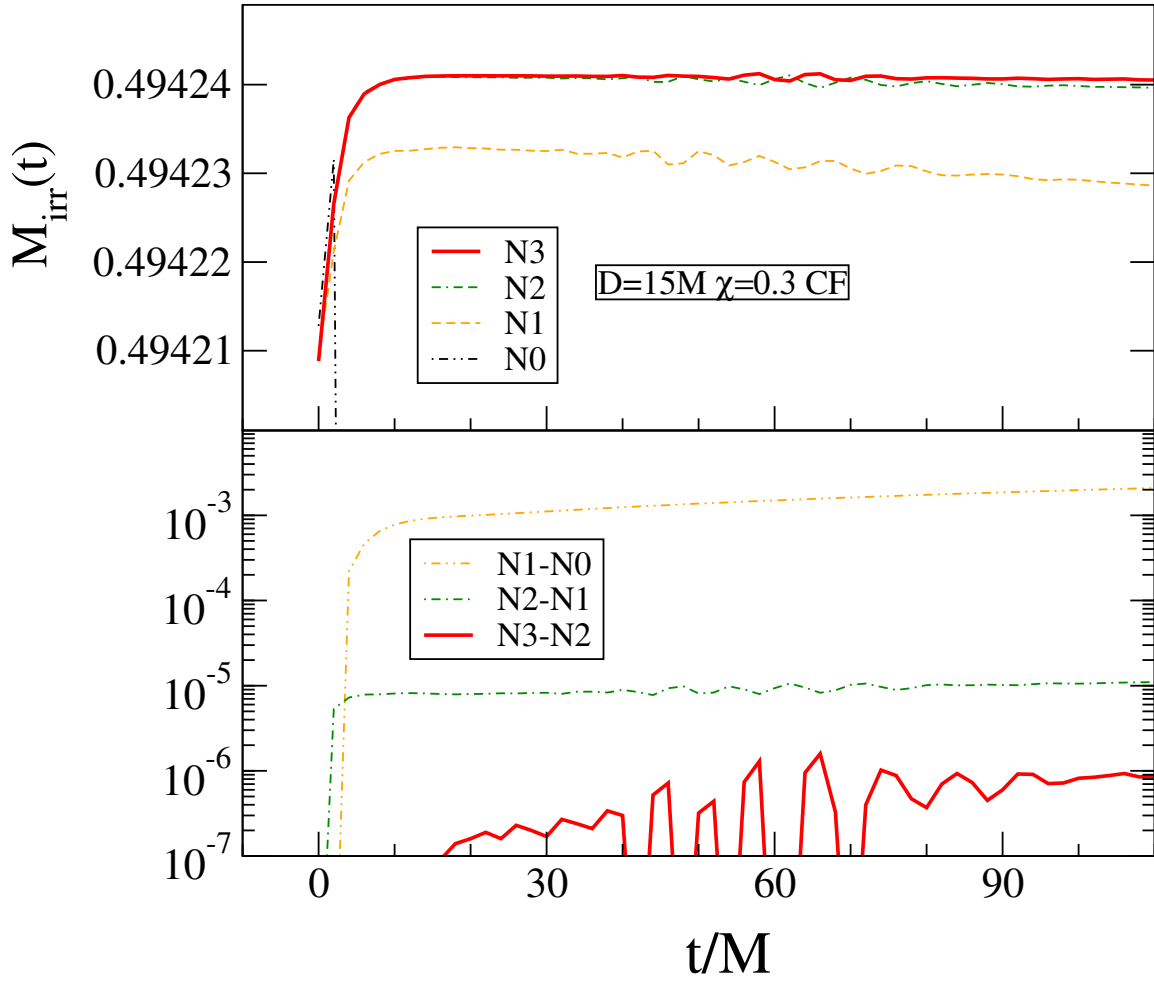
Figure 5.7: Convergence test of $M_{irr}(t)$ for SKS initial data in the case $D15 = M$, $\chi = 0.3$. The top panel shows $M_{irr}(t)$ at different resolutions, and the bottom panel shows the difference between consecutive resolutions.
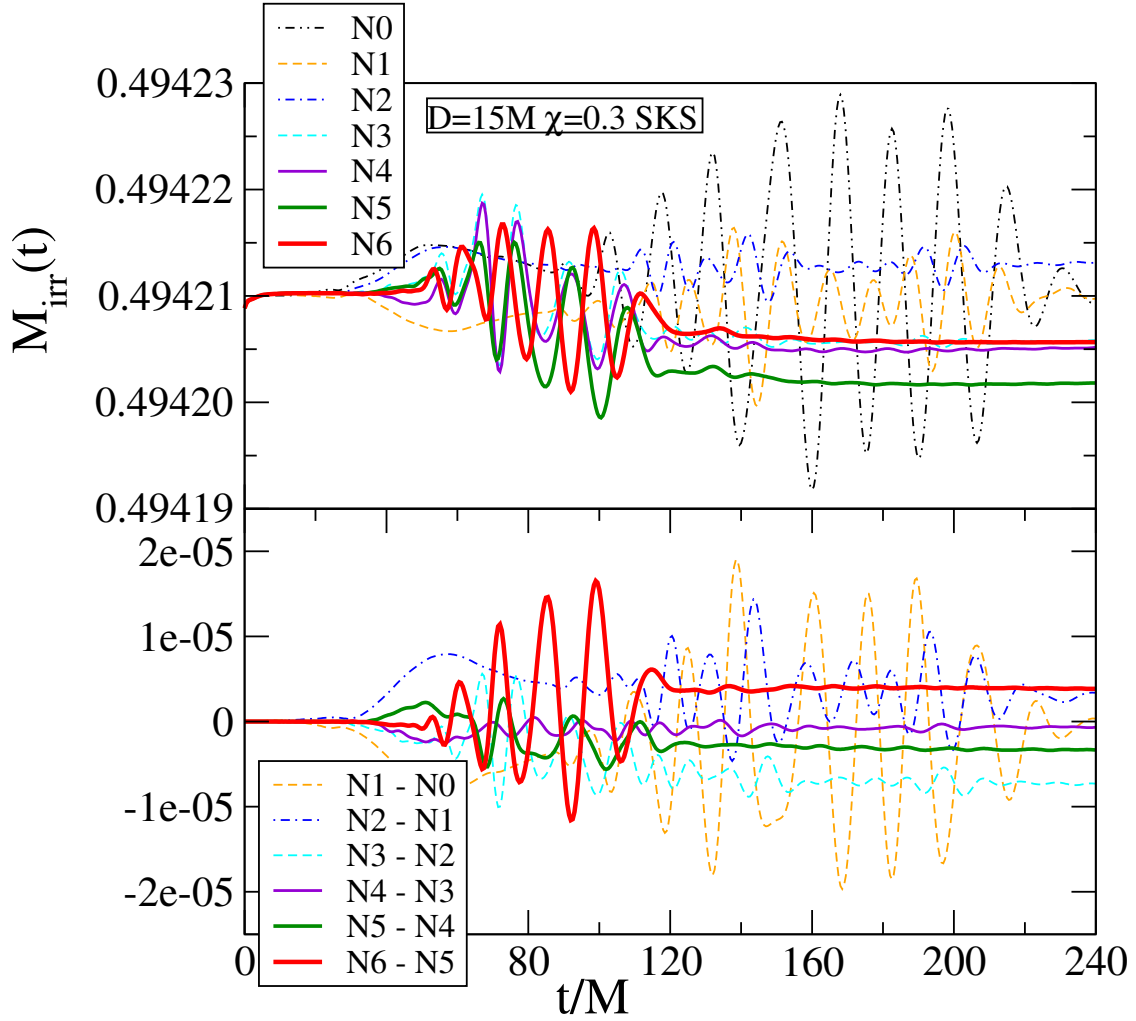
Figure 5.8: Same as Fig. 5.7 but for SKS data [make same changes to figure as indicated in Fig. 6]

as angular momentum being carried away from the system by junk radiation. Note that we use the dimension-ful quasi-local angular momentum, measured with approximate Killing vectors as described in Lovelace et al. (2008). We use S rather than $\chi = S/M^2$ to de-couple the change in spin from the change in mass.

Analogous to $\delta M(t)$, we can define the parameter $\delta S(t)$ as the fractional spin decrease of the black hole:

$$\delta S(t) = \frac{S(t)}{S(0)} - 1 \tag{5.22}$$

and the equilibrium parameter $\delta S_{eq} = \delta S(t_{eq})$, where t_{eq} the time when $\delta S(t)$ has reached some nearly constant value. In practice, we compute δS_{eq} as the average value of $\delta S(t)$ over some suitable interval around t_{eq}.

Analogous to Figs. 5.7 and 5.8, Figs. 5.8 and 5.7 [Fix figure numbers] demonstrate convergence tests for $\delta S(t)$, again for the case $D = 15M, \chi = 0.3$. Similar to what was see in the convergence test for $M_{\mathrm{irr}}(t)$, the CF data convergences rapidly, while we see no clear convergence in the SKS data going up to N6.

5.6 Results

5.6.1 Energy in Junk Radiation

Figure 5.11 shows the energy in the pulse of junk radiation, for all of our runs, as a function of spin. It is clear that within the uncertainty of our simulations, E_J has virtually no dependence on the spins of the black holes. The only exception may be that for conformally flat data, E_J seems to increase as $\chi \to 0.5$. This is most visible in the $D = 12M$ case. Perhaps the dependence of E_J on χ could become important for $\chi > 0.5$ if this trend continues.

Because, as we've shown in Fig. 5.11, there is virtually no dependence of E_J on χ, in looking at the dependence of E_J on D, we can use a fixed χ; we use $\chi = 0$. Figure 5.12
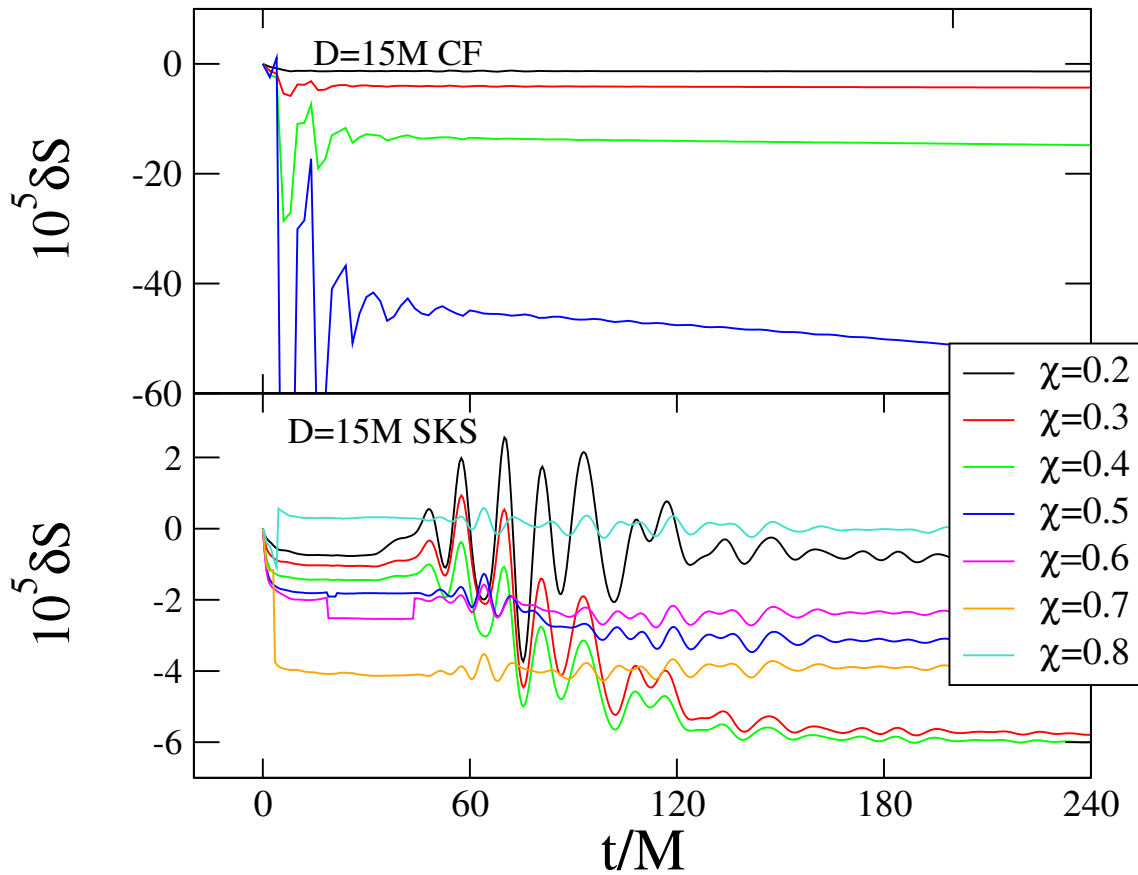
Figure 5.9: Fractional change in spin relative to $t = 0$, $\delta S = S(t)/S(t = 0) - 1$. The top panel shows conformally flat initial data and the bottom panel SKS data (note the different scale). All simulations at distance $D = 15M$.
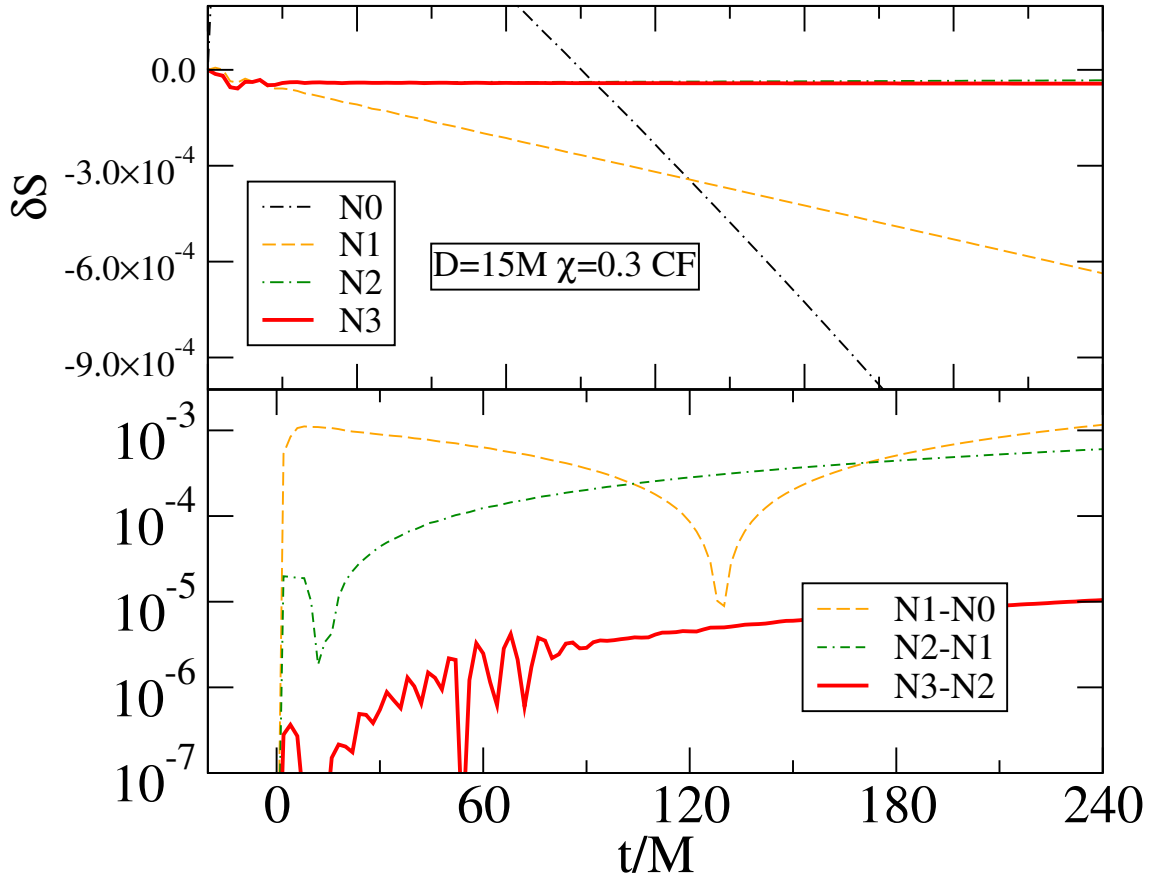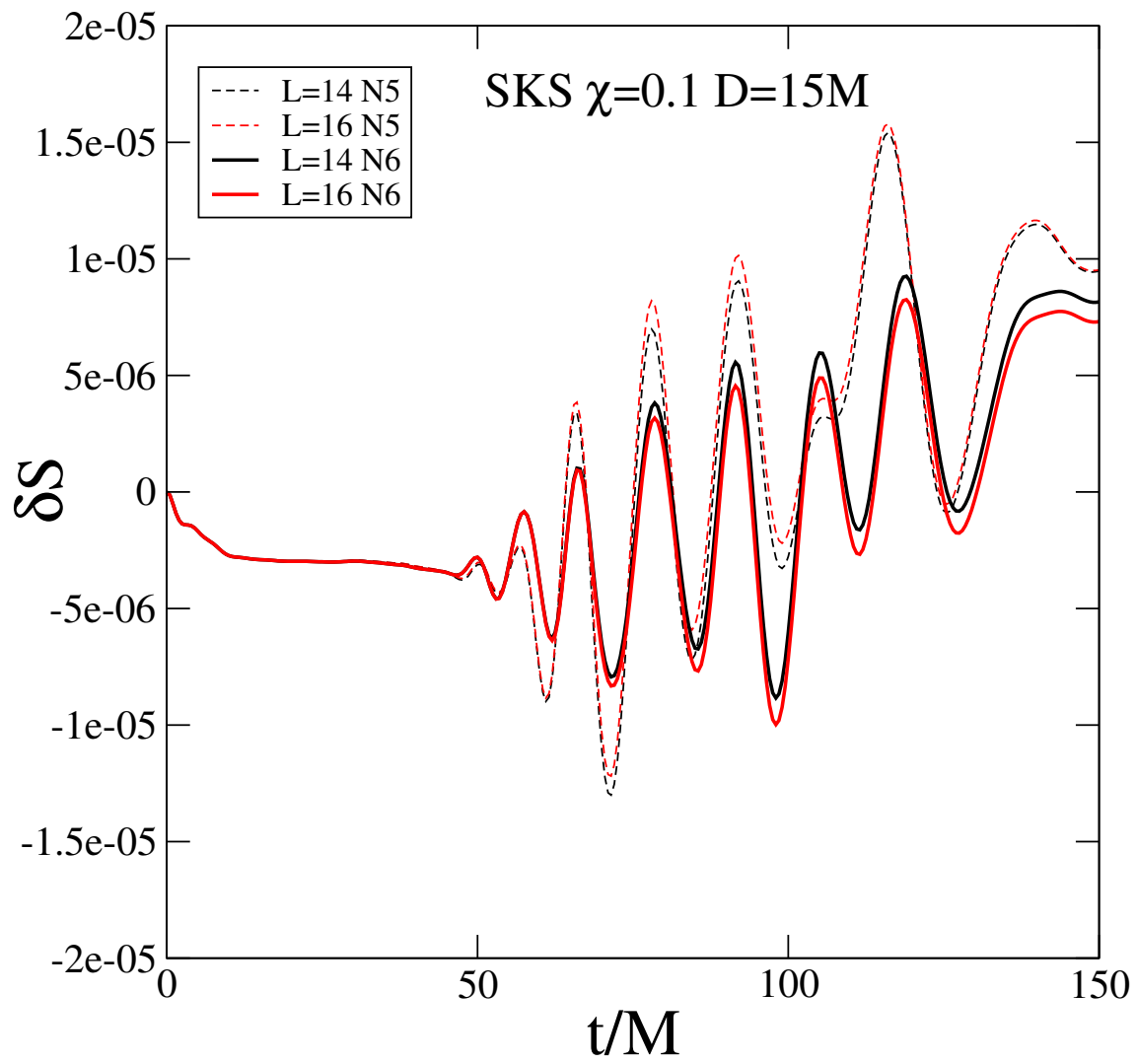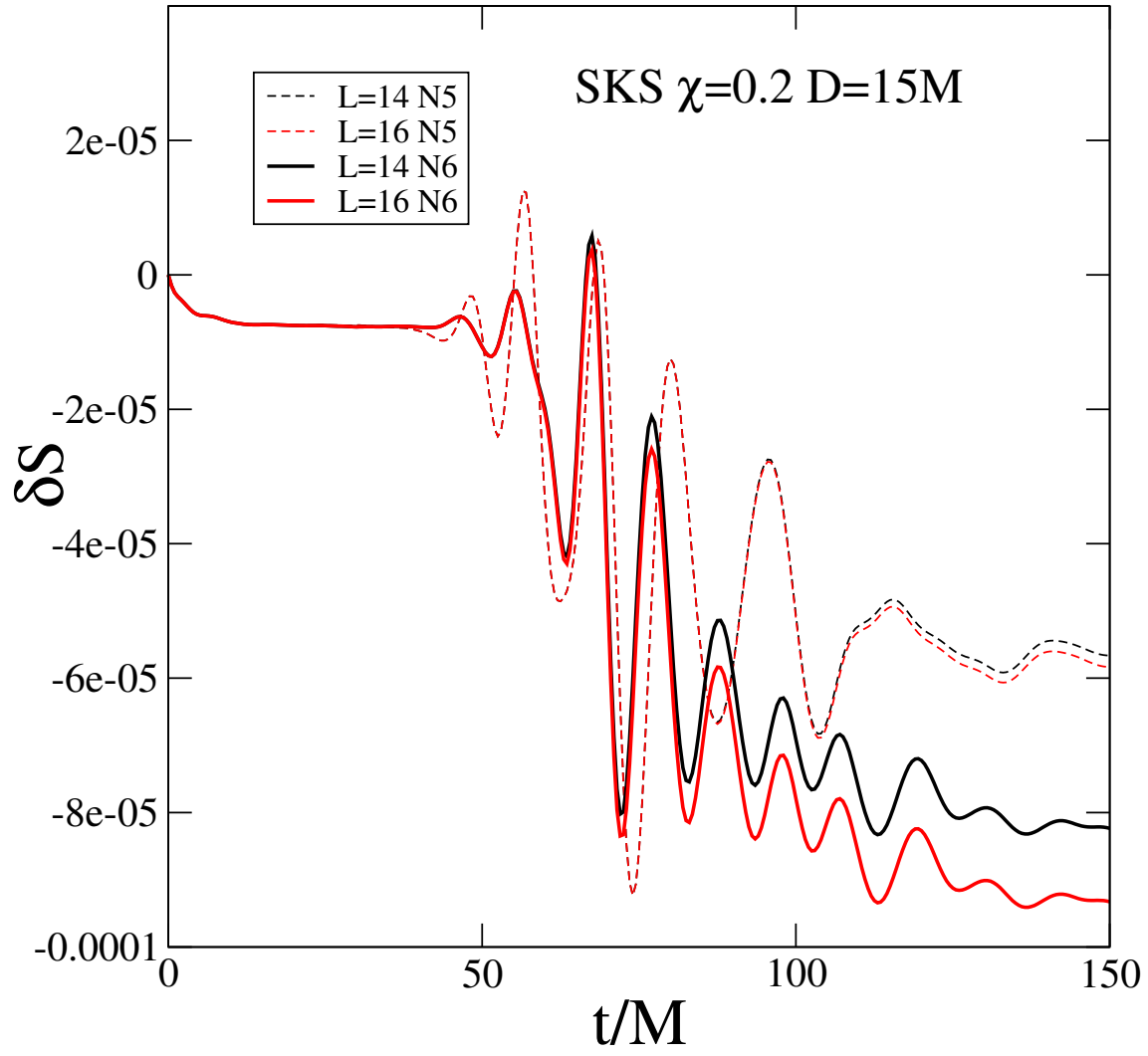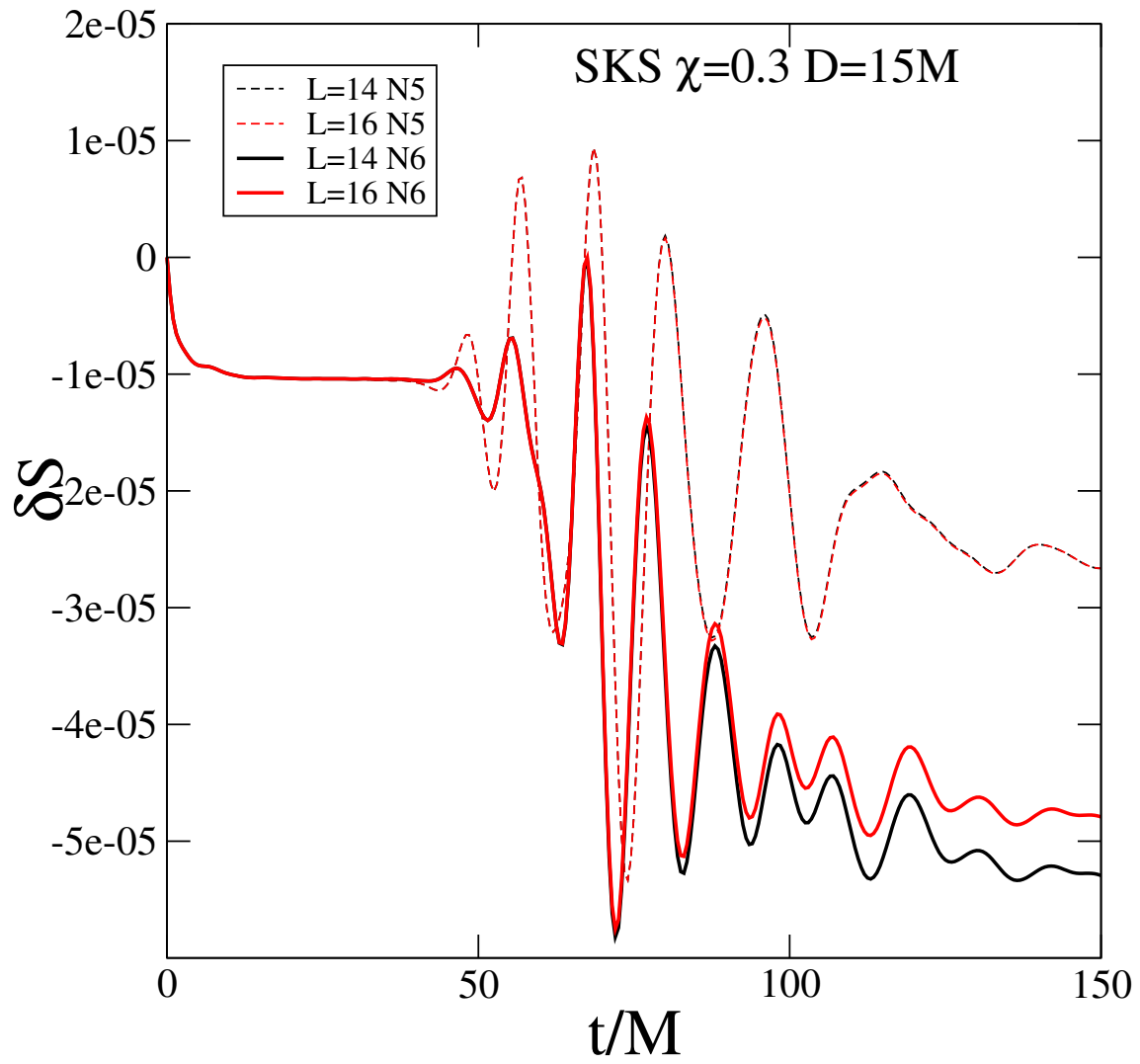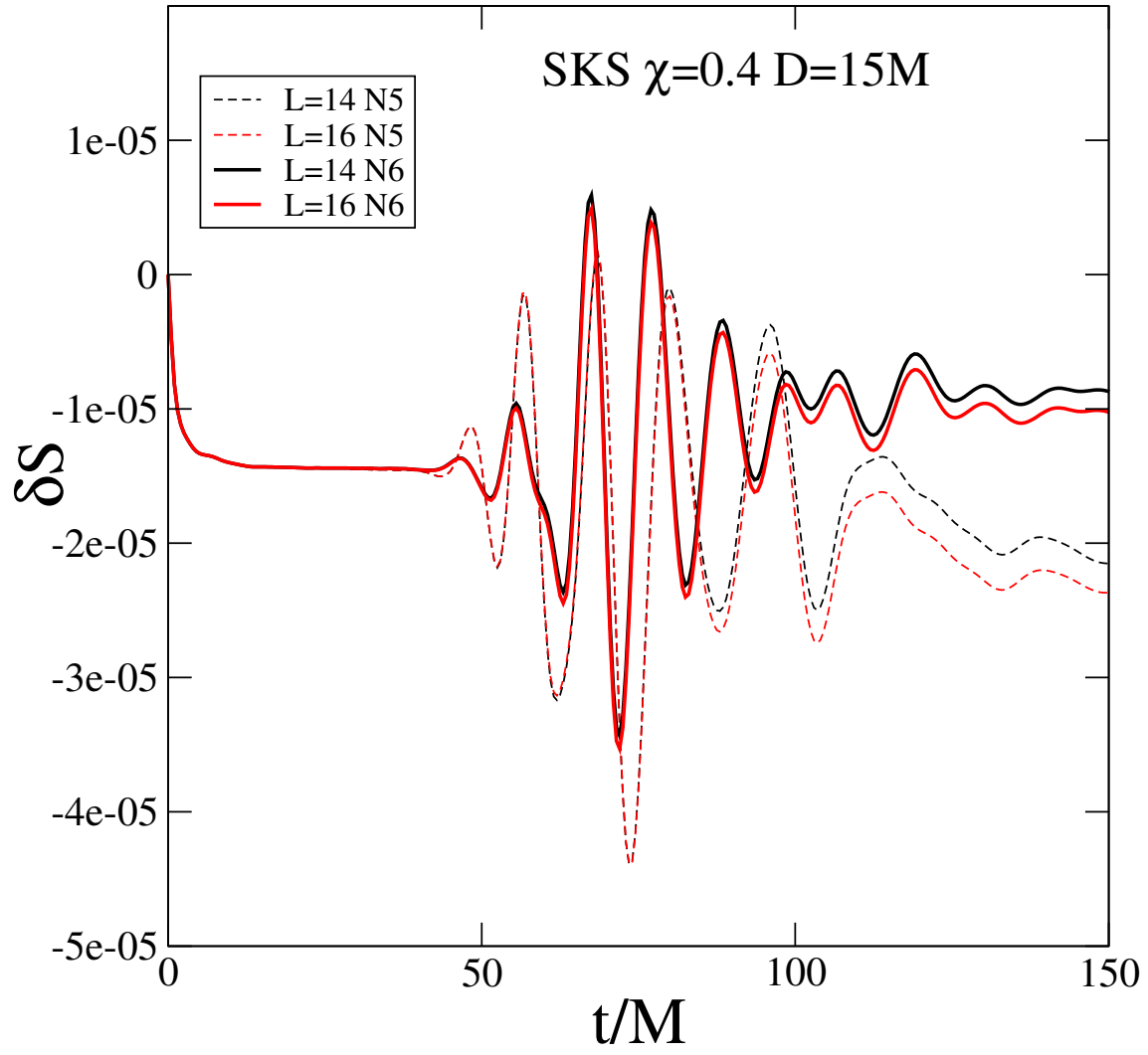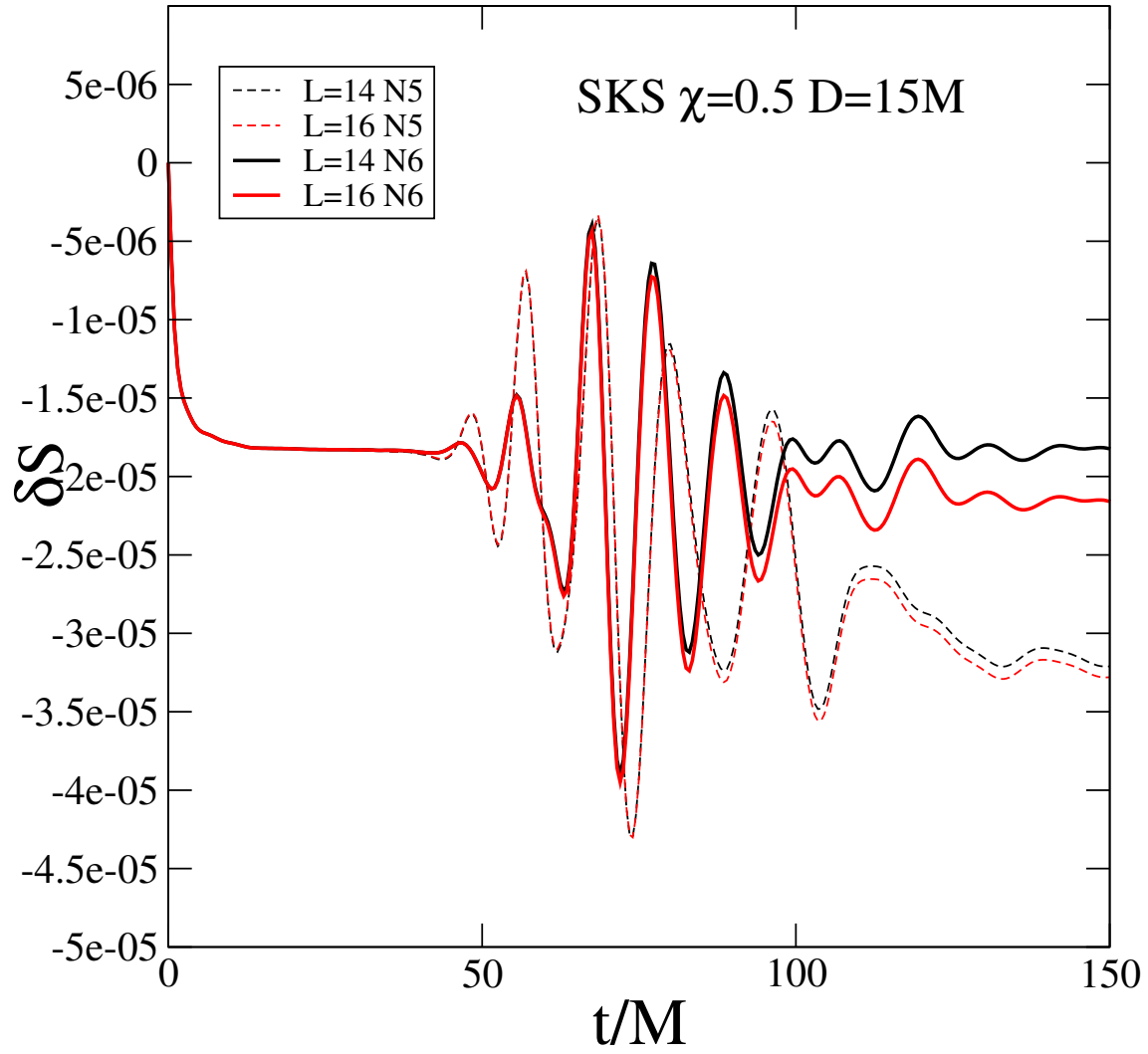
Figure 5.10: Convergence test of $\delta S(t)$ for CF initial data in the case $D = 15M$, $\chi = 0.3$. The top panel shows $\delta S(t)$ at different resolutions and the bottom panel shows the differences between consecutive resolutions
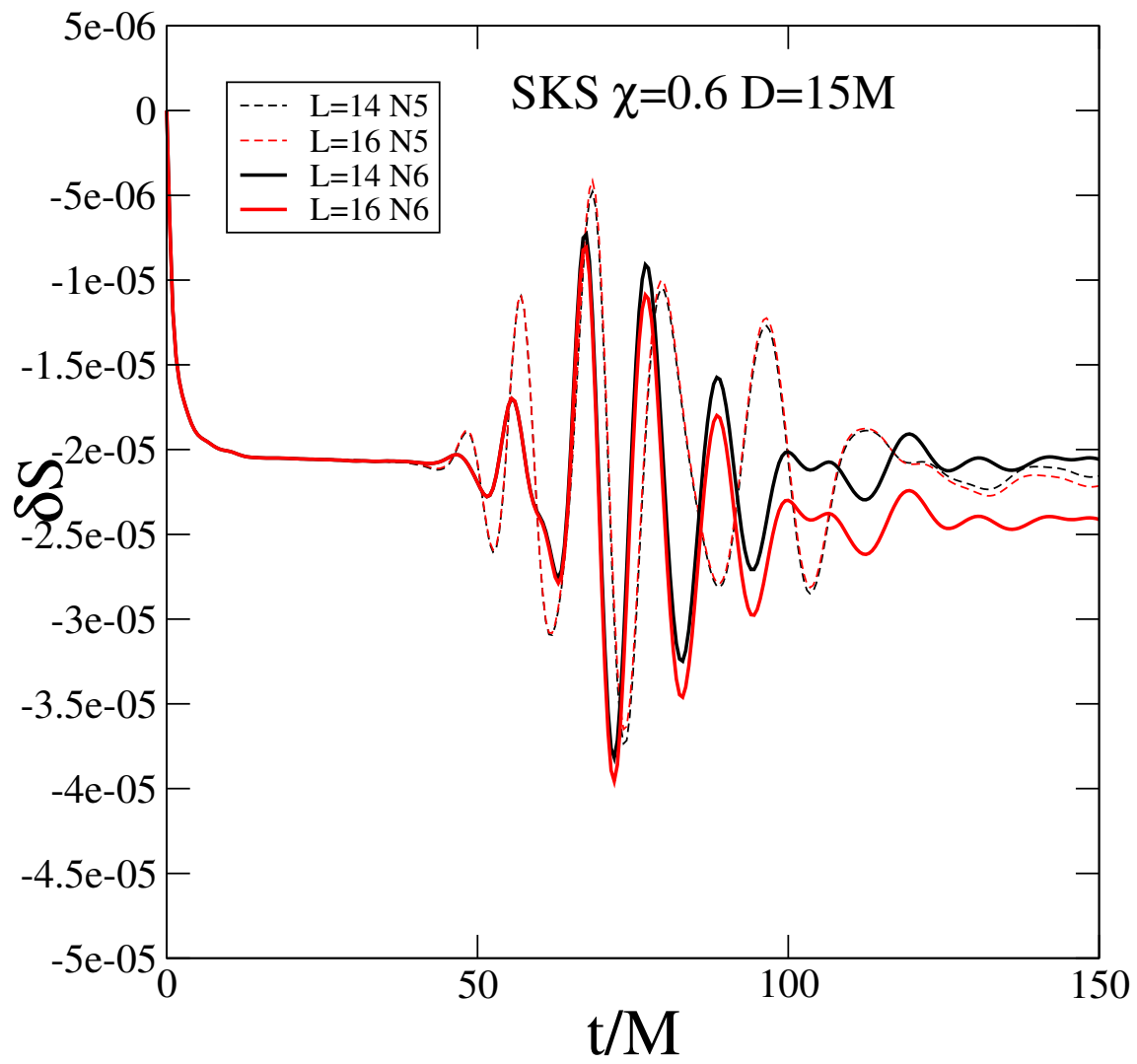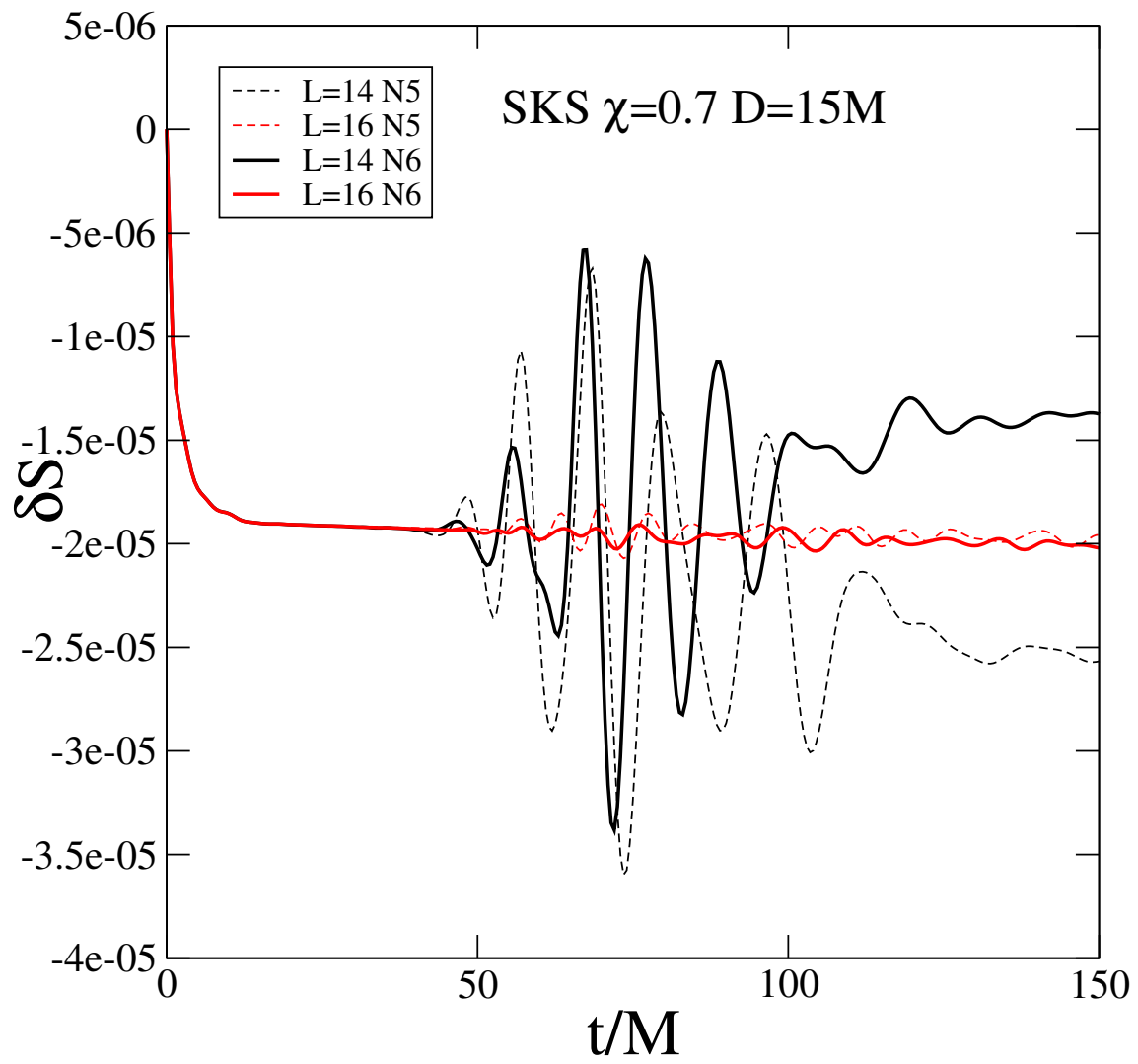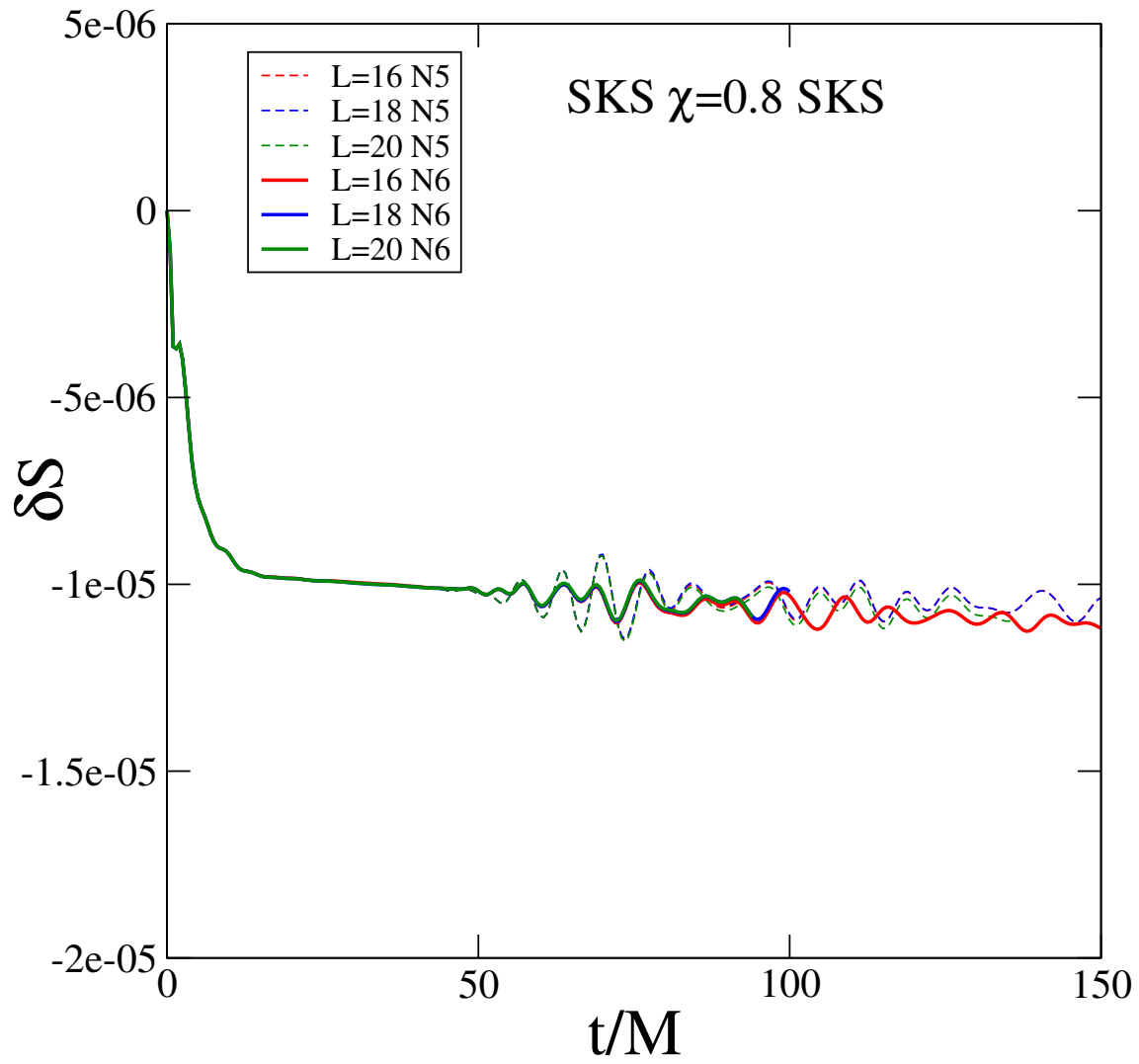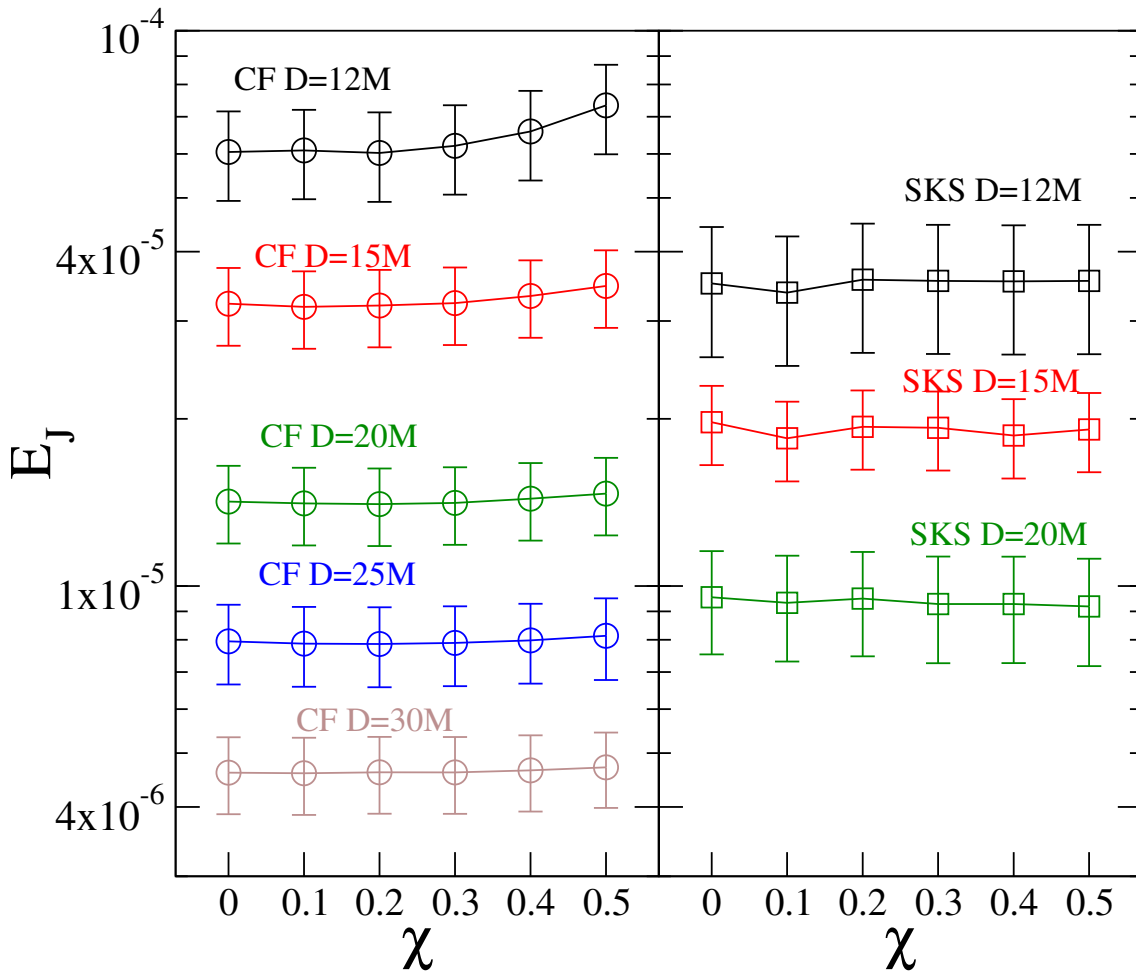
Figure 5.11: Energy in junk radiation as a function of χ at various initial separations, for conformally flat initial data (left panel) and SKS initial data (right panel). Within the uncertainty limit, there is virtually no dependence of E_J on χ
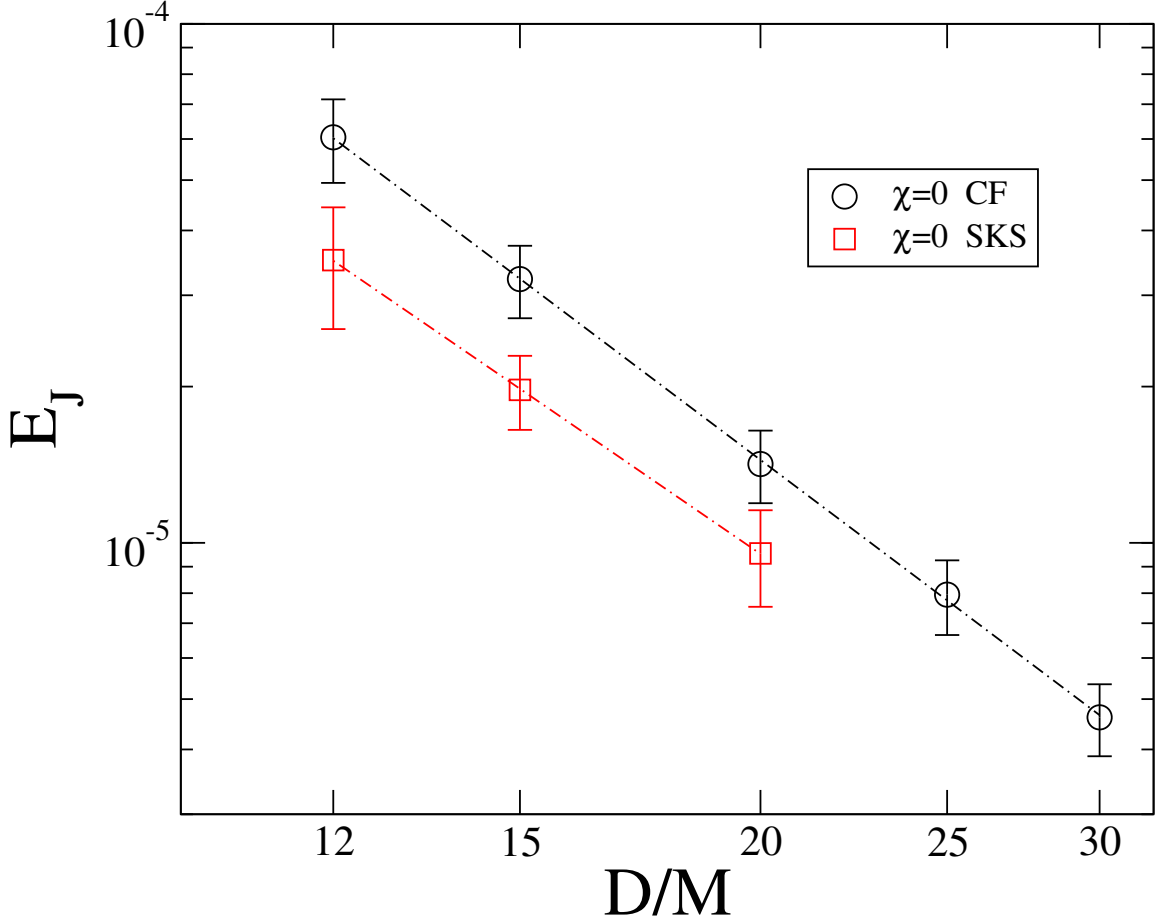
Figure 5.12: Log-log plot of the energy in junk radiation as a function of initial separation for binaries where $\chi = 0$. The black circles and red squares denote conformally flat and SKS initial data, respectively. The dotted lines are power law fits, with indices of ~ -2.79 and ~ -2.55 respectively.

shows E_J as a function of D for CF and SKS data. Both cases are good fits to power laws. For conformally flat data,

$$E_J^{\mathrm{CF}} \sim 0.06225 \left(\frac{D}{M} \right)^{-2.7933} .$$ (5.23)

and for SKS data

$$E_J^{\mathrm{SKS}} \sim 0.019576 \left(\frac{D}{M} \right)^{-2.5464} ,$$ (5.24)

however the latter is just a fit to three data points.

5.6.2   Mass Increase

As discussed earlier, we only attempt to quantify the transient quantities for CF data, due to the non-convergence of SKS data. We being by looking at the dependence of δM_{eq} on separation. In Fig. 5.13, we plot it for curves of constant χ[3].

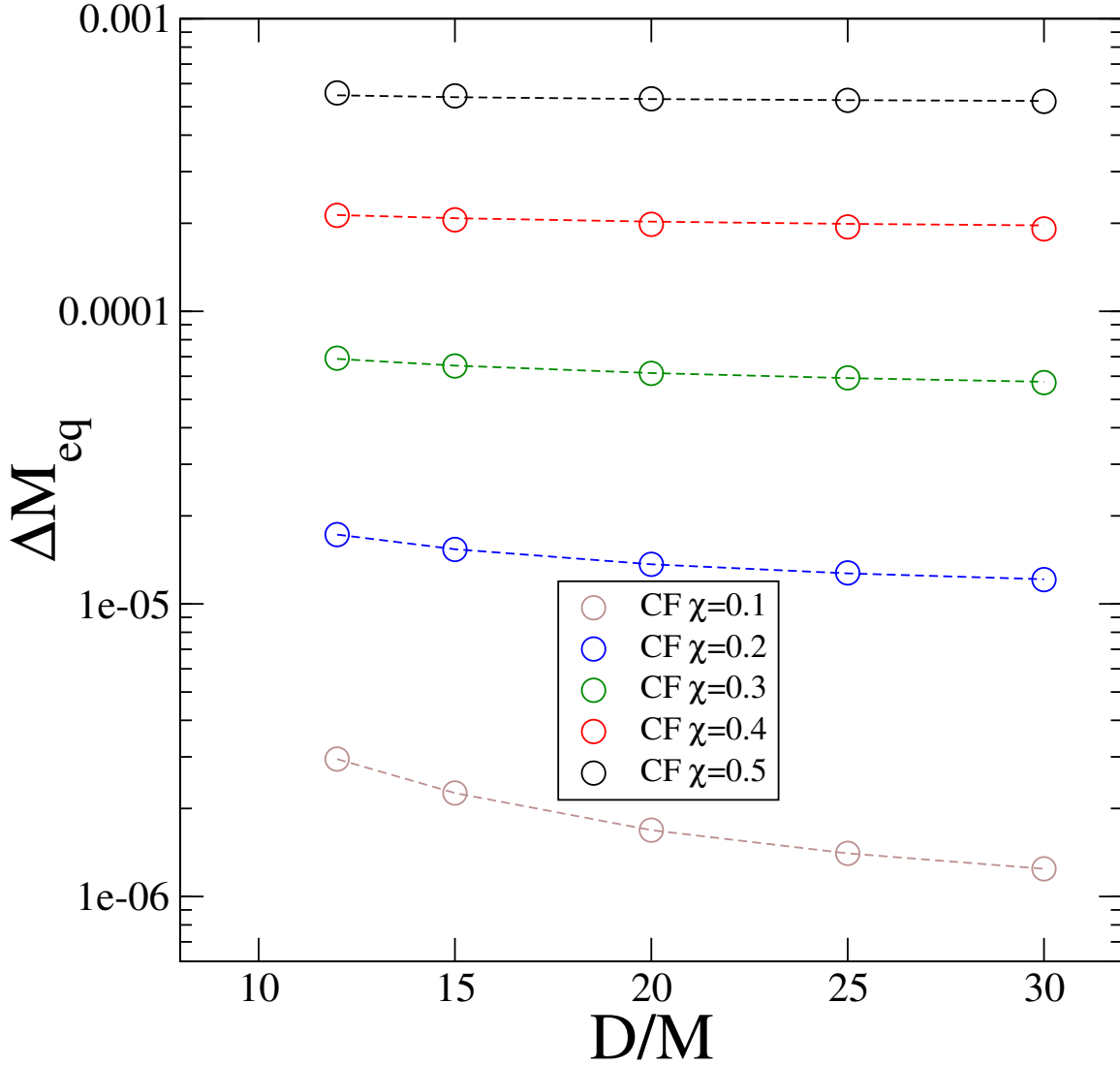Figure 5.13: $\delta M_{\rm eq}$ as a function of initial separation for CF initial data. The dotted lines are the best fits to a power law plus a constant offset.

The data are nearly independent of distance at high spin, while there is a clear

---

[3]we omit $\chi = 0$ because the data is too noisy

dependence at lower spin. In each case, we fit the data to a power law plus a constant offset. The fits are

$$\delta M_{\text{eq}}^{\chi=0.1} = 0.000170 \, (D/M)^{-1.76} + 8.194 \times 10^{-7}$$

$$\delta M_{\text{eq}}^{\chi=0.2} = 0.000209 \, (D/M)^{-1.36} + 1.007 \times 10^{-5}$$

$$\delta M_{\text{eq}}^{\chi=0.3} = 0.000146 \, (D/M)^{-0.75} + 4.60 \times 10^{-5}$$

$$\delta M_{\text{eq}}^{\chi=0.4} = 0.000262 \, (D/M)^{-0.87} + 1.83 \times 10^{-4}$$

$$\delta M_{\text{eq}}^{\chi=0.5} = 0.000470 \, (D/M)^{-0.99} + 5.08 \times 10^{-4}$$

In Fig. 5.14, the dependence of δM_{eq} is shown. In general we find that δM_{eq} grows rapidly with χ and the dependence is nearly exponential at each separation.

5.6.3 Spin Decrease

As with the mass increase, we only attempt to calculate δS_{eq} for CF data, as it was found to not be convergent for SKS data. In Fig. 5.15 we plot δS_{eq} vs. D for curves of constant χ^4. The data are similar to those in Fig. 5.13, although there is a stronger dependence on separation.

In each case, we fit the data to a power law plus a constant offset. The fits are

$$\delta S_{\text{eq}}^{\chi=0.2} = 0.000154 \, (D/M)^{-.966} + 5.836 \times 10^{-8}$$

$$\delta S_{\text{eq}}^{\chi=0.3} = 0.000340 \, (D/M)^{-0.836} + 6.025 \times 10^{-6}$$

$$\delta S_{\text{eq}}^{\chi=0.4} = 0.00136 \, (D/M)^{-1.189} + 8.348 \times 10^{-5}$$

$$\delta S_{\text{eq}}^{\chi=0.5} = 0.00261 \, (D/M)^{-1.133} + 3.445 \times 10^{-4}$$

In figure 5.16, δS_{eq} is plotted as a function of χ, at different separations. In each case, the data is a good fit to an exponential; at $D = 15M$,

$$\delta S_{\text{eq}} \sim 1.563 \times 10^{-6} e^{11.546\chi} \tag{5.25}$$

---

[4]we omit $\chi = 0$ because δS_{eq} is not well-defined, and we omit $\chi = 0.1$ because the data is too noisy
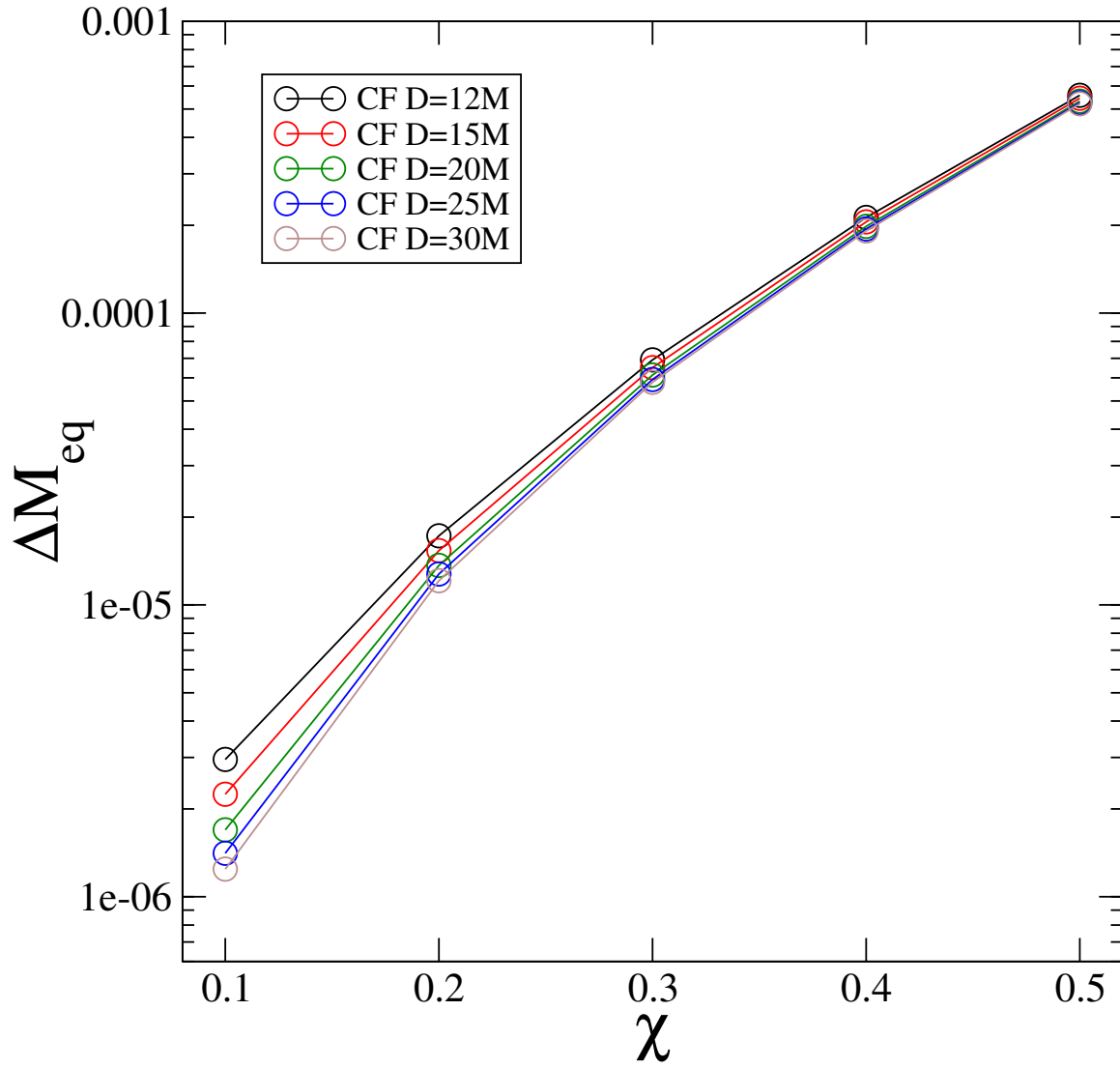
Figure 5.14: δM_{eq} as a function of black hole spin χ for CF initial data, evaluated at each different initial separation.

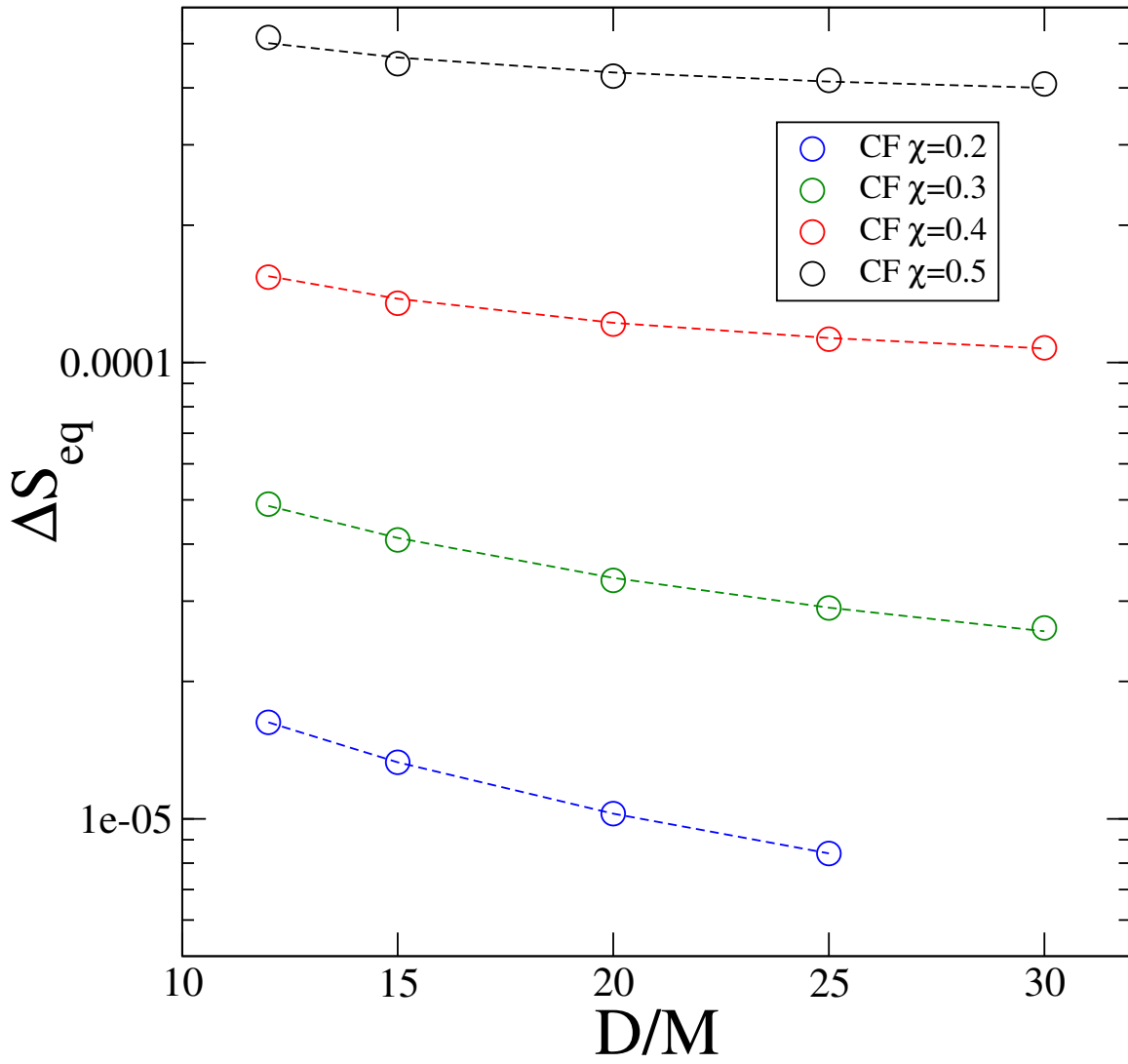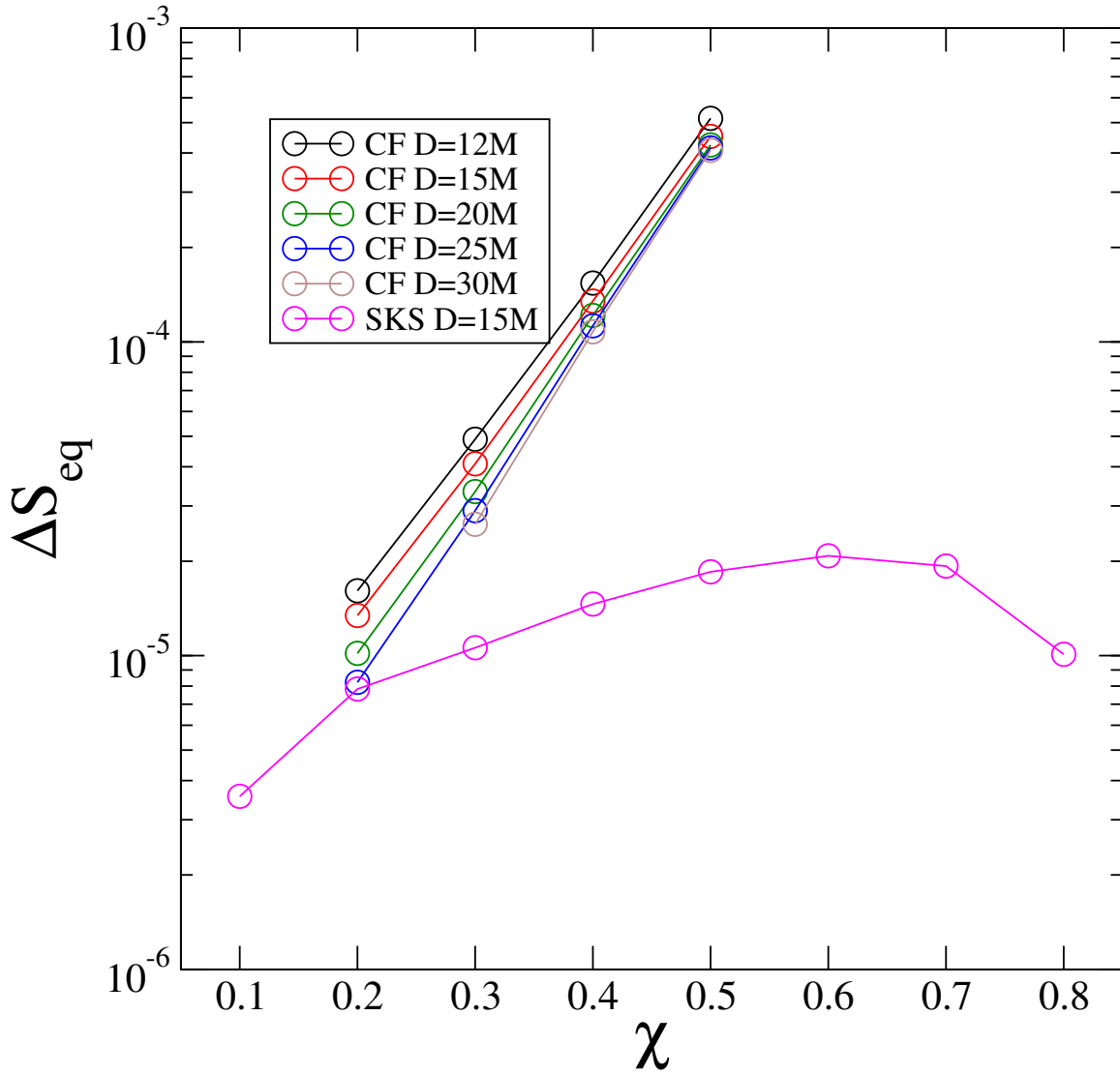Figure 5.15: δS_{eq} vs. D for CF initial data. The dotted curves are the best fit power law plus constant offsets.

Figure 5.16: Semi-log plot of δS_{eq} as a function of χ for CF data. The dotted lines are the best fit exponentials.

5.7   Summary

My Summary.

Chapter 6

Improved Initial Data for Spinning Binary Neutron Stars

6.1 Chapter Overview

This is a set of notes regarding a bug found the code we use to generate initial data for spinning binary neutron stars.

6.2 Introduction

Recently, Tacik et al. (2015) presented results for the construction and evolution of binary neutron stars with arbirary spin vectors using the SpEC code. In this chapter, we will revisit those results. Namely we have found a computational error in the code that was used to generate those results. We will begin by discussing what the error was and what the general implications of that are. We will then revisit and update the results of Tacik et al. (2015) in lieu of this. Finally, we will then discuss how the results of Tacik et al. (2015) can be pushed even further.

6.3   Erroneuous code

```
Dm b1(sd,0.0);

for (int i=0;i<3;i++){

  b1 += Shift(i)*moddPot(i);

}

b1 = sqr(b1 + CEuler);


Dm b2(sd,0.0);

for (int i=0;i<3;i++){

  for (int j=0;j<3;j++){

    b2 += Invg(i,j)/(sqr(sqr(Psi)))*(moddPot(i)+Rot(i))*Rot(j);

  }

}


Dm H = sqr(b1) + 2*b1*b2;

H = sqrt(H);

H += (b1+b2);

H = H / (2*sqr(Lapse));


for (int i =0; i <3; i++){

  for (int j=0; j<3; j++){

    H -= Invg(i,j) / (sqr(sqr(Psi))) * (moddPot(i)) * (moddPot(j));

  }

}

H = sqrt(H);
```

6.4   Revised Code

```
Dm b1(sd,0.0);

for (int i=0; i<3; i++){

  b1 += Shift(i)*moddPot(i);

}

b1 = sqr(b1 + CEuler);


Dm b2(sd,0.0);

for (int i=0; i<3; i++){

  for (int j=0; j<3; j++){

    b2 += Invg(i,j) / (sqr(sqr(Psi))) * (moddPot(i)+Rot(i)) * Rot(j);

  }

}

b2 *= (2 * Lapse * Lapse);


Dm L2(sd, 0.0);

L2 = ((b1+b2) + sqrt(sqr(b1)+2*b1*b2))/(2*sqr(Lapse));


Dm H = L2;

for (int i=0; i <3; i++){

  for (int j=0; j<3; j++){

    H -= Invg(i,j)/(sqr(sqr(Psi))) * (moddPot(i)+Rot(i))*(moddPot(j)+Rot(j));

  }

}

H = sqrt(H);
```

6.5   Description of Bug

Following Tichy (2012), the 3-velocity of the neutron star fluid in an inspiralling binary is written as the sum of an irrotational part and a rotational part:

$$U^i = \frac{\Psi^{-4}\tilde{\gamma}^{ij}}{h\gamma_n}\left(\partial_j\phi + W_j\right).$$

(6.1)

Here Ψ is the conformal factor, $\tilde{\gamma}_{ij}$ is the conformal metric, h is the specific enthalpy, γ_n is the Lorentz term $\gamma_n = \left(1 - \gamma_{ij}U^iU^j\right)^{-1/2}$, ϕ is the irrotational velocity potential, and W is the rotation term, designed to endow a uniform rotation to the star. In this construction, the solution of the Euler equation is

$$h = \sqrt{L^2 - \left(\nabla_i\phi + W_i\right)\left(\nabla^i\phi + W^i\right)}$$

(6.2)

where

$$L^2 = \frac{(x + y) + \sqrt{x^2 + 2xy}}{2\alpha^2}$$

(6.3)

$$x = \left(\beta^i\nabla_i\phi + C\right)^2$$

(6.4)

$$y = 2\alpha^2\left(\nabla_i + W_i\right)W^i$$

(6.5)

However, our code indicates that we have computed the following quantity instead

$$h' = \sqrt{L^2 - \left(\nabla_i\phi\right)\left(\nabla^i\phi\right)}$$

(6.6)

where

$$y' = \left(\nabla_i\phi + W_i\right)W^i$$

(6.7)

The difference between the two quantities is

$$h'^2 - h^2 = \frac{(y' - y)}{2\alpha^2} + \frac{\sqrt{x^2 + 2xy} - \sqrt{x^2 + 2xy'}}{2\alpha^2} - W_iW^i - \nabla_i\phi\left(\nabla^i\phi + W^i\right)$$

(6.8)

Let's take a rough limit where W is very large and only consider terms of order W^2. Then this difference is

$$h'^2 - h^2 = \frac{W^2 \left(1 - 4\alpha^2\right)}{2\alpha^2} \tag{6.9}$$

Since α should generally be > 0.5, this will be a negative number. This means that the enthalpy was too low, which means the density was too low, which means it wants to increase. This is what is seen in our simulations.

6.6 Revisiting previous results

Having re-coded the erroneous code, we now revisit the results of Tacik et al. (2015).

6.6.1 Size of density oscillations

We constructed initial data with the same input files as for the S0.4z run of Tacik et al. (2015), and evolved it with the same input files as well, for about $2500M_\odot$. In figure 6.1 we plot the normalized density oscillations ($\rho/\rho(t = 0)$, where ρ represents the maximum density) for both cases. We see that previously the peak-to-peak density oscillations were about 20%, whereas now they are about 0.5%, a decrease by about a factor of 40. This is in line with what is seen in simulations of non-spinning binary neutron stars (R. Hass, Priv. comm). The period of oscillation remains the same as it was previously, indicating that it probably still represents an excited quasi-normal mode oscillation. We note now, however, that the phase of oscillation has changed by approximately half of a period.

6.6.2 Magnitude of spin

With a change in the computation of the enthalpy, and thus distribution of the equilibrium enthalpy, the spin of the star may change. In particular, in the old bugged code, the starting radius of the star was too large (the density too small) and the oscillations would begin. Since $\chi \propto R^2$, we would expect that the dimensionless spin show be higher
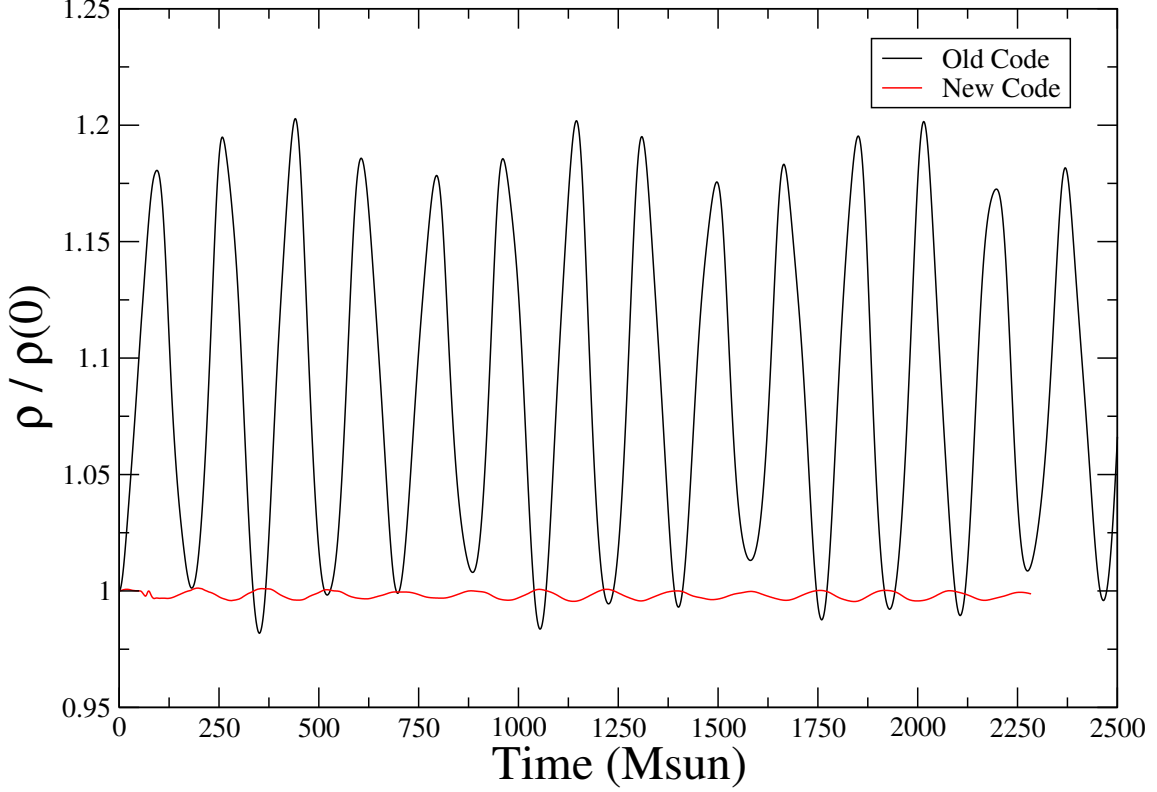
Figure 6.1: Normalized density oscillations for the S0.4z run from Tacik et al. (2015) and from a new run with the same parameters.

in the old code. In figure 6.2 we plot the spin during the evolution, measured in the way described in Tacik et al. (2015), for the new and old codes. Indeed we see that dimensionless spin has descreased from ~ 0.375 to ~ 0.33. Similar to the case of the density oscillations, the spin oscillations are still present in the new code, but they are much lower in magnitude and are half a period out of phase with the previous data.

6.6.3 $\chi - \Omega$ relation

As we have just seen, the new computation of the enthalpy means that the $\chi(\Omega)$ relation is changed. Thus we will now re-visit Fig. 8 of Tacik et al. (2015) where χ is plotted as a function of Ω. First, we re-compute all the initial data sets as before with the same values of Ω. However, because our computation is now more robust, we are also able to
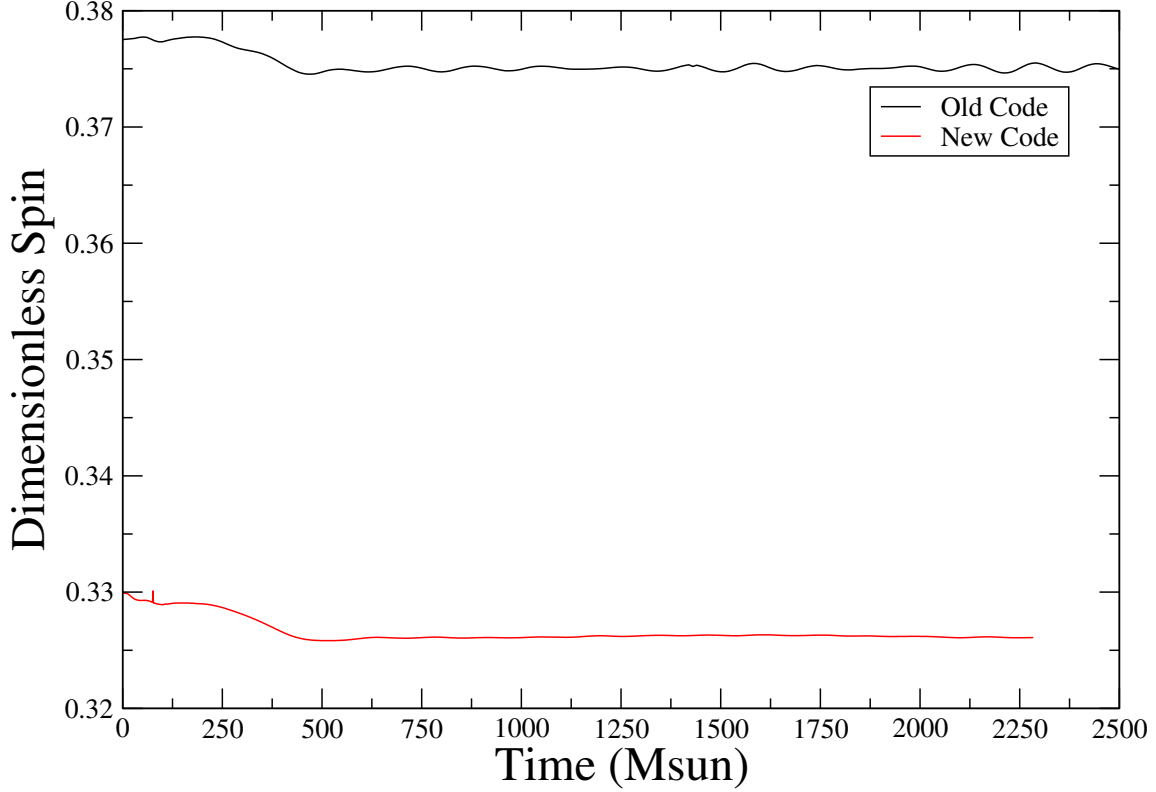
Figure 6.2: Dimensionless spin, $\chi = \frac{J}{M^2_{\mathrm{ADM}}}$, measured during the evolution of the S0.4z run from Tacik et al. (2015) with the old code and the new code.

extend to much higher values of Ω than before. Therefore, we also use this plot to explore how much higher the initial data solver can be pushed. The new relation is shown in figure 6.3. First, we note that the $\chi(\Omega)$ relation is unchanged at low values of Ω. In Tacik et al. (2015), a value of $|\Omega| = 0.00273$ was used for the S-0.05z run - so it is probably unaffected significantly by this bug. Second, we note that the new curve is indeed below the old curve, as predicted above. Finally, we note that the initial data solver can indeed be pushed much further now. Before it was able to reach spins of ~ 0.43, and now it can reach spins of ~ 0.63 - quite a significant increase. This 0.63 is in fact above the theoretical 0.57 limit quoted in Ansorg et al. (2003), and more in line with the values from studies like Lo & Lin (2011). Clearly this invites further investigation.
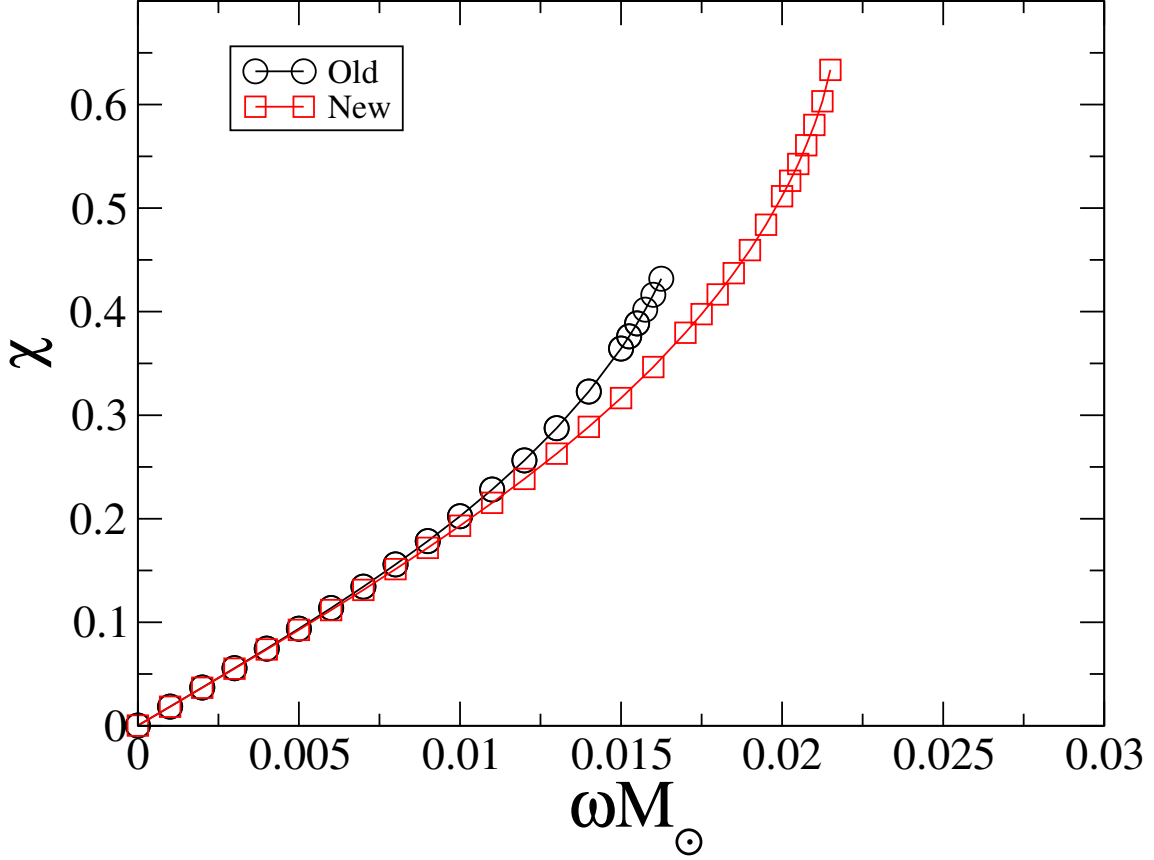
Figure 6.3: χ as a function of Ω in the initial data. The black curve is from Fig. 8 of Tacik et al. (2015), while the red curve is generated with the bug fixed.

6.6.4 Initial Data Convergence

We'll know look at how the changed enthalpy computation affects the convergence of the initial data. Again, we focus on the S0.4z run from Tacik et al. (2015) using the same input files. In figure 6.4 we look at the Hamiltonian and Momentum constraints for the new code. We do not find a very significant difference between the two. Presumably this is because many there are many factors that affect the constraints. Furthermore, we were previously still solving the field equations correctly, it just happened to be for a star that was out of equilirbium.

Next, we look at how the global quantities E_{ADM} and J_{ADM} are affected by this computational change. This is plotted in Fig. 6.5. In particular we are plotting the
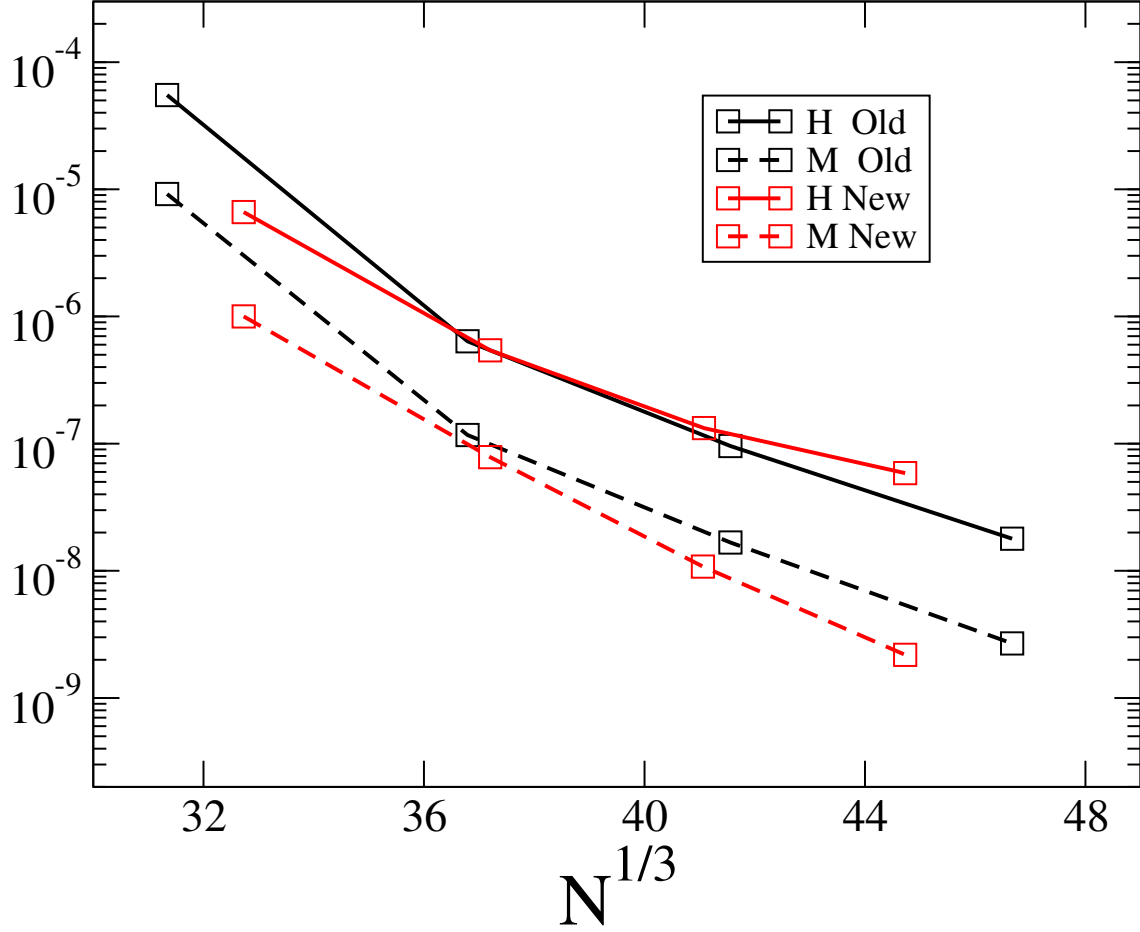
Figure 6.4: Hamiltonian and Momentum constraints for the new and old code, for the S0.4z run.

fractional difference between adjacent resolutions as a function of the lower resolution. The "old"' data is from Fig.5 of Tacik et al. (2015). Again, there does not seem to be a large change here (although the E_{ADM} slope for the new initial data is much more shallow and the data start much lower at low resolution.

Next, we look how the spin in the initial data convergences with resolution. This is plotted in figure 6.6. In particular we plot the absolute difference between $\chi(N)$ and χ at the highest resolution. The "old" data is from Fig. 6 of Tacik et al. (2015). The new data seems to be lower than the old data by a fairly significant amount.
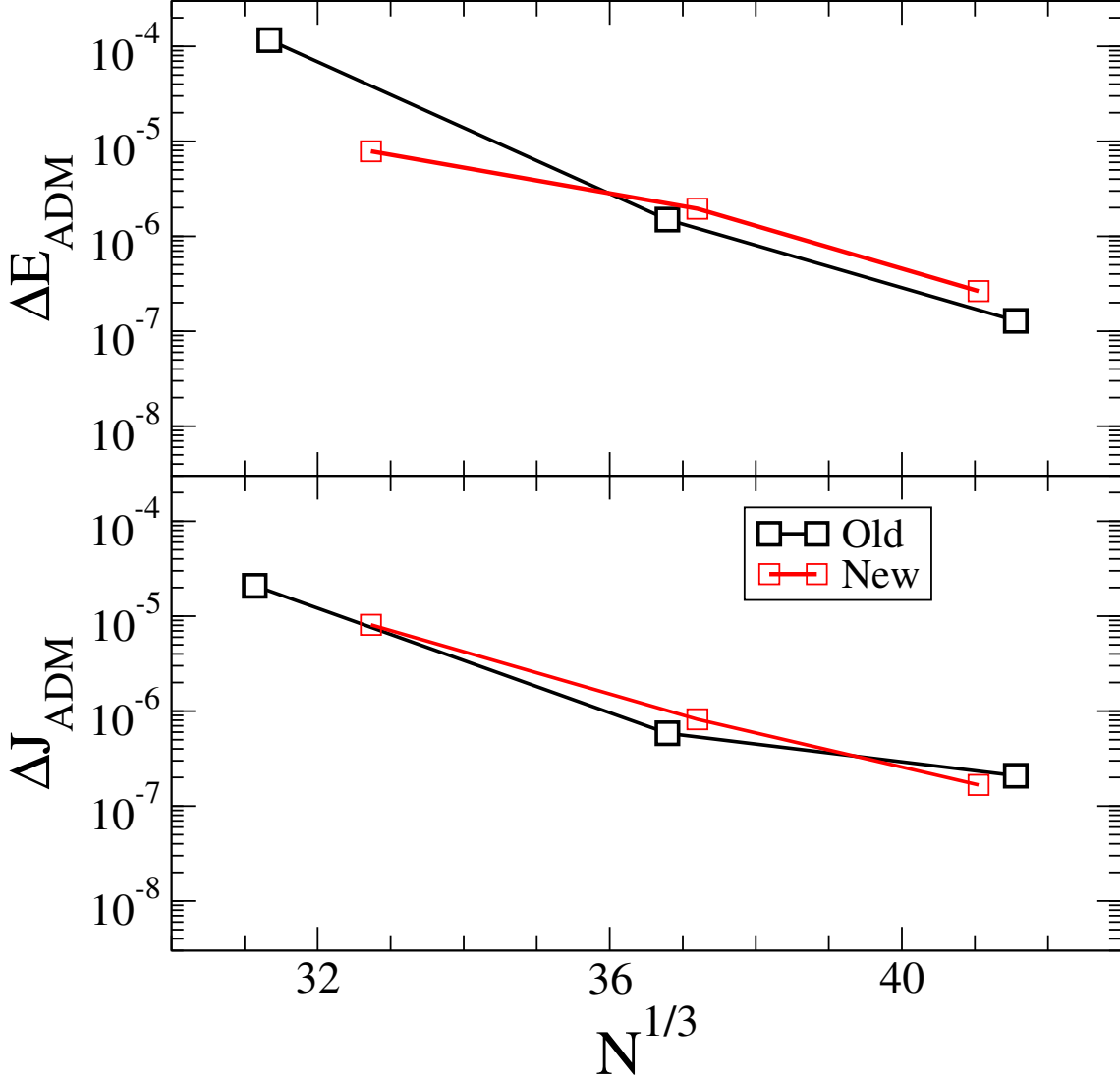
Figure 6.5: Fractional convergence of the ADM energy and ADM angular momentum for the new and old codes.

6.6.5 Komar Mass

As noted in Foucart et al. (2008), the difference between the Komar mass M_K and the ADM energy M_{ADM} is an indicator of deviations from equilibrium. We now suspect our neutron star is more close to being in equilibirum, and therefore except that this difference would be smaller. Let us investigate this. We again look at the same S0.4z comparison. In the old results, at the highest initial data resolution, this difference
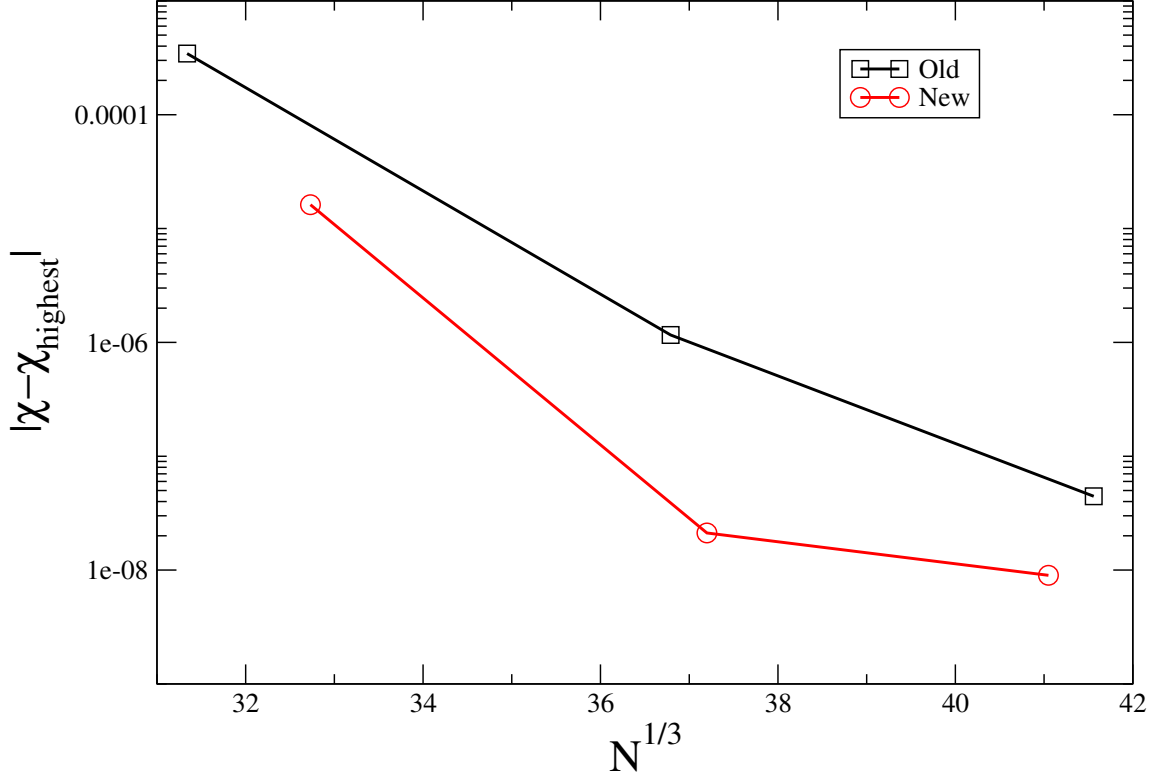
Figure 6.6: Convergence of the spin measured in the initial data for the new and old codes.

is $|(M_K - M_{\mathrm{ADM}})/M_k \sim 2.6 \times 10^{-3}$. In the new results, this difference is $|(M_K - M_{\mathrm{ADM}})/M_k \sim 2.1 \times 10^{-4}$. So indeed, this difference has decreased by more than an order of magnitude.

6.7 Higher Spin Evolutions

As shown in Fig. 6.3, the initial data solver can now construct initial data for much higher spins than before. Let us try to evolve some of these.

6.7.1 Evolution 1

Here we construct and evolve initial data with $\Omega = 0.019\hat{z}$. In figure 6.7 we present a snapshot of the run, plotting the normalized density oscillations, measured spin, and the orbit of the stars. The dimensionless spin is about $\chi \sim 0.46$. The peak-to-peak density

oscillations are now about 2%. Higher than in the previous evolution, but still much smaller than in Tacik et al. (2015). We have performed about three orbits of evolution.
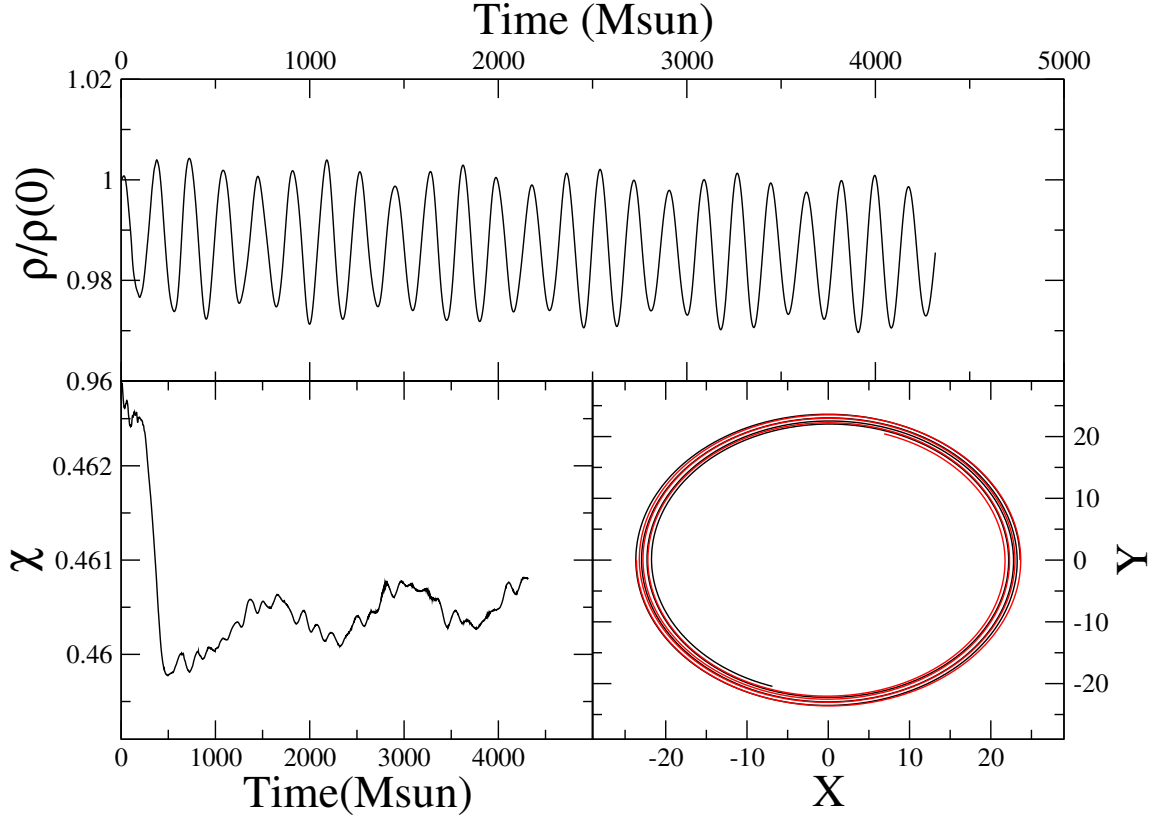

Figure 6.7:   A snapshot of an evolution with $\Omega = 0.019$. The top panel shows the normalized density oscillations. The bottom-left panel shows the measured spin of a star. The bottom-right panel shows the orbtis of the stars as they inspiral.

6.7.2   Evolution 2

Here we construct and evolve initial data with $\Omega = 0.0215\hat{z}$. The evolution has only recently begun so we can only make tentative conclusions. But the peak-to-peak density oscillations are around 6%, and the spin during the evolution is around $\chi \sim 0.625$. See Fig. 6.8.

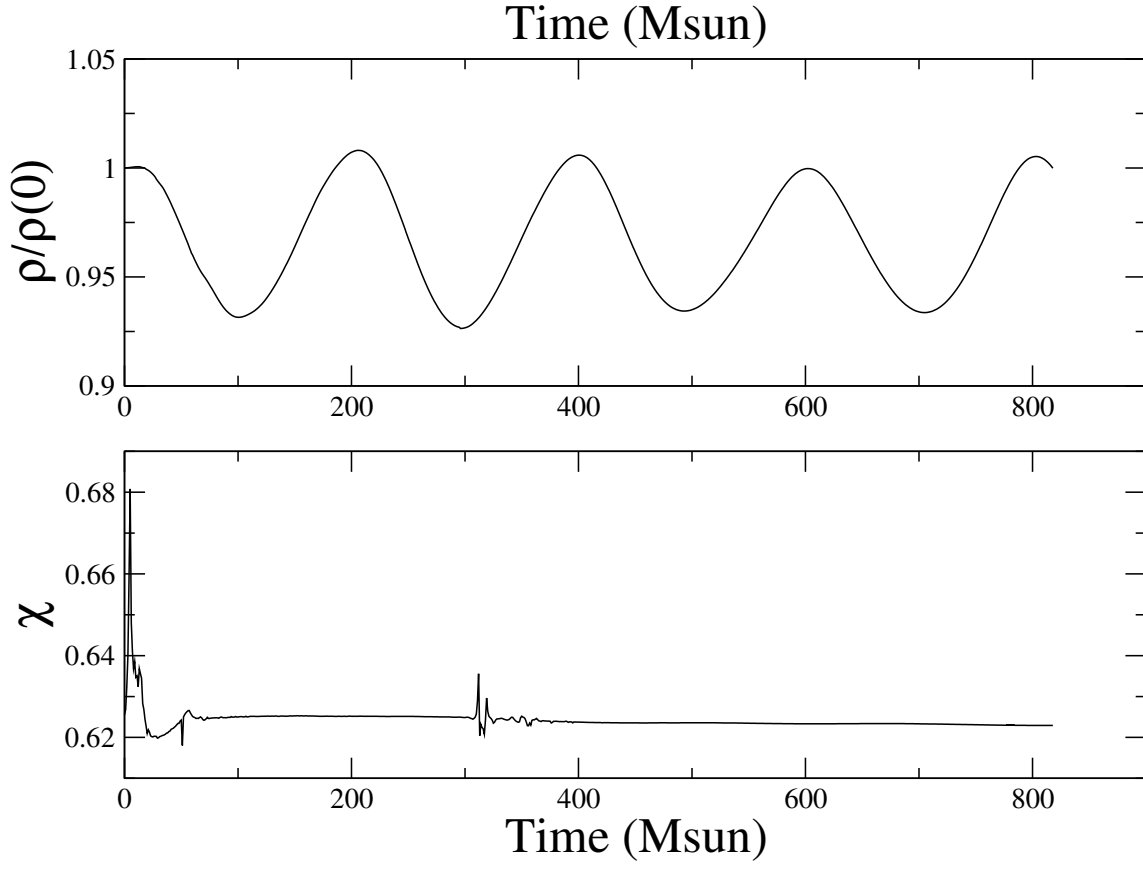Figure 6.8: Density oscillations and and measured spin for evolution 2. This run has only recently begun.

Chapter 7

Conclusions & Future Work

7.1 Conclusions

My Conclusions

7.2 Future Work and Directions

My Future Work and Directions.

Bibliography

????, http://www.black-holes.org/SpEC.html

A. Harten, P. D. Lax, B. v. L. 1983, SIAM Rev., 25, 35

Aasi, J., et al. 2015, Class. Quant. Grav., 32, 074001

Abadie, J., et al. 2010, Class. Quant. Grav., 27, 173001

Acernese, F., et al. 2006, Class. Quantum Grav., 23, S635

—. 2015, Class.Quant.Grav., 32, 024001

Agathos, M., Meidan, J., Pozzo, W. D., Li, T. G. F., Tompitak, M., Veitch, J., Vitale, S., & Broeck, C. V. D. 2015, ArXiv:1503.05405

Ansorg, M., Kleinwachter, A., & Meinel, R. 2003, Astron.Astrophys., 405, 711

Arnowitt, R., Deser, S., & Misner, C. W. 1962, in Gravitation: An Introduction to Current Research, ed. L. Witten (New York: Wiley), 227–265

Ashtekar, A., Beetle, C., & Lewandowski, J. 2001, Phys. Rev. D, 64, 044016

Ashtekar, A., & Krishnan, B. 2003, Phys. Rev. D, 68, 104030

Baiotti, L., Damour, T., Giacomazzo, B., Nagar, A., & Rezzolla, L. 2010, Phys. Rev. Lett., 105, 261101

Baiotti, L., Damour, T., Giacomazzo, B., Nagar, A., & Rezzolla, L. 2011, Phys. Rev. D, 84, 024017

Barish, B. C., & Weiss, R. 1999, Phys. Today, 52, 44

Baumgarte, T. W., O'Murchadha, N., & Pfeiffer, H. P. 2007, Phys. Rev. D, 75, 044009

Baumgarte, T. W., & Shapiro, S. L. 2009, Phys.Rev., D80, 064009

Benacquista, M. J., & Downing, J. M. 2013, Living Rev.Rel., 16, 4

Bernuzzi, S., Dietrich, T., Tichy, W., & Bruegmann, B. 2014, Phys. Rev. D, 89, 104021

Bernuzzi, S., Nagar, A., Dietrich, T., & Damour, T. 2015, Phys.Rev.Lett., 114, 161103

Berti, E., et al. 2015

Bildsten, L., & Cutler, C. 1992, Astrophys. J., 400, 175

Blanchet, L. 2006, Living Rev.Rel., 9, 4

Bode, T., Shoemaker, D., Herrmann, F., & Hinder, I. 2008, Phys. Rev. D, 77, 44027

Boyle, M., Brown, D. A., Kidder, L. E., Mroué, A. H., Pfeiffer, H. P., Scheel, M. A., Cook, G. B., & Teukolsky, S. A. 2007, Phys. Rev. D, 76, 124038

Boyle, M., Buonanno, A., Kidder, L. E., Mroué, A. H., Pan, Y., et al. 2008, Phys. Rev. D, 78, 104020

Brown, D. A., Harry, I., Lundgren, A., & Nitz, A. H. 2012, Phys.Rev., D86, 084017

Brown, J. D., & York, J. W. 1993, Phys. Rev. D, 47, 1407

Buchman, L. T., Pfeiffer, H. P., Scheel, M. A., & Szilágyi, B. 2012, Phys. Rev. D, 86, 084033

Buonanno, A. 2007, in Les Houches Summer School - Session 86: Particle Physics and Cosmology: The Fabric of Spacetime Les Houches, France, July 31-August 25, 2006

Buonanno, A., & Damour, T. 1999, Phys. Rev. D, 59, 084006

Buonanno, A., Kidder, L. E., Mroué, A. H., Pfeiffer, H. P., & Taracchini, A. 2011, Phys. Rev. D, 83, 104034

Caudill, M., Cook, G. B., Grigsby, J. D., & Pfeiffer, H. P. 2006, Phys. Rev. D, 74, 064011

Chatziioannou, K., Yagi, K., Klein, A., Cornish, N., & Yunes, N. 2015

Christodoulou, D. 1970, Phys. Rev. Lett., 25, 1596

Chu, T., Pfeiffer, H. P., & Scheel, M. A. 2009, Phys. Rev. D, 80, 124051

Cook, G. B. 2002, Phys. Rev. D, 65, 084003

Cook, G. B., & Pfeiffer, H. P. 2004, Phys. Rev. D, 70, 104016

Cook, G. B., & Whiting, B. F. 2007, Phys. Rev. D, 76, 041501(R)

Damour, T., Nagar, A., & Villain, L. 2012, Phys. Rev. D, 85, 123007

Del Pozzo, W., Li, T. G. F., Agathos, M., Van Den Broeck, C., & Vitale, S. 2013, Physical Review Letters, 111, 071101

Dietrich, T., Moldenhauer, N., Johnson-McDaniel, N. K., Bernuzzi, S., Markakis, C. M., Bruegmann, B., & Tichy, W. 2015

Dimmelmeier, H., Stergioulas, N., & Font, J. A. 2006, Mon.Not.Roy.Astron.Soc., 368, 1609

Duez, M. D., Foucart, F., Kidder, L. E., Pfeiffer, H. P., Scheel, M. A., & Teukolsky, S. A. 2008, Phys. Rev. D, 78, 104015

East, W. E., Paschalidis, V., & Pretorius, F. 2015

East, W. E., Ramazanoglu, F. M., & Pretorius, F. 2012, Phys.Rev., D86, 104053

Fan, X., & Hendry, M. 2015

Foucart, F., Duez, M. D., Kidder, L. E., Scheel, M. A., Szilágyi, B., & Teukolsky, S. A. 2012, Phys. Rev. D, 85, 044015

Foucart, F., Duez, M. D., Kidder, L. E., & Teukolsky, S. A. 2011, Phys. Rev. D, 83, 024005

Foucart, F., Kidder, L. E., Pfeiffer, H. P., & Teukolsky, S. A. 2008, Phys. Rev. D, 77, 124051

Foucart, F., et al. 2013, Phys. Rev. D, 87, 084006

Garat, A., & Price, R. H. 2000, Phys. Rev. D, 61, 124011

Gold, R., Bernuzzi, S., Thierfelder, M., Brugmann, B., & Pretorius, F. 2012, Phys.Rev., D86, 121501

Gourgoulhon, E. 2007, 3+1 Formalism and Bases of Numerical Relativity

Gourgoulhon, E., Grandclément, P., Taniguchi, K., Marck, J.-A., & Bonazzola, S. 2001, Phys. Rev. D, 63, 64029

Harry, G. M. 2010, Class.Quant.Grav., 27, 084006

Hemberger, D. A., Scheel, M. A., Kidder, L. E., Szilágyi, B., Lovelace, G., Taylor, N. W., & Teukolsky, S. A. 2013, Class. Quantum Grav., 30, 115001

Hinderer, T., Lackey, B. D., Lang, R. N., & Read, J. S. 2010, Phys. Rev. D, 81, 123016

Hulse, R. A., & Taylor, J. H. 1975a, Astrophys. J., 195, L51

—. 1975b, The Astrophysical Journal, 195, L51

Jiang, G.-S., & Shu, C.-W. 1996, Journal of Computational Physics, 126, 202

Joshi, B. C. 2013, Int. J. Mod. Phys., D22, 1341008

Kastaun, W., Galeazzi, F., Alic, D., Rezzolla, L., & Font, J. A. 2013, Phys.Rev., D88, 021501

Kidder, L. E., Scheel, M. A., Teukolsky, S. A., Carlson, E. D., & Cook, G. B. 2000, Phys. Rev. D, 62, 084032

Kuroda, K., & the LCGT Collaboration. 2010, Class. Quantum Grav., 27, 084004

Lackey, B. D., Kyutoku, K., Shibata, M., Brady, P. R., & Friedman, J. L. 2012, Phys. Rev. D, 85, 044061

Lee, W. H., Ramirez-Ruiz, E., & van de Ven, G. 2010, ApJ, 720, 953

Lichnerowicz, A. 1944, J. Math Pures et Appl., 23, 37

Lindblom, L., Scheel, M. A., Kidder, L. E., Owen, R., & Rinne, O. 2006, Class. Quantum Grav., 23, S447

Liu, X.-D., Osher, S., & Chan, T. 1994, Journal of Computational Physics, 115, 200

Lo, K.-W., & Lin, L.-M. 2011, Astrophys.J., 728, 12

Lorimer, D. R. 2008, Living Reviews in Relativity, 11, 8

Lovelace, G. 2009, Class. Quantum Grav., 26, 114002

Lovelace, G., Boyle, M., Scheel, M. A., & Szilágyi, B. 2012, Class. Quant. Grav., 29, 045003

Lovelace, G., Owen, R., Pfeiffer, H. P., & Chu, T. 2008, Phys. Rev. D, 78, 084017

Lovelace, G., Scheel, M. A., & Szilágyi, B. 2011, Phys. Rev. D, 83, 024010

Lyne, A., Burgay, M., Kramer, M., Possenti, A., Manchester, R., et al. 2004, Science, 303, 1153

M. A. Scheel, M. Boyle, T. Chu, L. E. Kidder, K. D. Matthews and H. P. Pfeiffer. 2009, Phys. Rev. D, 79, 024003

Marronetti, P., & Matzner, R. A. 2000, Phys. Rev. Lett., 85, 5500

Marronetti, P., & Shapiro, S. L. 2003, Phys.Rev., D68, 104024

Matsushima, T., & Marcus, P. S. ????, J. Comput. Phys., 120, 365

Matzner, R. A., Huq, M. F., & Shoemaker, D. 1998, Phys. Rev. D, 59, 024015

Metzger, B. D., & Berger, E. 2012, Astrophys. J., 746, 48

Muhlberger, C. D., Nouri, F. H., Duez, M. D., Foucart, F., Kidder, L. E., et al. 2014, Phys. Rev. D, 90, 104014

Murchadha, N. Ó., & York, Jr., J. W. 1974, Phys. Rev. D, 10, 428

Ossokine, S., Boyle, M., Kidder, L. E., Pfeiffer, H. P., Scheel, M. A., & Szilágyi, B. 2015

Ossokine, S., Kidder, L. E., & Pfeiffer, H. P. 2013, Phys. Rev., D88, 084031

Owen, R. 2007, PhD thesis, California Institute of Technology

Peters, P. C. 1964, Phys. Rev., 136, B1224

Peters, P. C., & Mathews, J. 1963, Phys. Rev., 131, 435

Pfeiffer, H. P., Brown, D. A., Kidder, L. E., Lindblom, L., Lovelace, G., & Scheel, M. A. 2007, Class. Quantum Grav., 24, S59

Pfeiffer, H. P., Cook, G. B., & Teukolsky, S. A. 2002, Phys. Rev. D, 66, 024047

Pfeiffer, H. P., Kidder, L. E., Scheel, M. A., & Teukolsky, S. A. 2003, Comput. Phys. Commun., 152, 253

Pfeiffer, H. P., & York, J. W. 2003, Phys. Rev. D, 67, 044022

Pfeiffer, H. P., & York Jr., J. W. 2005, Phys. Rev. Lett., 95, 091101

Postnov, K. A., & Yungelson, L. R. 2014, Living Rev.Rel., 17, 3

Pretorius, F. 2005, Phys. Rev. Lett., 95, 121101

—. 2006, Class. Quantum Grav., 23, S529

Read, J. S., Markakis, C., Shibata, M., Uryū, K., Creighton, J. D. E., & Friedman, J. L. 2009, Phys. Rev. D, 79, 124033

Rezzolla, L., Baiotti, L., Giacomazzo, B., Link, D., & Font, J. A. 2010, Class. Quant. Grav., 27, 114105

Rieth, R. 1997, in Mathematics of Gravitation. Part II. Gravitational Wave Detection, ed. A. Królak (Polish Academy of Sciences, Institute of Mathematics, Warsaw), 71–74

Scheel, M. A., Giesler, M., Hemberger, D. A., Lovelace, G., Kuper, K., Boyle, M., Szilágyi, B., & Kidder, L. E. 2015, Classical and Quantum Gravity, 32, 105009

Scheel, M. A., Pfeiffer, H. P., Lindblom, L., Kidder, L. E., Rinne, O., & Teukolsky, S. A. 2006, Phys. Rev. D, 74, 104006

Shibata, M. 1998, Phys.Rev., D58, 024012

Shibata, M., & Uryu, K. 2000, Phys. Rev. D, 61, 064001

Somiya, K., & the KAGRA Collaboration. 2012, Class. Quantum Grav., 29, 124007

Szilágyi, B. 2014, Int.J.Mod.Phys., D23, 1430014

Szilágyi, B., Lindblom, L., & Scheel, M. A. 2009, Phys. Rev. D, 80, 124010

Tacik, N., et al. 2015, Phys. Rev., D92, 124012

Taniguchi, K., Baumgarte, T. W., Faber, J. A., & Shapiro, S. L. 2006, Phys. Rev. D, 74, 041502

—. 2007, Phys. Rev. D, 75, 084005

Teukolsky, S. A. 1998, Astrophys.J., 504, 442

The Virgo Collaboration. 2010, Advanced Virgo Baseline Design, vIRâĂŞ027AâĂŞ09

Tichy, W. 2011, Phys.Rev., D84, 024041

—. 2012, Phys.Rev., D86, 064024

Tsatsin, P., & Marronetti, P. 2013

Tsokaros, A., Uryū, K., & Rezzolla, L. 2015, Phys. Rev., D91, 104030

Verkley, W. T. M. 1997, Journal of Computational Physics, 136, 100

Walsh, D. M. 2007, Class. Quantum Grav., 24, 1911

Worley, A., Krastev, P. G., & Li, B.-A. 2008

York, J. W. 1999, Phys. Rev. Lett., 82, 1350

York, Jr., J. W. 1979, in Sources of Gravitational Radiation, ed. L. L. Smarr (Cambridge, England: Cambridge University Press), 83–126